μ-Plasma assisted deposition of titanium dioxide thin films

Verheyen, Joerie

Award date:
2017

Eindhoven University of Technology,

Department of Applied Physics,

Plasma & Materials Processing group

µ-Plasma assisted deposition of Titanium Dioxide thin films

Joerie Verheyen

January 2017 PMP 17-01

Supervisors

Dr. M. Creatore (TU/e), graduation professor

MSc. M. Aghaee (TU/e), daily supervisor

Dr. Ir. A. Stevens (Innophysics), advisor

Abstract

In this Master Thesis work, the potential of the µ-PlasmaPrinter (µPP) as plasma source for deposition of patterned thin film metal oxides is investigated. The µPP combines the benefits of digital printing technique with the versatility of atmospheric pressure plasma processing via multi needle-to-plane dielectric barrier discharges (DBDs). The system has been already used to deliver amino-group containing polymer thin films. However the µPP has never been used for deposition of thin film (sub-) millimeter patterned metal oxides, which can be used for the fabrication of organic electronics, sensors and LEDs.

Titanium dioxide (TiO_2) was chosen as demonstrator with titanium tetra-isopropoxide (TTIP) as titanium precursor. Several hardware modifications were required since TTIP is reactive with moisture (i.e. water) from the environment and has a relatively low melting point. In the first part of this work, sublimated TTIP precursor were guided to the discharge volume (where O_2 was present) by means of nitrogen carrier gas, in order to deposit patterned TiO_2 thin films. This operation mode is also known as plasma-enhanced chemical vapor deposition (PE-CVD). The depositions were performed on glass and silicon (Si) substrates. The TiO_2 films contained high levels of carbon and nitrogen as impurities, according to XPS measurements and resulted of porous nature.

Therefore, in the second part of this Master Thesis work, the possibility of achieving higher material quality by spatially separating the exposure of the substrate to the TTIP precursor and to the O_2 plasma was investigated. The deposition method where both precursor and oxidant exposures are separated in the temporal (or spatial) domain is known as atomic layer deposition (ALD). Hence the µPP system was upgraded to a µ-Plasma assisted ALD setup through the integration of a precursor dosing module. The plasma and precursor head served each as one half-cycle in the ALD-process. ALD was achieved through the alternate translation of both deposition heads over the substrate. It was shown that self-limiting surface reactions were obtained with a precursor exposure time of 475 ms, 10s of purge time and 400 µs of O_2 plasma exposure per ALD cycle, leading to a saturation value of the growth per cycle (GPC) of 0.145 nm/cycle. It was shown that the amount of carbon in the films decreased to less than one percent by increasing the plasma exposure time per ALD-cycle.

Hence the µPP can be used to deposit almost carbon-free TiO_2 thin films with sub-nanometer growth control by the modification to a plasma-assisted ALD setup. Furthermore it was shown that the modification leads to an enhancement of the patterning resolution and provides a more accurate thickness control for small area features. The possibility to perform patterned plasma-assisted ALD at atmospheric pressure is something unique and could be applicable in numerous applications or the µPP-head could possibly be implemented in other (spatial) ALD systems.

Content

1. Introduction

The interest in area selective deposition of thin films has been growing extensively in the past years, for example in the manufacturing of transistors, interconnect technology [1], oxide electronics [2], printed micro-electronics [3] and labs-on-chips devices [4]. The feature dimensions keep shrinking according to Moore's law in the state-of-the-art devices [5], i.e. recently Intel fabricated a transistor as small as 14 nm [6]. Nonetheless, area selective thin film deposition is also a challenge in large-area electronics, where (sub-)millimeter patterned thin films are required, for example in the fabrication of transparent conductive oxides (TCOs), e.g. indium tin oxide (ITO), organic light emitting diodes (OLEDs), liquid crystal displays (LCDs), etc. [7,8,9]. One of the most popular approaches at the moment for nano-patterning of thin films for nano-electronic applications is offered by a combination of atomic layer deposition (ALD[a]) with lithography and/or etching steps, since ALD itself delivers no control over the lateral dimensions [1,5]. However (photo-)lithography is costly and delivers a low throughput, due to the large amount of processing steps (resist spinning, light exposure, resist development)[1]. Therefore photolithography is not beneficial in applications for large-area electronics, however it is the state-of-the-art method in the fabrication of nano-patterned thin films. Due to the world's cheaper and faster mindset, a continuous demand exists for alternative methods in order to decrease the process time and corresponding cost.

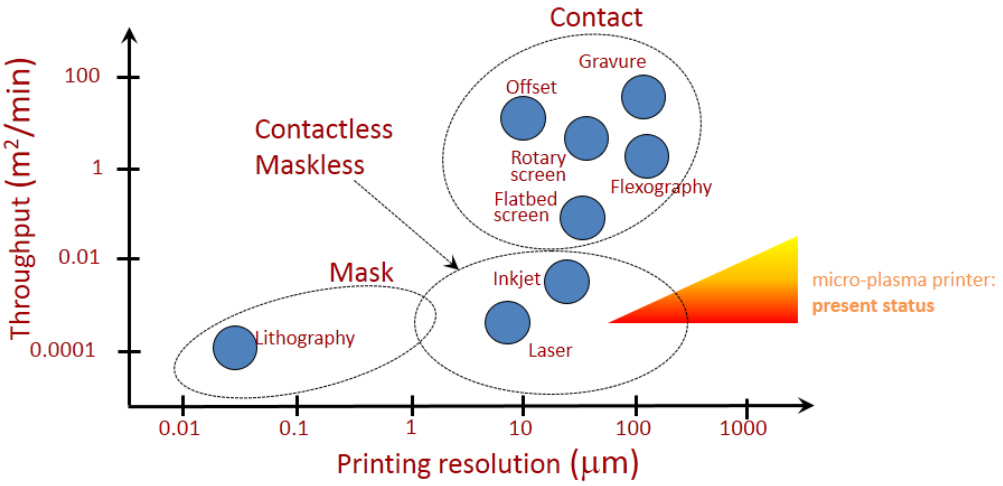

Figure 1: Throughput (m²/min) as a function of patterning resolution (µm) for several contact(less) and mask(less) deposition techniques. The present status of the µ-PlasmaPrinter is shown. Patterned thin films can be fabricated with the µPP in a contactless and maskless manner at atmospheric pressure.

Figure 1 presents an overview of mask(less) and contact(less) deposition techniques which can be used to fabricate patterned thin films. The throughput (m²/min) is given as a function of the required patterning resolution (µm). Deposition techniques using a mask, e.g. photolithography, achieve the highest resolution (<100 nm), however the throughput is low. The contact-deposition techniques achieve the highest throughput, despite the lower resolution. Therefore considerable effort has been dedicated in the last years in investigating other methods to fabricate (sub-)millimeter patterned thin films in a maskless and contactless process. One of the most promising techniques would be direct-printing, which is a fast and inexpensive deposition technique to deposit micro-scale patterned thin

[a] Basic principles and properties of ALD can be found in Appendix A.

films. A wide variety of different direct-printing techniques are on the market, for example inkjet printing, direct-write assembly, micro-stereo lithography, etc. The minimum feature sizes vary in a range from a few hundred micrometers down to a few micrometer[10]. Innophysics B.V. has developed the µ-PlasmaPrinter (µPP), which enables plasma treating of surfaces at atmospheric pressure in a patterned manner without the requirement for contact or masks. The present status of the µPP is depicted in Figure 1. The patterned, maskless and contactless characteristics of the µPP make it a potentially attractive deposition technique. However the potential of the µPP has not been explored yet and has never been used as a tool for deposition of patterned inorganic metal oxides thin films.

µ-PlasmaPrinting

The µPP was developed and engineered by Innophysics B.V. and combines the benefits of digital printing technique with the versatility of atmospheric pressure plasma processing, by adopting multi needle-to-plane dielectric barrier discharges (DBDs). The main parts of the system are a high voltage substrate table, a dielectric layer and a print head. The print head is integrated in a XYZ platform and consists of 24 grounded needle electrodes, which can be individually displaced towards the high voltage substrate table. Thereby the critical electric field required for breakdown of the gas can be passed and micro discharges are ignited, as depicted in Figure 2a. Figure 2b shows the side and bottom view of the print head when all needles are simultaneously ignited. The µPP enables plasma treating surfaces in a patterned manner by defining digital images as patterns. Since the system is operated at atmospheric pressure, there is no need for expensive vacuum equipment and it enables the compatibility with roll-to-roll systems for large area processing in industrial applications.

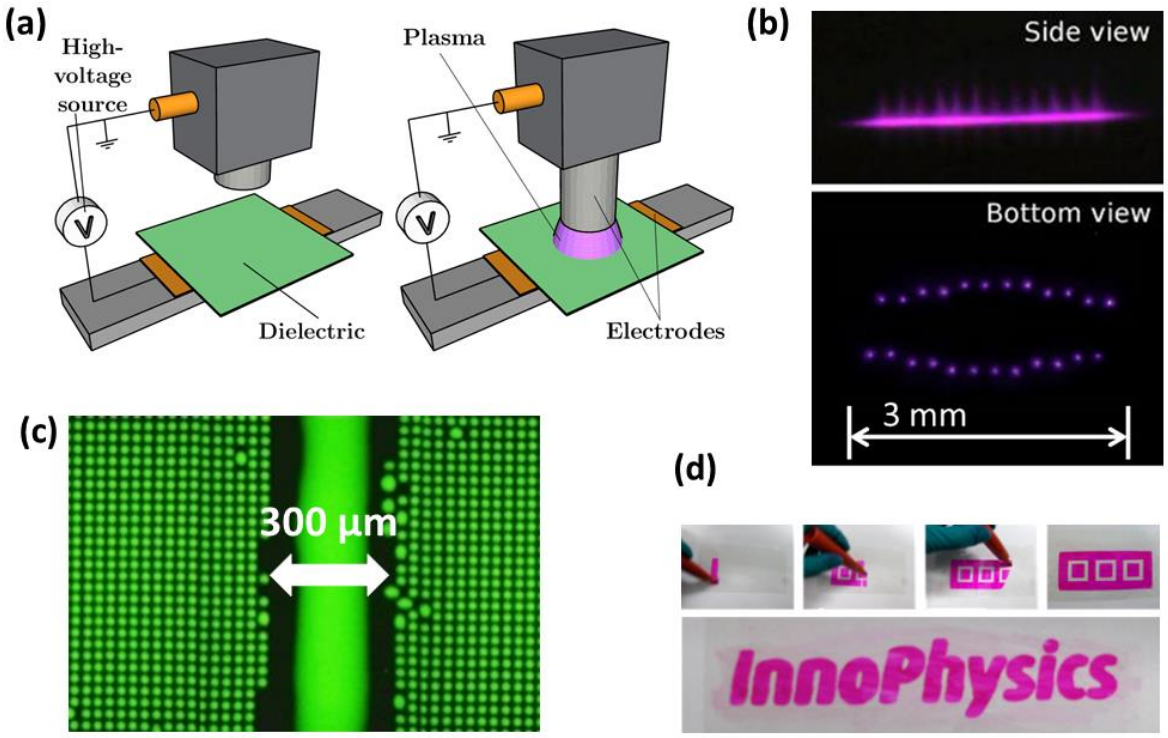

Figure 2: a) Micro discharges are ignited when a needle electrode is displaced towards the high voltage substrate table and the applied electric field reaches the critical field required for breakdown [11]. B) Side and bottom view of the print head when all needles are simultaneously ignited. C) Resolution of the µPP for activation of surfaces using N_2 plasma, prior to digital inkjet printing. D) Hydrophilic functional groups are implanted at the surface, through µ-PlasmaPrinting, at which ink only adheres.

The system has been initially designed for patterned surface treatment using air, N_2 or O_2 plasmas. The achievable resolution with the µPP for surface treatment is proved to be in the order of several hundreds of µm, as depicted in Figure 2c, in which an image is shown where the µPP has been used prior to inkjet printing in order to increase the wetting behavior. The µPP has been used to deposit patterned organic thin films, i.e. amine-containing polymer by guiding a specific vaporized precursor (3-aminopropyl trimethoxysilane, APTMS) towards the discharge-volume, without the requirement for a mask or physical contact of the needle electrodes with the substrate. A possible application of the amine-containing polymer films is electroless Nickel plating [12]. Figure 2d presents an example where hydrophilic functional groups are implanted at the surface by a plasma polymerization process. The µPP was used as a plasma source and hexamethyldisiloxane (HMDSO) as precursor, ink only adheres at the treated areas [13].

The possibility to deposit metal oxides thin films with the µPP system has not been explored yet. However, the µPP has a potential to be utilized as plasma source for plasma enhanced chemical vapor deposition (PE-CVD) of metal oxides in atmospheric pressure. PE-CVD is a deposition technique in which a vaporized precursor, together with an oxidant (i.e. O_2) is fed into the discharge volume[14]. As we will see at the end of section 4.1, the material quality of the deposited thin films with the µPP as plasma source in a PE-CVD process is not satisfactory in terms of film density and presence of impurities. Therefore, the setup is converted into a micro-plasma printer assisted atomic layer deposition (ALD) setup. In ALD (the basic principles and properties of ALD can be found in Appendix A) the substrate is exposed to alternating pulses of precursor and oxidant (an O_2 µ-plasma in this case) exposures, resulting in self-limiting surface reactions[15,16]. The self-limiting and alternating behavior is acknowledged to result in high-quality films. Therefore, the combination of the µ-PlasmaPrinting technique with ALD could lead to a significantly enhanced material quality patterned thin films.

Goal and outline

The µ-PlasmaPrinter was initially designed to activate surfaces chemically with air, nitrogen or oxygen plasmas. However the µPP has not been employed for metal oxide film deposition so far. Therefore the first research question is:

1. *Can the µPP, which is initially used for plasma activation of surfaces, be used for deposition of metal oxides thin films (e.g. Titanium dioxide) in a patterned manner according to a PE-CVD mode?*
    a. What are the required hardware modifications to enable metal oxides thin film deposition with the µPP?
    b. What is the growth rate of the deposited film? Is there a difference when depositing on dielectric or conductive substrates?
    c. What are the film properties? What is the stoichiometry, impurity content, etc.? And how do the properties (stoichiometry, roughness, etc.) compare with those achieved with other CVD systems?
    d. What is the patterning resolution of the µPP, when depositing TiO_2 thin films in PE-CVD mode?

Secondly, the question arises if the separation of the organometallic precursor and oxidant can lead to an improvement in film properties? Therefore the second research question is:

2. *Can the µPP be modified in order to achieve successful plasma-assisted atomic layer deposition of metal oxides (e.g. TiO_2) in a patterned manner?*
    a. What are the required hardware modifications?
    b. What is the ALD process development?
    c. What are the properties of the films? What is the effect of the plasma exposure time?
    d. What is the patterning resolution of the µPP in ALD mode? How does the resolution change in comparison with the PE-CVD mode?
    e. How do the properties (stoichiometry, impurity content, roughness, etc.) change in comparison with the PE-CVD mode? And how do these properties compare with other ALD processes reported in literature?

The structure of the thesis is based on the above mentioned specific research questions/goals. The principles of dielectric barrier discharges, streamer formation and the µPP are reviewed in Chapter 2. In Chapter 3, the experimental setup and diagnostic techniques are discussed. The hardware related part of the µPP is discussed, followed by the deposition setup for the PE-CVD experiments. The required hardware modifications to modify the system into a plasma-assisted ALD setup are described in the next section, together with the deposition setup. Different techniques such as Spectroscopic ellipsometry, X-ray Photoelectron spectroscopy, Atomic force microscopy, Rutherford backscattering spectrometry, Scanning electron microscopy and Raman spectroscopy were used to characterize the deposited thin films in terms of thickness, physical and chemical properties. The results are presented in Chapter 4. First the deposited TiO_2 thin films in PE-CVD mode are discussed. Followed by the results of the ALD-experiments together with a comparison of the two different deposition modes. The conclusion and answers to the research questions are given in Chapter 5, together with an outlook for future experiments.

2. Theoretical background

The µPP is based on multi needle-to-plane dielectric barrier discharges (DBDs). Electrical breakdown in a DBD occurs in a large amount of filaments, referred to as micro-discharges [17,18]. In the first section the principles of DBDs and the formation of a micro-discharge are explained. Secondly, the principles of the µPP are discussed. The hardware related part of the µPP is described in section 3.1.

2.1 Dielectric Barrier Discharges (DBDs)

Plasmas can be divided in two main categories, thermal and non-thermal plasmas. In thermal plasmas the electron and ion (gas) temperatures are equal, while in non-thermal plasmas the electron temperature is significantly higher than the ion (gas) temperature [19]. Atmospheric pressure non-thermal plasmas are generated by either corona discharge or DBDs [20]. The DBDs have been studied for more than a century [21,17], due to the broad variety of applications such as surface modification, material processing, water treatment and ozone production [22,23]. A basic planar DBD configuration is shown in Figure 3, where discharges are ignited between two metallic electrodes connected to an AC power supply and at least one of the two electrodes is covered by a dielectric layer. The latter is done to limit the discharge current and dissipated power and to prevent the transition to an arc discharge [24]. Materials such as glass, quartz, polymers and ceramics can be used as dielectric layers. The dielectric layer in between the electrodes does not allow the transport of dc current [22], hence an alternating electric field is required to drive a displacement current [18]. Therefore DBDs are always operated with AC supply voltages.

The voltage applied between the electrodes needs to exceed a certain threshold voltage in order to cause breakdown of the gas, i.e. to ignite a gas-discharge. The breakdown voltage of a gas is determined by the Paschen's law, which is explained in this section. Electrical breakdown in a DBD configuration occurs in a large series of current filaments with a short duration time ($<10^{-7}$s), referred to as micro-discharges [17,18]. DBDs can be ignited at atmospheric pressure and numerous micro-discharges are observed in most gases [25]. The discharges can be influenced by external parameters, for example by the amplitude and frequency of the supply voltage, the distance between the two electrodes and type of gas mixture.

Different types of discharges are presented in Figure 4, in which the voltage is plotted as a function of the discharge current. The graph is determined for a parallel plate setup with Neon gas at 1 Torr pressure and a gap distance of 50 cm. Therefore the numeric values are not relevant for the µPP, but the behavior is expected to be the same. The dark discharges (Figure 4 A-D) are also known as Townsend discharges. With low applied voltage (A, B), the discharge is not self-sustaining and current is provided by the outside circuit. Once the applied voltage exceeds the breakdown voltage, the self-sustained discharge region is reached (C, D) and a Townsend discharge is sustained.

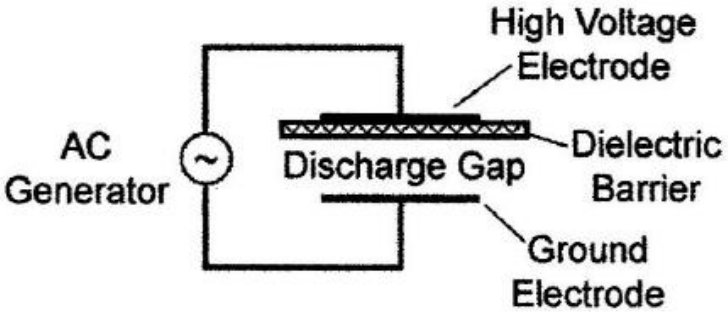

Figure 3: Basic DBD configuration. A dielectric layer is positioned between two parallel plate electrodes, in order to limit the discharge current and dissipated power. One electrode is fed with a high voltage signal, while the other electrode is grounded. [25]

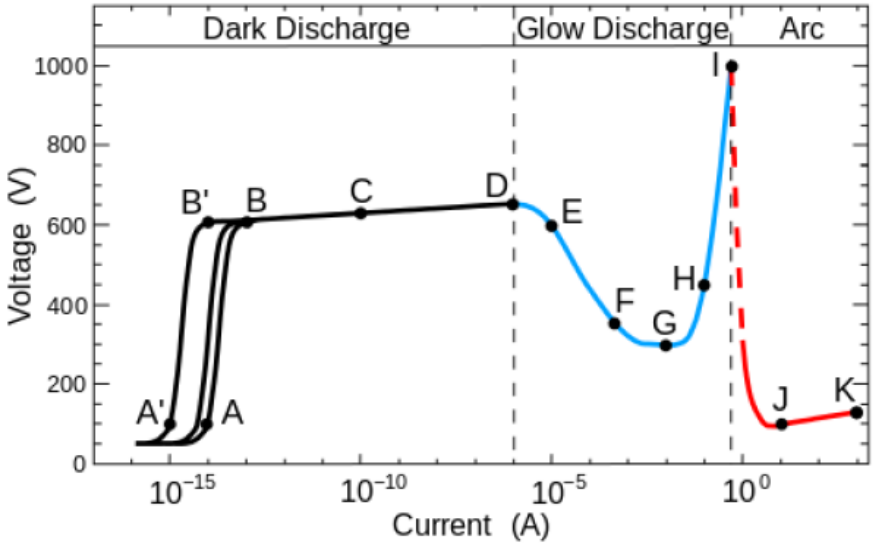

Figure 4: Schematic representation of the discharge characterization. The voltage is shown as a function of discharge current. The graph is determined for a parallel plate setup with a gap distance of 50 cm for Neon gas at 1 Torr pressure.

The dark discharge (Townsend discharge) region is characterized by a low discharge current density, resulting in a low ionization rate and a low charge density [26]. Therefore no appreciable light is emitted, therefore the name dark discharge. When the discharge current further increases, the discharge makes a transition to a glow discharge (D-I), where the required voltage to sustain the discharge decreases. The glow discharge region is divided in two separate regions, referred to as the normal (E-G) and the abnormal (G-I) glow discharge. When the discharge current exceeds a specific threshold current, the discharge changes from an abnormal glow discharge to an arc discharge (I-K) and the required voltage to sustain the discharge decreases significantly. Region I-J represents non-thermal plasmas, while region J-K represents thermal plasmas, which are characterized by a large discharge current.

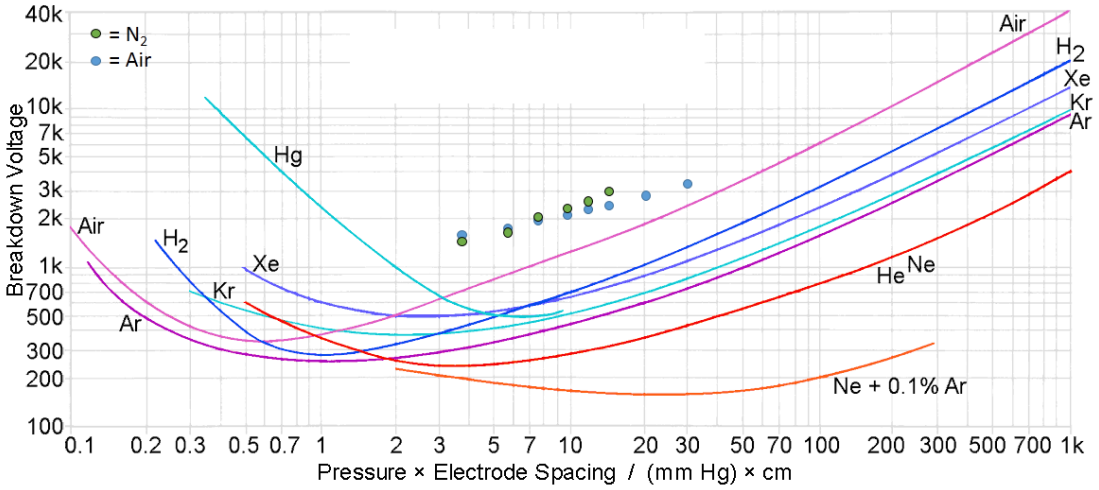

Figure 5: Paschen's curves for different gases: the breakdown voltage is depicted as a function of pressure times gap distance (Torr cm). The blue and green dots represent the breakdown voltage determined for the µPP for both air and nitrogen (100 sccm), respectively. Since the µPP operates at atmospheric pressure, the breakdown voltage depends only on the gap distance.

The electrical breakdown voltage of a gas is determined by the Paschen's law, which describes the breakdown voltage as a function of the product of electrode gap spacing and chamber pressure, according to Eq. 1:

$$V_{br} = \frac{\alpha p d}{\ln(pd) + \beta} \tag{1}$$

with V_{br} the breakdown voltage, d the gap electrode distance (meters), p the pressure (Torr), and α and β constants depending on the gas mixture. The Paschen curves in Figure 5 are determined for a parallel plate setup with DC supply voltages, low pressure and no dielectric layer between the electrodes. The blue and green dots represent the experimentally determined breakdown voltages for the µPP for air and nitrogen (100 sccm) respectively (measured during this Master Thesis work). As seen in the figure, the experimental determined breakdown voltages for the µPP are higher than predicted by Paschen's law. Moreover, the values are also higher than other in the literature reported values[27]. A few possible explanations are listed below:

- Parallel plate vs. needle-to-plane setup.
- DBD setup (needle electrode serves as the cathode in only half of the voltage cycles, hence decreased amount of secondary electron emission[28]).
- Voltage drop across the dielectric layer.
- Paschen curves are determined for a low pressure setup with larger gap distance. µPP operates at atmospheric pressure with very small gap distances (in order of 100 µm).

However, the voltage drop across the dielectric layer is the most likely explanation. The measured voltage is the voltage applied between the two electrodes, however there is a finite voltage drop across the dielectric layer. Therefore the potential difference in the discharge gap is smaller than the applied voltage, which explains the difference between the Paschen's curves and the experimentally determined values. Since the µPP is operated at atmospheric pressure, the breakdown voltage depends only on the gap distance between the electrodes (Eq. 1). The breakdown voltage of nitrogen

is smaller than the breakdown voltage of air at small gap distance, however the opposite occurs by increasing the gap distance, as shown in Figure 5.

Development of a micro-discharge

The development of a micro-discharge is explained using Figure 6, in which the different stages of a micro-discharge are presented. A micro-discharge is initiated by an electron avalanche and at least one free electron is required to trigger an electron avalanche. The free electron is subjected to an applied electric field according to Eq. 2:

$$E = \frac{V_{applied}}{d_{gap}} \tag{2}$$

with $V_{applied}$ the applied voltage and d_{gap} the gap distance between the electrodes. The free electron is accelerated by the electric field and thereby increasing its energy. When the electron gains enough energy to cause ionizing collisions with neutrals, an ion and an extra electron are produced. The free electrons are consequently accelerated by the electric field and are able to ionize other neutrals. The latter is known as direct-ionization[28]. The electron density increases exponentially according to Eq. 3:

$$n_e = n_{e,0}\, e^{\alpha * z} \tag{3}$$

in which n_e is the electron density, $n_{e,0}$ the initial electron density, z the distance over which the electrons are accelerated and α the Townsend ionization coefficient [29]. The exponential increase of free electrons induces an electron avalanche (Figure 6). Due to the large mass difference between electrons and ions, the electrons are accelerated faster than the ions and are located in the head of the avalanche. The charge separation induces a dipole, enhancing the local electric field strength in the streamer head [12,30]. An avalanche to streamer transition appears, when the electric field in the streamer head is comparable in magnitude as the externally applied electric field [29]. The streamer propagates to the anode, with the streamer head in front and the electrons disappear into the electrode, upon impact of the streamer head. The positive ions are left behind in the discharge gap, resulting in a strong radial electric field (Figure 6) [17,31]. The recombination of electron-ion pairs leads to the emission of photons, which are able to cause secondary avalanches through photo-ionization. The secondary avalanches result in the formation of a cathode directed streamer, which are characterized by a velocity of approximately 10^8 cm/s [30]. The impedance in the discharge gap drops upon formation of a streamer, resulting in a large discharge current and dissipation of power. A dielectric layer is positioned between the electrodes, in order to reduce the dissipated power and to prevent the substrate from damage. The discharge breaks down after tens of nanoseconds, because the electric field in the discharge gap is counteracted by charge accumulation at the dielectric surface [29]. The remaining positive ions diffuse slowly to the electrode, resulting in a slow decaying ion current, which can last for tens of microseconds. The latter is known as micro-discharge remnant [12,29]. A DBD cannot be operated with DC supply voltages, since charge accumulation at the dielectric surface prevents the formation of new streamers, therefore a DBD is always operated with AC supply voltages. The approximated duration time and transferred charges for every stage of a streamer discharge are presented in Table 1.

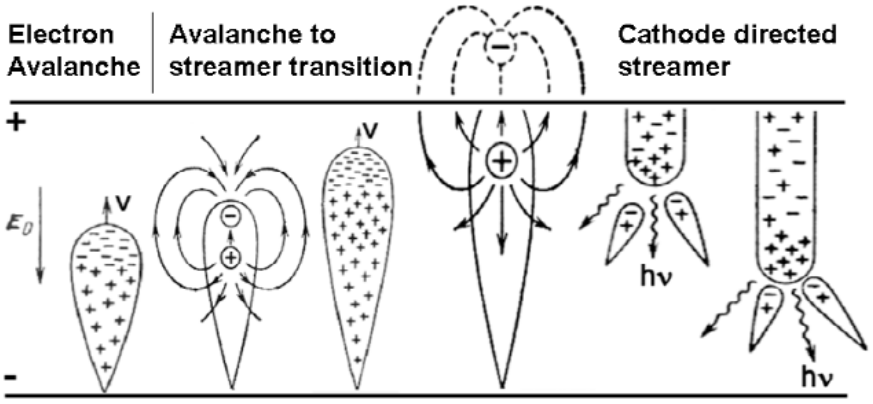

Figure 6: Development of a streamer discharge. A streamer discharge is initiated by an electron avalanche, followed by an avalanche to streamer transition and finally by a cathode directed streamer. Taken from [30].

Table 1: Duration time and transferred charges for the different stages of a micro-discharge.

	Duration time	**Transferred charge**
A: Micro-discharge	40 ns	10^{-9} C
A.1 Electron avalanche	10 ns	10^{-11} C
A.2 Cathode directed streamer	1 ns	10^{-10} C
A.3 Plasma channel	30 ns	10^{-9} C
B: Micro-discharge remnant	1 ms	$< 10^{-9}$ C

2.2 µ-PlasmaPrinting principles

The µPP enables plasma treating surfaces in a patterned manner by defining digital images as patterns. The main parts of the µPP are a high voltage substrate table, a dielectric layer and a print head. The power supply generates a sinusoidal voltage signal with a frequency of 67 KHz and an amplitude variable between 0 and 10 kV_{PP} (peak-to-peak). The high voltage signal is fed into the substrate table. Since the µPP is based on DBDs, a dielectric layer is placed between the substrate table and the print head.

The print head consists of two rows of twelve grounded needle electrodes, equally spaced by 270 µm and each needle can be individually displaced towards the substrate table, which will be addressed through the rest of this thesis as an "*activated needle*". An activated needle is displaced by approximately 700 µm towards the high voltage substrate table (Figure 7a), thereby increasing the applied electric field, according to Eq. 2. The activated needle electrodes oscillate with a frequency between 0 and 400 Hz, depending on the printing settings. The distance between the substrate and the needle electrode (at its minimum position) is variable between 50 and 300 µm, depending on the gas mixture and applied voltage. As already has been discussed in section 2.1, the electrical breakdown voltage of a gas is determined by Paschen's law and depends on the gap distance between the needle electrodes and the high voltage substrate table. According to the Paschen's law, a micro-discharge is ignited when a needle electrode is displaced towards the substrate table and reaches the critical distance for the breakdown. The discharge is terminated when the gap distance becomes larger than the critical distance (Figure 7a) and Paschen's law is not satisfied anymore. The print head is integrated in a XYZ platform, enabling patterned plasma treatment of the surface positioned on top of the high voltage table. The µPP can be used for different types of plasma processing (i.e. surface modification, etching and deposition) by guiding a specific gas mixture to the print head.

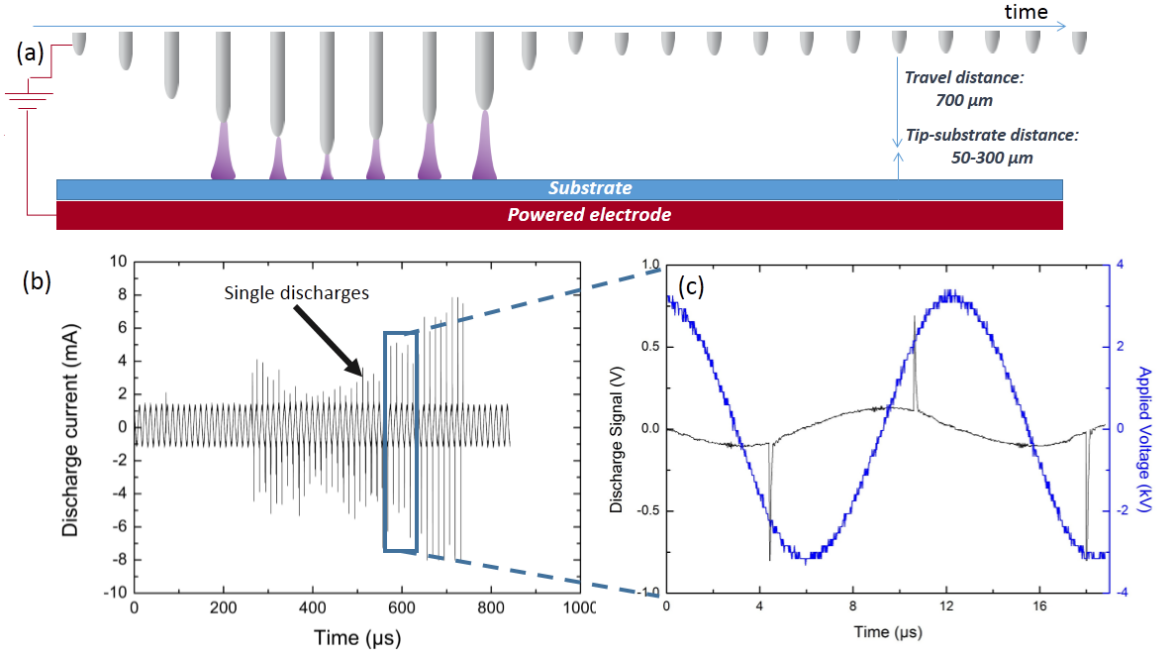

Figure 7: Basic principles of µPP setup. Micro-discharges are ignited when a needle electrode is activated and the applied electric field reaches the critical field required for breakdown. An activated needle is displaced by approximately 700 µm, towards the high voltage substrate table. (b) Discharge current as a function of time. Multiple discharges are ignited during one needle oscillation period. (c) Discharge signal and applied voltage as a function of time, at least two discharges are ignited during one voltage period. One positive on the rising edge and one negative on the falling edge of the voltage signal.

In order to print one plasma dot, a needle electrode is activated and starts moving towards the high voltage substrate table, thereby decreasing the gap distance between the needle electrode and the substrate table. When the gap distance reaches the critical distance required for breakdown of the gas, a first micro-discharge is ignited (Figure 7a,b). Since the frequency of the supply voltage (67 KHz) is significantly larger than the needle frequency (0-400 Hz), multiple discharges are ignited during one needle movement (Figure 7b). In approximately 400 µs of one needle movement, the needle electrode is close enough to the substrate to satisfy Paschen's law. The applied voltage is a sinusoidal signal and at least two discharges are ignited during one voltage period, one positive discharge on the rising edge and one negative on the falling edge, as shown Figure 7c[32]. The number of ignited micro-discharges in one needle movement depends on the gap distance, applied voltage, gas composition and type of substrate. Typically in one needle movement 40-100 micro-discharges are ignited (Figure 7b). The discharge current, plasma energy and plasma duration time have been studied in previous works, by the author of this Master Thesis [32]. The plasma energy and duration time are presented as a function of applied voltage for variable gap distance in Figure 8, determined in ambient air and for one single needle movement. Extended information can be found in [32]. It was shown that with a plasma filament size of 100 µm (radius), the typical power per cm² varies between 250 and 650 W/cm², depending on the applied voltage and gap distance. However the power density is highly dependent on the filament size.

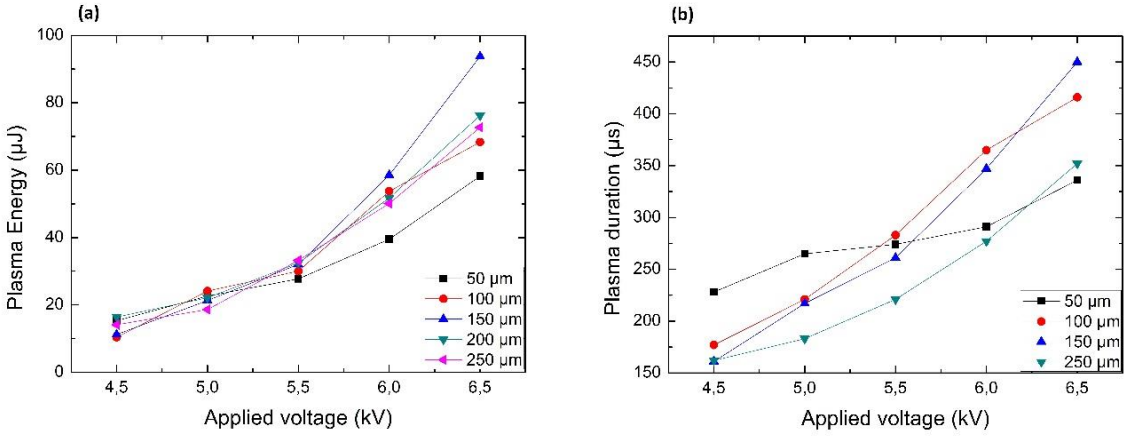

Figure 8: Plasma energy (a) and duration time (b) as a function of applied voltage for variable gap distance. Determined in ambient air and for one single needle movement. [32]

As the µPP is a DBD system, a dielectric layer is required between the needle electrodes and the high voltage substrate table. Two different configurations of the setup exist, depending on the type of substrate (i.e. dielectric or conductive). If the substrate is a dielectric material, no extra dielectric is required between the needle electrodes and high voltage table. The substrate itself serves as the dielectric in the DBD system (Figure 9a). When a voltage is applied between the high voltage substrate table and grounded needle electrodes, an electric field is established and the charge carriers in the dielectric substrate are shifted slightly from their average positions, counteracting the applied electric field. When the Paschen's law is satisfied, micro-discharges are ignited between the activated needles and dielectric substrate.

The second configuration of the setup (Figure 9b) is used when the substrate is (semi-)conductive (e.g. Si). In order to maintain a DBD system, a dielectric layer is required between the needle electrodes and the conductive substrate. A 260 µm thick Al_2O_3 layer is used as the dielectric and positioned between the needle electrodes and the conductive substrate, as depicted in Figure 9b. The distance between

the activated needles and the dielectric layer is approximately 150 µm. When a voltage is applied between the high voltage table and the grounded needle electrodes, two electric fields establish with the same direction and the charge carriers in the dielectric layer shift slightly from their average positions, trying to cancel the applied electric field. When Paschen's law is satisfied, micro-discharges are ignited both between the activated needles and dielectric layer and between the dielectric layer and conductive substrate, as depicted in Figure 9b.

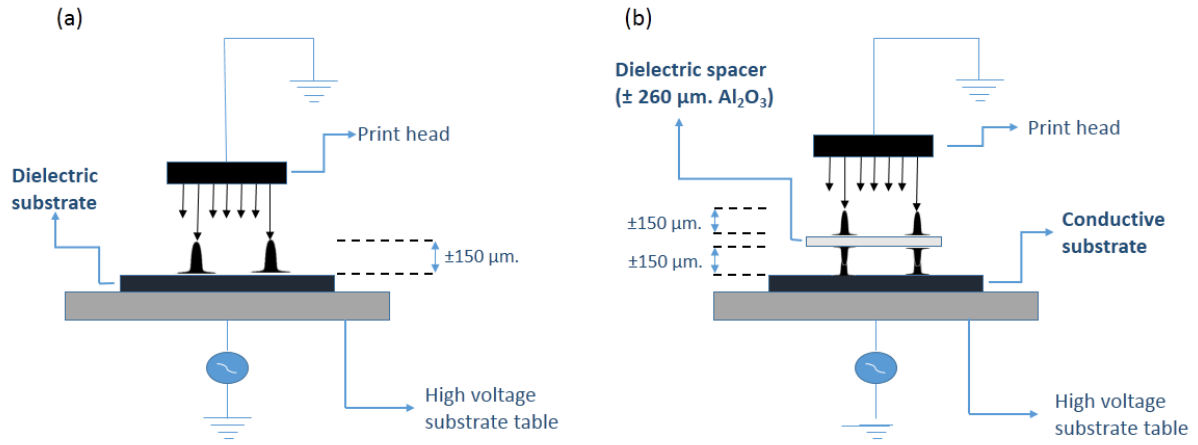

Figure 9: Schematic representation of the two different configurations of the setup, depending on the type of substrate (i.e. dielectric or conductive). When the substrate is a dielectric material (a), the substrate itself serves as the dielectric in the DBD system. Micro-discharges are ignited between the activated needles and the dielectric substrate. When the substrate is conductive (b), a dielectric layer (260 µm thick Al_2O_3) is positioned between the conductive substrate and the needle electrodes in order to maintain a DBD system. Micro-discharges are ignited both between the activated needles and dielectric layer and between the dielectric layer and conductive substrate.

Patterned plasma treatment is enabled by loading digital images into the µPP-software. The software consequently transforms the image into a pattern and defines which needle electrodes need to be activated at the specific locations. The images consist of black and white pixels. Black pixels are ignited by one of the 24 needle electrodes, while white pixels remain untreated. The distance between consecutive plasma dots of a defined pattern can be modified in the µPP-software. Two values of 90 or 270 µm were chosen as distance between consecutive plasma dots. The difference between the two printing modes is depicted in Figure 10. The numbers inside the dots, represents which needle electrode (1-24) is activated for the specific plasma dot.

As it was already mentioned, the distance between the centers of the needle electrodes in the plasma head is 270 µm. Thus when an image of twelve pixels wide is printed, with the distance between the dots set at 270 µm, the printer needs only one movement in Y axis to complete the image (Figure 10a). Plasma printing with a distance of 270 µm between consecutive dots is referred to as *printing without overlap,* since the different plasma filaments do not overlap each other on the surface (under assumption that the plasma filament size is less than 270 µm). The other possibility is to set the distance between the dots at 90 µm (Figure 10b). Plasma printing when the distance between the dots is set at 90 µm is referred to as *printing with overlap*, since the different plasma filaments do overlap each other on the surface. One plasma print repeat (PR) is completed when every defined dot in the pattern is ignited once, by one of the 24 needle electrodes. The plasma ignition time for every dot (150 µm gap and 6.0 kV_{PP}) is approximately 400 µs (Figure 8b).

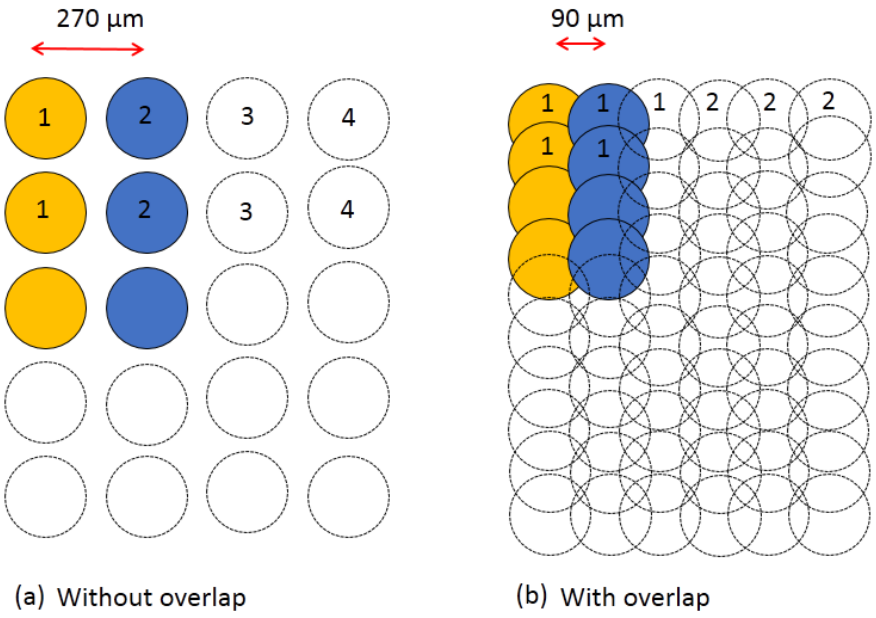

Figure 10: Motion patterns of the µPP for two different distances between consecutive plasma dots: (a) 270 µm and (b) 90 µm. In (a) the different plasma filaments do not overlap each other on the surface, while in (b) the plasma filaments do overlap. Under assumption that the plasma filament size less than 270 µm. µ-PlasmaPrinting with the distance between consecutive dots set at 270 or 90 µm, is referred to as printing without and with overlap, respectively. The numbers inside the dots, represent the needle electrode activated for the specific dot.

3. Experimental

In this chapter, the experimental setups and (thin film) characterization methods are explained. In the first section, the working principle of µPP setup is explained in detail. The deposition setups for the PE-CVD and plasma-assisted ALD experiments are described in the second section. Several material characterization methods were used such as spectroscopic ellipsometry (SE), X-ray photoelectron spectroscopy (XPS), atomic force microscopy (AFM), scanning electron microscopy (SEM), Raman spectroscopy and Rutherford backscattering spectrometry (RBS) which are addressed in the last section of this chapter.

3.1 µ-PlasmaPrinter

The µPlasmaPrinting principles were already explained in section 2.2. This section addresses the hardware related part of the µPP setup. Figure 11 shows the different components of the µPP. The power supply generates a sinusoidal voltage signal which is fed into the substrate table, which is made of glass or plastic with a thin ITO (Indium tin oxide) layer on top. The ignited micro-discharges can be visualized by an inline camera. The system is operated by the µPP-software, as developed and engineered by Innophysics B.V. Since the µPP is operated at atmospheric pressure it does not require expensive vacuum equipment and it enables plasma treating surfaces which cannot be used in vacuum. Nonetheless the µPP is compatible with roll-to-roll systems for large area processing in industrial applications.[b]

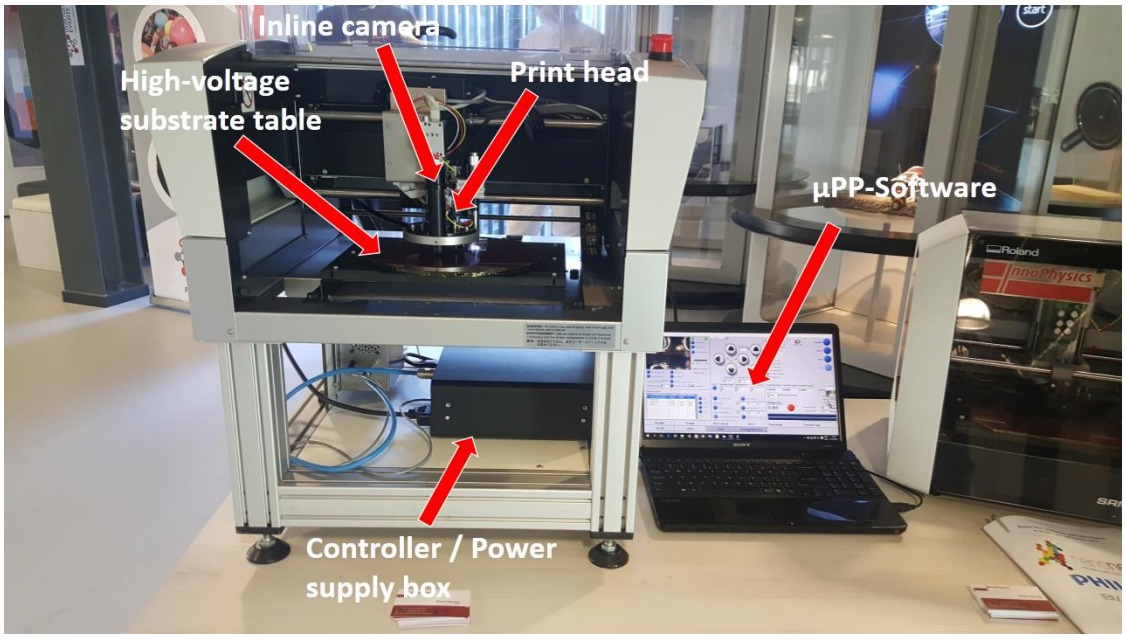

Figure 11: Picture of the µ-PlasmaPrinter, showing the different components. The main parts are a print head, substrate table, controller/power supply box and the µPP-software.

[b] The interested reader is referred to the following website: http://innophysics.nl/index.php/uplasmaprint-movie where an informative video of the µPP can be found.

Figure 12 presents a 3D-schematic of the plasma print-stage, which is integrated at a XYZ-platform. The print-stage is composed of a print head, gas chamber, gas curtain system and an inline camera. A gas chamber with an inlet and outlet is attached around the print head, as indicated in Figure 12, which is designed to guide and evenly distribute the gas mixture towards the needle electrodes. The gas outlet can be connected to a vacuum pump and be used as an exhaust line. In order to avoid reactions between the gas mixture and surrounding air from the environment, a gas curtain system was designed which surrounds the print head and gas chamber and provides a continuous flow of nitrogen. The plasma print-stage is integrated at a XYZ-platform, more specifically in a modified Roland EGX-350 engraving machine, in order to make patterned plasma treatment possible. The motion speed of the system is variable between 10 and 60 mm/s and the motion engines have an accuracy of ± 20 µm in XY-direction, which control the spatial position of the print head.

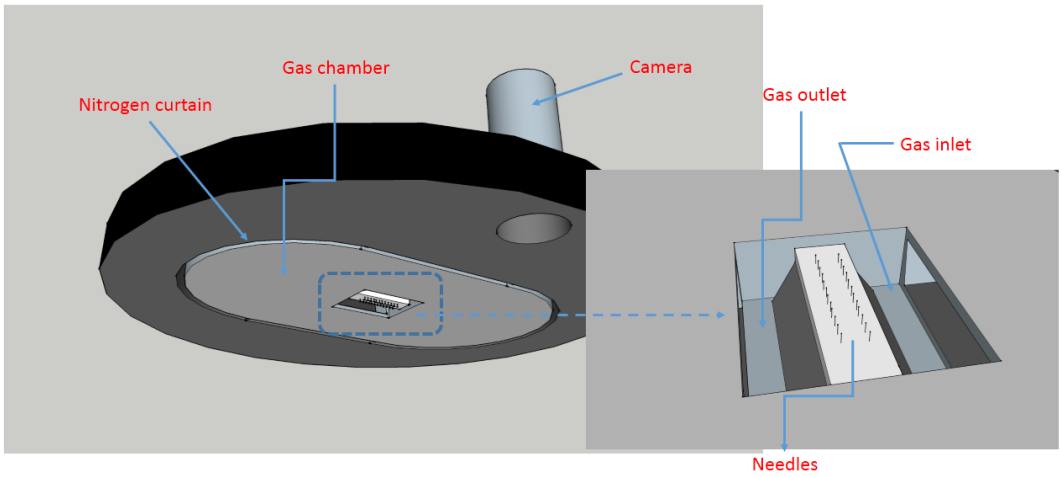

Figure 12: 3D schematic of the print-stage. A gas chamber with an in- and outlet is attached around the print head. The gas chamber and print head are surrounded by a gas curtain system, providing a continuous flow of nitrogen, to avoid reactions of the gas mixture with moisture from the environment.

As already has been explained in section 2.2, a dielectric layer is required between the needle electrodes and the high voltage substrate table and two different configurations of the setup exist, depending on the type of substrate. If the substrate is a dielectric material, the substrate itself serves as the dielectric and the setup is used as shown in Figure 12. If the substrate is a (semi-)conductive material, an extra dielectric layer (260 µm thick Al_2O_3) is positioned between the needle electrodes and the conductive substrate. A 3D schematic of the print-stage for plasma treating conductive substrates can be found in Appendix C.

3.2 Deposition setups

The deposition setups are described in this section. First the PE-CVD setup is addressed, followed by the modification towards the setup for the ALD experiments. In this work titanium tetra-isopropoxide (TTIP) was selected as titanium precursor to deposit titanium dioxide (TiO_2) thin films. TTIP was selected for several reasons, which are addressed at the end of this section.

3.2.1 PE-CVD setup

A schematic view of the PE-CVD µPP setup is shown in Figure 13. All required system modifications are extensively described in Appendix B. N_2 (99.995% purity) was used as carrier gas which was fed into a stainless steel TTIP bubbler, in which the precursor vaporized. The N_2 flow was controlled by a mass flow controller (MFC). The TTIP bubbler was heated to 32 ± 3 °C. The flexible stainless steel line and gas chamber were heated to 50 ± 3°C and 55 ± 5°C, respectively, to prevent precursor condensation. The temperature of the substrate table remained 55 ± 5°C during all the experiments. The exhaust line was connected to a vacuum pump and the pumping speed was controlled by a needle valve and a MFC. For TiO_2 depositions on dielectric substrates, a TTIP precursor flow and pump flow of 25 sccm was used and the oxygen (99.5% purity) flow was varied between 0 and 10 sccm. For TiO_2 depositions on conductive substrates, a TTIP precursor and pump flow of 53 and 75 sccm was used, respectively, in order to maintain a continuous gas flow underneath the dielectric spacer. A schematic view of the PE-CVD setup for conductive substrates can be found in Appendix C. The gas curtain system (not shown in Figure 13) was fed with 500 sccm N_2, in all PE-CVD experiments. The precursor lines and gas chamber were purged before and after depositions for 1 hour with 200 sccm N_2 flow.

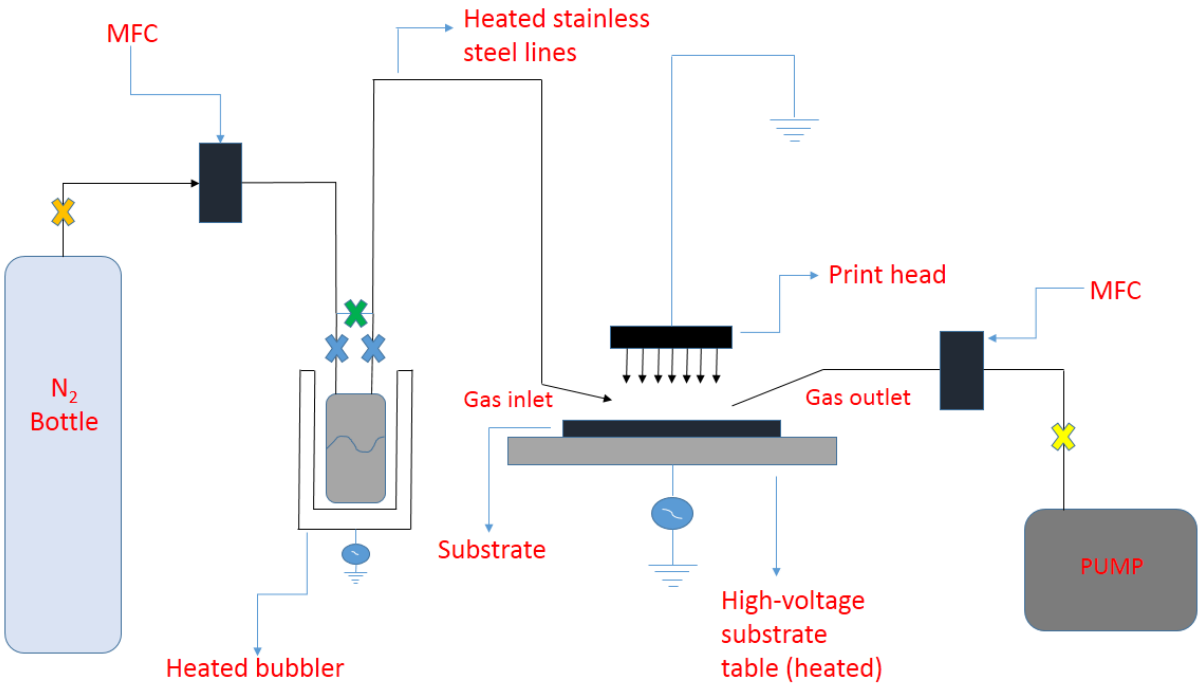

Figure 13: Schematic view of the PE-CVD µPP setup for depositing on dielectric substrates. The TTIP precursor and exhaust flow was 25 sccm and the oxygen flow was varied between 0 and 10 sccm. The temperatures of the bubbler, lines, gas chamber and substrate table were constant in all experiments: bubbler (32 ± 3°C), precursor lines (50 ± 3°C), gas chamber (50 ± 5°C) and substrate table (55 ± 5°C).

3.2.2 Plasma-assisted ALD setup

As already mentioned in the introduction, the µPP can probably be used as a plasma source for a plasma-assisted ALD process and lead to an improvement of the film properties and material quality. The basic principles of ALD can be found in Appendix A. The required hardware modifications to modify the µPP to a plasma-assisted ALD system are described in this section, together with the deposition setup for the ALD experiments.

Since ALD is based on the alternate pulsing of a precursor and a reactant (or plasma) gas, a precursor dosing head was integrated at the print-stage. A schematic view of the modified print-stage is shown in Figure 14. The precursor head is made of aluminum and is designed to evenly distribute the precursor over the surface. The head consists of one central inlet channel and four exhaust channels, which converge into one central exhaust channel. The precursor head was used as one half-cycle in the ALD process, while the plasma print head was used as the second half-cycle, through oxidation with O_2-plasma. A gas curtain system (Figure 14) was designed to separate the precursor and print heads from each other and from the environment in order to avoid reactions with moisture from the environment and with each other.

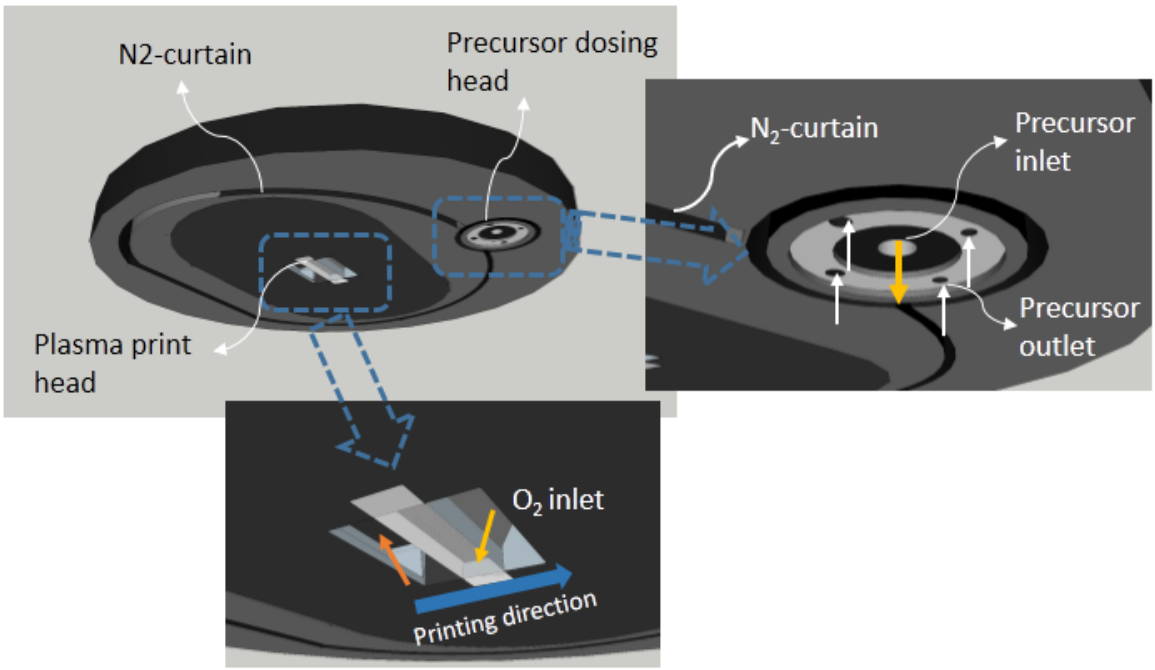

Figure 14: 3D Schematic of print-stage for plasma-assisted ALD setup. A precursor dosing head was integrated in the µPP. Precursor dosing head and plasma head were separated from each other and from environment by a gas curtain system.

ALD reactions are achieved by the alternate shifting of both deposition heads (i.e. plasma and precursor) over the sample's surface. The substrate is located at a fixed position on the substrate table. The different steps of one TiO_2 ALD-cycle with TTIP as precursor and O_2 plasma as oxidant in the plasma-assisted ALD setup are explained in the following, using Figure 15 and Figure 16:

(a) The substrate is exposed to the TTIP precursor by shifting the precursor dosing head over the substrate's surface, the TTIP precursor molecules absorb on the surface. In an ideal situation, only one sub-monolayer absorbs in a self-limiting manner due to the limited number of available surface sites. The self-limiting behavior can be checked by controlling the growth per cycle (GPC) as a function of precursor exposure time.
(b) The precursor dosing head moves away from the substrate, while the plasma head approaches the substrate. Unreacted TTIP molecules and byproducts are removed through the exhaust by a combination of the N_2/O_2 flow with the exhaust flow. Hence the purge step is performed during the transition from the precursor head to the plasma head. Extra purge time can be added, by moving the plasma head over the substrate without plasma ignition.
(c) The substrate is exposed to O_2-plasma, produced by the plasma head. The produced O-species in the plasma (e.g. O-radicals and probably O_3) react with the previously absorbed precursor

molecules, combusting the hydro-carbon ligands of the TTIP molecule (ligands). A TiO_2 monolayer is formed and reactive surface sites are created on which the TTIP molecules chemisorb in the next half-cycle.

(d) The produced byproducts are removed through the exhaust by a combination of the N_2/O_2 flow with exhaust flow, which completes the ALD-cycle. In an ideal situation only one TiO_2 monolayer is formed in one ALD-cycle. The next ALD-cycle is initiated by shifting the precursor head again over the substrate, the TTIP molecules absorb at the previously oxidized surface sites.

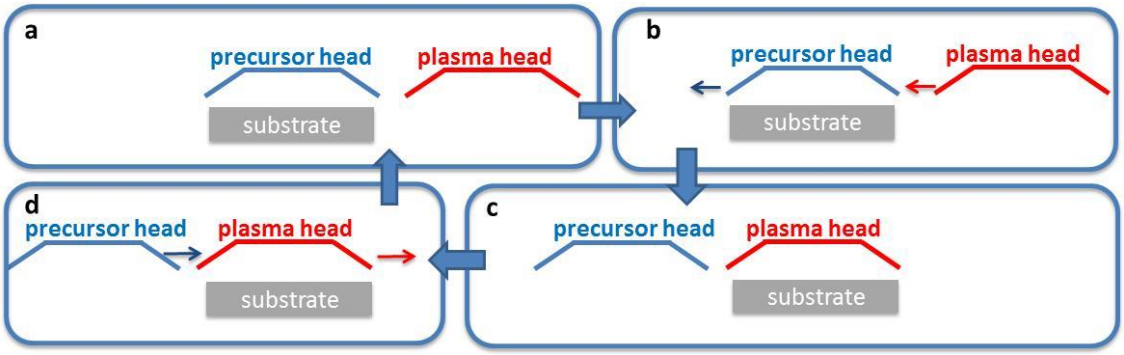

Figure 15: Schematic representation of one ALD cycle in the µ-Plasma assisted ALD setup. The substrate is located at a fixed position, while it is alternatively exposed to precursor and O_2-plasma, through the alternate shifting of the two heads over the substrate.

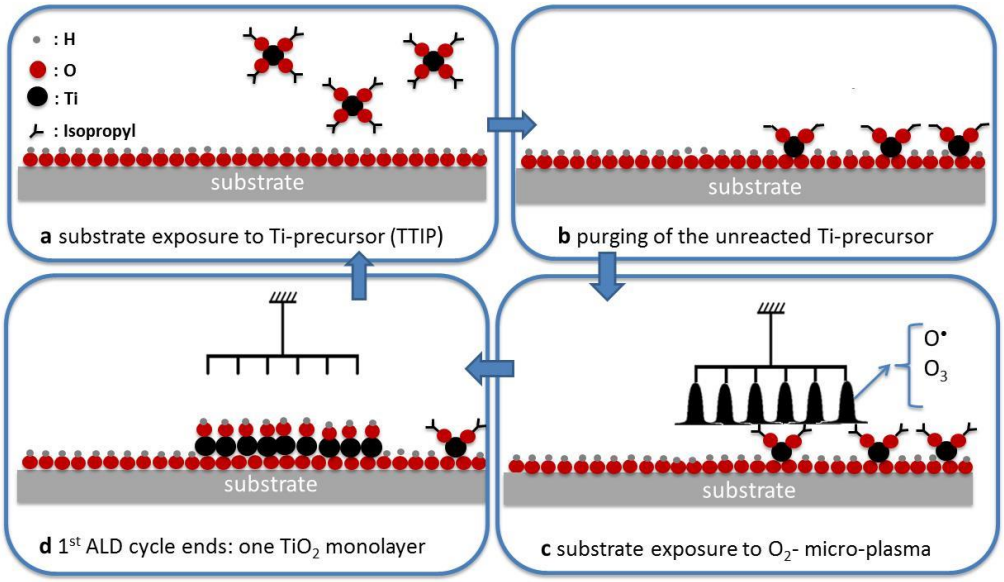

Figure 16: Schematic representation of chemical reactions in one ALD-cycle of TiO_2 in the µPP ALD setup. (a) The substrate is exposed to the TTIP precursor in the first half-cycle, by shifting the precursor head over the sample's surface. The TTIP molecules absorb at the surface, in a self-limiting manner due to the limited amount of available surface sites. (b) The precursor head is shifted away from the surface, while the plasma head approaches the surface. Residual precursor molecules and byproducts are removed through the exhaust. (c) The second half-cycle starts by exposing the surface to O_2-plasma. The produced species (e.g. O-radicals) react chemically with the hydro-carbon ligands of the absorbed TTIP molecules. A TiO_2 monolayer is formed and reactive surface sites are created. (d) Residual species and created byproducts are removed through the exhaust. The next ALD-cycle is initiated by shifting the precursor head again over the substrate's surface.

A schematic view of the µPP ALD setup is shown in Figure 17. The temperatures were kept the same as in the PE-CVD setup (see section 3.2.1), because the temperatures used in other reported ALD processes of TiO_2 with TTIP as precursor vary between room temperature and a few hundred degrees [33,34,35]. The TTIP precursor flow was 25 sccm, which was guided to the precursor dosing head, while 10 sccm O_2 was guided to the plasma print head. The outlet channels from plasma print head and precursor head were connected to vacuum pump and the exhaust flow was controlled by a needle valve and a MFC. The gas curtain system was fed with 2 slm of N_2. The precursor lines and dosing head were purged before and after deposition for 1 hour with 200 sccm N_2 flow.

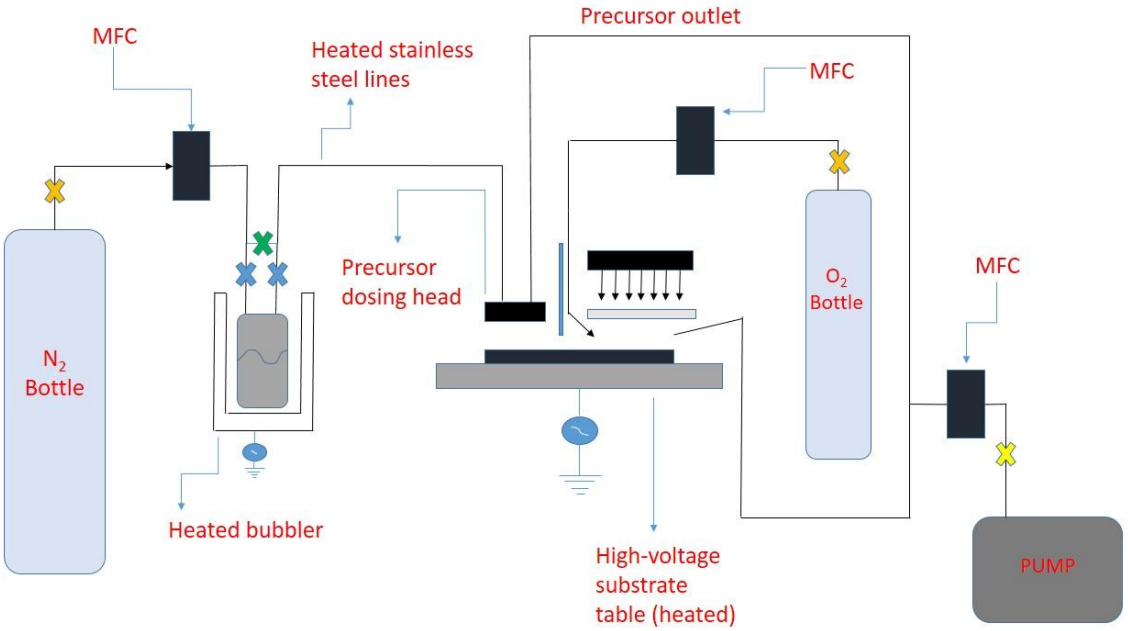

Figure 17: Schematic representation of the µPP ALD setup. The TTIP precursor was guided to the precursor dosing head (25 sccm), O_2 (10 sccm) to the plasma print head, while the gas curtain system was fed with 2 slm N_2. The temperatures were the same as in the PE-CVD experiments. Substrate was positioned at a fixed location on the substrate table while alternatively exposed to the precursor and oxidant pulses.

The amount of precursor exposure and purge time per ALD-cycle is depending on the motion speed of the print-stage, which is variable between 10 and 60 mm/s. The precursor exposure and purge time as function of motion speed are shown in Table 2. The precursor exposure is variable between 315 and 1900 ms, while the purge time between 650 and 3900 ms, for the present setup. Extra purge time was added, by moving the plasma head over the substrate without plasma ignition, which is defined as "Extra purge time" in this work. It is worth mentioning that the precursor exposure time also depends on the length of the dosing head. Since the duration of plasma cannot be changed in every plasma PR, the plasma exposure time was controlled by the number of plasma PR in every ALD-cycle. In one PR, every dot on the substrate is exposed to plasma for approximately 400 µs (Figure 8b) [32]. Therefore the plasma exposure time can be increased by discrete steps of 400 µs, by increasing the number of plasma PR per ALD-cycle. Other spatial ALD systems are mainly operated with a deposition head with separate fixed gas regions (e.g. Figure 50, Appendix A). Therefore the dosing and purge times are dependent to each other and are limited by the motion speed or rotation speed [36,37,38,39]. The motion speed is adapted when an increase/decrease of precursor/reactant exposure time is required, which also affects the other steps in the ALD process. However in the µPP ALD setup, the precursor and plasma exposure times and purge time can be varied independently.

Table 2: Precursor exposure and purge time (between every plasma and precursor exposure step) as function of motion speed of the print-stage.

Motion speed (mm/s)	Precursor exposure time (ms)	Purge time (ms)
10	1900	3900
20	950	1950
30	630	1300
40	475	975
50	380	780
60	315	650

Sample preparation and deposition settings

Two different types of substrates were used for the PE-CVD experiments:

- Pre-cleaned Silicate-glass microscope slides (76x26x1 mm) from Thermo Scientific Menzel-Gläser.
- P-type Si (100) wafer with native oxide.

The ALD experiments were only performed on p-type Si (100) wafer with native oxide. The deposited area was approximately 0.5 cm² for all samples, large enough for all necessary characterization methods, unless otherwise specified. The applied voltage was 5.8 kV_{PP} for all depositions. The distance between consecutive plasma dots was set at 90 µm in the µPP software for all PE-CVD experiments, while 270 µm for all ALD experiments, unless otherwise specified. The samples used for determination of the patterning resolution were all deposited with 270 µm between consecutive plasma dots (PE-CVD and plasma-assisted ALD).

Model system: deposition of metal-oxide thin film

In this work the possibility to deposit metal-oxide thin films with the µPP as plasma source is investigated. An abundance of different metal oxides can be formed, one is titanium dioxide (TiO_2), which was already extensively studied by the PMP-research group [37]. Therefore TiO_2 was chosen as a material to demonstrate the possibility of depositing metal oxides thin films with the µPP. A large variety of different titanium precursors are on the market. The most popularly used Ti precursors for CVD and ALD processes are: Titanium (IV) tetra-isopropoxide (TTIP) [40,41,35]; Titanium (IV) chloride ($TiCl_4$) [42,34,43]; Tetrakis(dimethylamino)titanium(IV) (TDMAT) [44]; Titanium(IV) oxyacetylacetonate; etc. However, TTIP and $TiCl_4$ are predominantly used.

$TiCl_4$ is characterized by a high vapour pressure (12.4 Torr at 25°C) and reaction of $TiCl_4$ with H_2O leads to the production of toxic by-products (i.e. HCl). The vapour pressure of TTIP is 0.13 Torr at 25°C, which is lower than $TiCl_4$ but higher than other alkoxides Ti precursors. TTIP was chosen as Ti precursor for the experiments, because of several reasons: widely studied in other deposition processes (also from PMP research group [37,33]), non-toxic by-products, used in both CVD and ALD – processes, limited reactivity at room temperature and TTIP is inexpensive.

The chemical formula of TTIP is $Ti\{OCH(CH_3)_2\}_4$ and the structural formula is presented in Figure 18a. TTIP is a symmetrical tetrahedral molecule, consisting of a central titanium atom with four bonded

oxygen atoms and a propyl-group to each oxygen atom. The melting and boiling points of TTIP are 17°C and 232°C, respectively, with a flash point of 45°C. As for other precursors, the vapour pressure increases with increasing temperature, as shown Figure 18b.

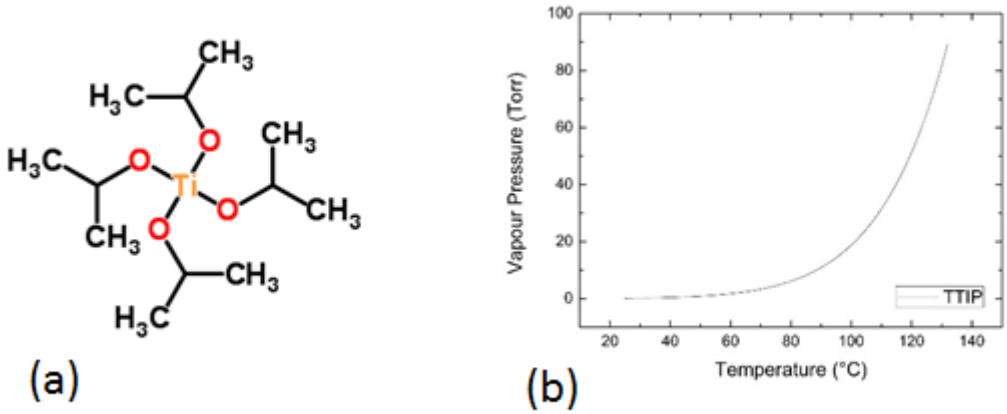

Figure 18: (a) structural formula of TTIP. TTIP is a symmetrical tetrahedral molecule consisting of a central titanium atom with four bonded oxygen atoms and a propyl group to each oxygen atom. (b) Vapour pressure (Torr) as function of temperature.

3.3 Characterization methods

3.3.1 Spectroscopic Ellipsometry (SE)

In this work the ex-situ Woollam M2000 Multi-Angle Spectroscopic Ellipsometer (SE) was used to determine the thickness and refractive index (RI) of the deposited TiO_2 thin films. SE is a non-contact/non-destructive optical diagnostic technique, based on the change of polarization state when linearly polarized light is reflected or transmitted at a material (Figure 19). Linearly polarized light is reflected at the sample's surface and because of the structural and electrical properties of the layers, the polarization state changes [12]. The change in polarization state is measured by a detector, both for parallel (p) and perpendicular (s) to the plane of incidence, for a specific photon energy range. The change in polarization state is expressed by the two parameters delta (Δ) and psi (Ψ), which are measured as a function of wavelength (λ) of the light. The parameter Δ is the phase difference between the initial and the reflected beam and the parameter Ψ is the ratio between the reflected amplitudes [45].

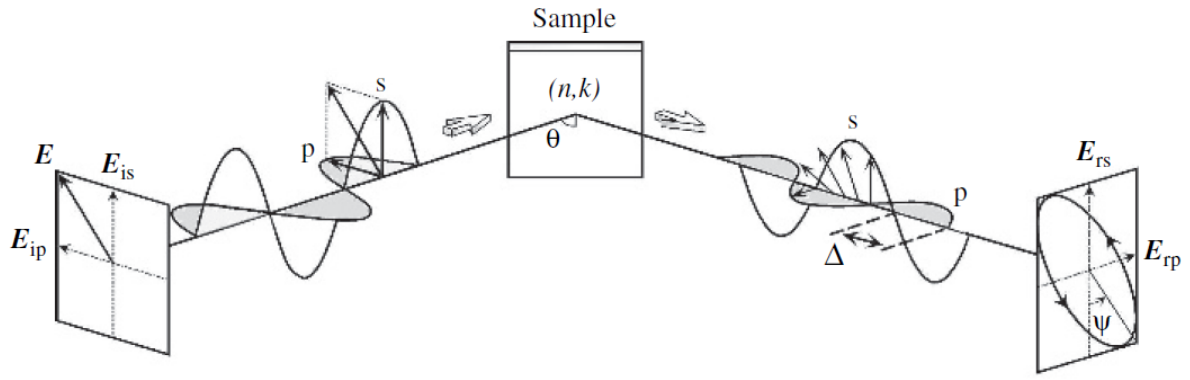

Figure 19: Basic principle of spectroscopic ellipsometry (SE) [12].

In this report both parameters Δ and Ψ were measured as a function of wavelength at three different angles (65°, 70° and 75°), to increase the accuracy of the measurement. The experimental data was modelled with two different optical fit models: Cauchy and Tauclor, in order to determine the TiO_2 film thickness and RI, respectively. The signal below a wavelength of 350 nm was excluded in the Cauchy model, since TiO_2 is not optically transparent below this wavelength region [46]. The reported film thickness was determined by averaging three different measurement points on a TiO_2 sample, the corresponding standard deviation was used as the measurement error.

3.3.2 X-Ray Photoelectron Spectroscopy

XPS is a widely used ex-situ diagnostic technique to investigate the chemical and/or electronic states and the chemical composition of a material [47,45]. XPS is based on measuring the binding energy of the elements in the film. A schematic view of the working principle of XPS is presented in Figure 20. A mono-energetic X-ray source (Al Kα) is used to irradiate high energetic photons on the material under investigation. The target material consequently emits a core electron and the kinetic energy (E_{Kin}) of the emitted electron is measured by the spectrometer (Thermo Scientific K-Alpha spectrometer). The spectrometer is placed perpendicular to the substrate while the X-ray source is placed at an angle of 65° [48]. The electron's kinetic energy depends on the binding energy of the electron to the nucleus (E_B), the X-Ray photon energy of the source (hv) and on the spectrometer work function $\varphi_{spec.}$, according to Eq. 4:

$$E_{kin} = hv - E_B - \varphi_{spec} \tag{4}$$

The spectrometer work function is determined by calibration of the spectrometer and the photon energy is known and constant, since the X-rays are mono-energetic. Hence measuring the kinetic energy of the emitted electron, is indirectly a measurement of the binding energy of the electron to the nucleus. The detected electron signals are counted and plotted in a spectrum.

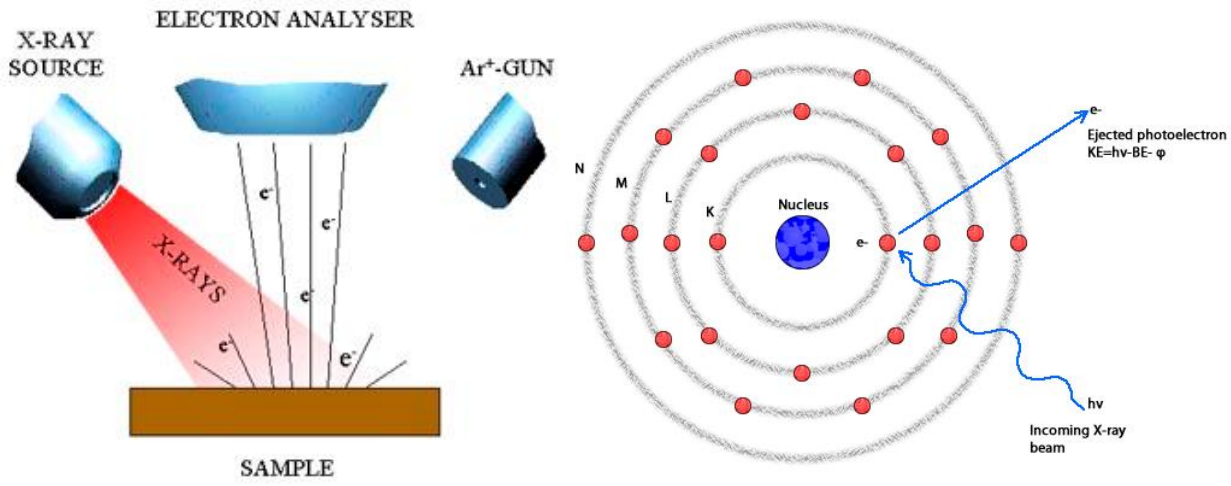

Figure 20: Schematic of working principle of XPS [47]. High energetic photons (X-rays) are irradiated at a sample's surface, causing emission of core electrons. The emitted electrons are detected by the spectrometer and used to determine the chemical composition of the material under investigation.

A XPS spectrum shows the counts per second of the detected electron signal as a function of binding energy in eV, which is in principle a distribution of the detected binding energies. Therefore a XPS spectrum shows the abundance of binding energies present in the material under investigation. Since each atomic element is characterized by a discrete set of electronic states, due to different quantum states, each element is characterized by a specific set of XPS intensity peaks. Therefore comparing the detected XPS spectrum with a known database, enables the possibility to determine the elements and chemical states present in the material. However analysis of a XPS spectrum can be a complex problem, since multiple peaks can be broadened and even overlap [47]. Therefore the spectrum has to be deconvoluted into separate peaks. Peak broadening can occur due to influence of the material on the kinetic energy of the emitted electrons. Moreover the emission of electrons out the substrate results in a positively charged surface, which affects the electron's kinetic energy [12]. The elemental

concentration of the material is determined by integrating the corresponding peaks, which requires the application of sensitivity factors used to scale the distribution peaks [47].

Since electrons have a limited escape depth out of a material, a XPS measurement is limited to information about the top 10 nm layer of the film [48]. However the XPS system is equipped with an Ar-ion gun, enabling depth profiling by sputtering the material under investigation and thereby etch some material away. Ion energies between 100 eV and 3 keV are possible with the used XPS system. In this work the substrates were measured as-deposited and after 60 seconds sputtering with a 500 eV Ar^+ ion beam. An additional benefit of the sputtering step is the removal of hydrocarbon surface contamination of the deposited film. However sputtering can lead to positive charge accumulation at the substrate due to the positively charged Ar^+ ions and some elements can be sputtered more than others, known as preferential sputtering [47].

XPS line-scan:

The patterning resolution of the µPP was determined by means of XPS line-scan, the mechanism is presented in Figure 21. Multiple XPS measurements were performed on different locations on the sample, equally spaced by 60 µm. The result is a spectrum showing the elemental concentration of the material as a function of distance, which enables the possibility to determine the line-width of a deposition. A proof of concept can be found in Appendix D.

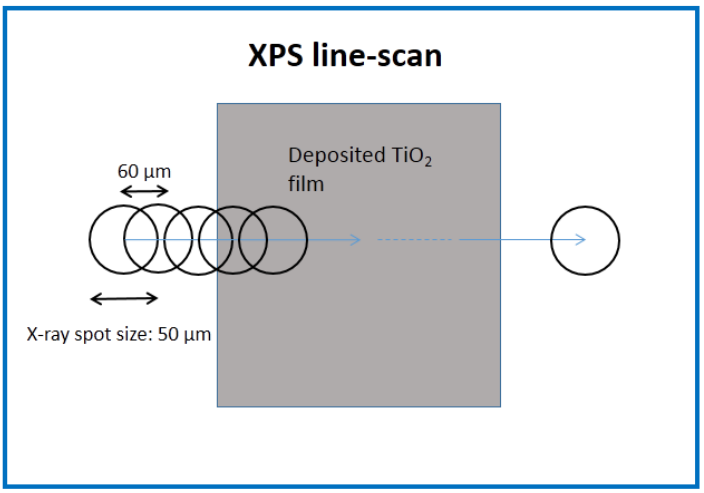

Figure 21: Schematic representation of XPS line-scan. Multiple XPS measurements are performed equally spaced by 60 µm. The result is a spectrum showing the elemental concentration as function of distance.

3.3.3 Atomic Force Microscopy

Atomic Force Microscopy (AFM) is used to study the surface morphology and roughness of the deposited TiO_2 films. With AFM, 3D images of both conducting and insulating surfaces can be made with a precision up to atomic level [49]. A schematic of the working principle of AFM is presented in Figure 22. A sharp tip with a specific spring constant *k* is mounted in a cantilever, which oscillates at its resonance frequency. The cantilever tip is brought in close proximity with the surface, where various attractive and repulsive forces between the tip and surface, for example Van Der Waals forces, dipole forces, etc. influence the resonance frequency [49]. Leading to a deflection of the cantilever tip, which is monitored by a laser beam pointed at the tip. The laser beam is reflected towards a segmented photodiode and the deflection of the cantilever tip can be determined by the photocurrent detected in each part of the photodiode. The relative photocurrent is consequently transformed in a voltage signal, proportional to a distance [49].

AFM can be operated in different modes: contact/non-contact mode and a semi-contact mode or tapping mode [49,50]. In this thesis the Nova NT-MDT Solver AFM system was used in tapping mode. In tapping mode, the tip oscillates close or at its resonance frequency by using a small piezoelectric element, while the tip starts tapping the surface. The resonance frequency and amplitude of the oscillation is thereby affected and the amplitude is kept constant through an integrated feedback system by adapting the distance between cantilever tip and sample's surface [49].

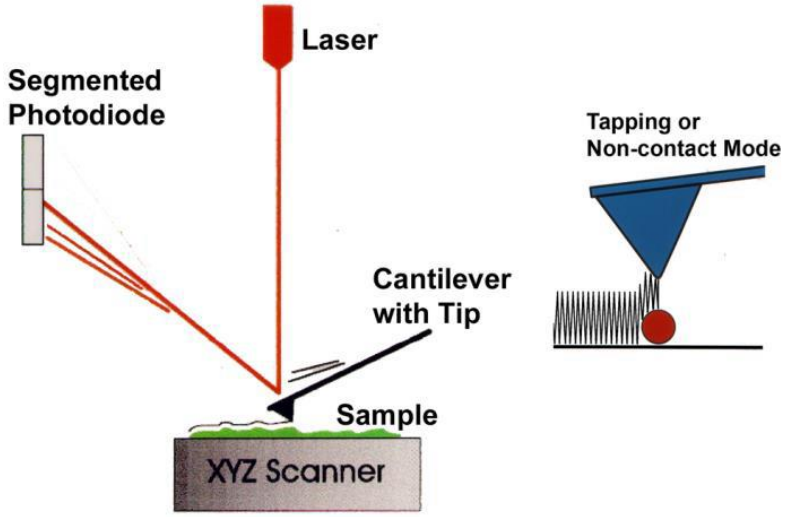

Figure 22: Schematic representation of Atomic Force Microscopy (AFM) in tapping or non-contact mode.[45]

3.3.4 Scanning Electron Microscopy

Scanning electron microscopy (SEM) is a high resolution microscopy technique. The resolution of an optical microscope is limited by the wavelength of the light source and therefore limited to approximately 200 nm [51]. However radiation with a shorter wavelength can increase the resolution significantly, which is done in SEM, by using a focused beam of energetic electrons. The electrons are accelerated and focused onto a sample's surface and interact with the atoms in the sample, leading to various scattering events. The electron beam scans the sample's surface in two dimensions and information about the composition and surface topography can be obtained by detecting and analyzing the scattered signals.

The electrons can either be elastically or inelastically scattered. In an elastic scattering event, the primary electron (PE), typically a high-energy electron, interacts with the nucleus of the atom. The PE loses a small part of its energy and is reflected or back-scattered. The elastically scattered electrons are referred to as back-scattered electrons (BSEs). Heavier elements in the sample scatter more electrons than lighter elements, leading to a difference in detected electron density. Therefore different film layers can be visualized by detecting the BSEs [49,52]. In an inelastic scattering event, the energy of the PE is almost completely transferred to the atom, resulting in the emission of secondary low-energy electrons. The amount of detected secondary electrons depends on the angle of incidence of the PE beam with the sample's surface, leading to a contrast difference between flat and steep surfaces. Therefore topography images of the sample's surface can be made by detecting the secondary electrons [52]. However the PE can kick out an inner shell electron, resulting in the formation of an open vacancy, which will be filled by a higher orbital electron and a small amount of energy is released in the form of a photon or X-ray. However the energy can also be transferred to an outer orbital electron, resulting in an ejected electron, known as an Auger electron [52].

Different detectors are required to detect and analyze the different types of scattering signals. The electron acceleration energy of the primary beam together with the beam spot size determine the resolution of the SEM, which can be better than 1 nm [49]. SEM is operated at high-vacuum. In this work the Zeiss Sigma SEM was used.

3.3.5 Raman Spectroscopy

Raman spectroscopy is used to determine vibrational and rotational modes in a system, by inelastic scattering of monochromatic light on a sample's surface. The monochromatic light interacts with the atoms and molecules in the target material, causing vibrations (phonons) in the molecules and thereby promoting the vibrational energy state of the molecule to a higher state. The new energy state is a virtual temporarily state and relaxes consequently to a stable stationary state by the emission of a photon [53]. The light is elastically scattered if the frequency of the initial and the emitted photon is the same, the type of scattering is known as Rayleigh scattering [54].

However when the frequency and therefore the energy of the emitted photon is different from the initial photon, the light inelastically scattered and known as Raman scattering. The frequency of the emitted photon can shift lower or higher than the initial frequency. When the frequency is lower, the photon transferred energy to the lattice vibrations and a phonon is created. The downward shift in frequency is known as the Stokes shift. The opposite, when the frequency is higher, the photon gained energy from the lattice vibrations and a phonon is destroyed. The upward shift in frequency is known as the anti-Stokes shift [54]. Both Stokes and anti-Stokes shifts are known as Raman shifts. In Raman scattering, the energy shift between the initial and the emitted photon is the amount of energy of one vibrational unit and therefore characteristic for each type of molecule [54].

All three situations are depicted in Figure 23. Anti-Stokes is rarely observed at room temperature since most molecules are in their ground state at room temperature. The detected signals are plotted as a function of Raman shift (cm^{-1}) in a Raman spectrum. In this work the In-via Renishaw Raman spectrometer with a laser of 514.5 nm was used.

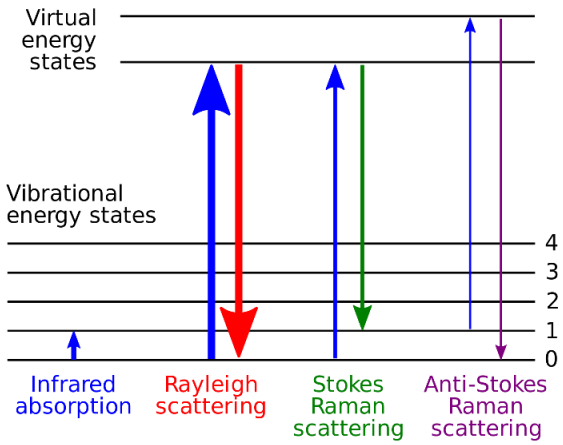

Figure 23: Energy level scheme explaining the three different scattering events. In Rayleigh scattering, the photon frequency of the emitted photon is the same as the initial photon and no energy is exchanged with the lattice vibrations. Raman scattering is divided in Stokes and Anti-Stokes shift. In Stokes shift, energy is transferred from the initial photon to the lattice vibrations and a phonon is created, resulting in a decreased photon frequency. While in Anti-Stokes, the opposite occurs and a phonon is destroyed, resulting in an increased photon frequency.

3.3.6 Rutherford Backscattering Spectrometry and Elastic Recoil Detection

Rutherford Backscattering Spectrometry (RBS) and Elastic Recoil Detection (ERD) are ex-situ diagnostic techniques, used to determine the absolute elemental composition and atomic areal density of the material under investigation. Schematic representations of RBS and ERD are presented in Figure 24. The fundamentals of both methods will be addressed, briefly, in this section. In RBS, a high energy (1.8 – 2.0 MeV) ion beam (He^{2+} or He^{+} ions) is directed perpendicular to a target sample. The positively charged He^{+} ions cause elastic collisions with the heavier target atoms in the sample and are backscattered. A rotational detector is placed at specific angles and measures the remaining kinetic energy of the backscattered ions (Figure 24). The energy of the initial He^{+} ion, the energy of the backscattered ion together with the scattering angle are used to determine the mass of the target atom, by applying conservation of energy and momentum in an elastic scattering event [45]. Since each atomic element is characterized by a unique mass, the elemental composition of the target material can be determined by RBS measurements. The energy loss of the initial He^{+} ions is dependent to the density and composition of the target material and to the penetration depth of the ions in the target material [47]. Hence RBS can be used for depth profiling a material. Besides the elemental composition, RBS can be used to determine the atomic areal density of the target atoms, N_s (atoms/cm²). Therefore the probability for an elastic scattering event between an incoming He^{+} ion and the target atom has to be taken into account. Assume Q is the number of incoming ions and Q_D the backscattered fraction of Q in an angle Ω, than N_s can be determined according to Eq. 5:

$$Q_D = \sigma(\theta)\Omega N_S \tag{5}$$

in which $\sigma(\theta)$ is the central-force Rutherford backscattering cross-section [45,55]. Therefore by measuring Q_D, the atomic areal density of the target atoms N_S can be determined, since Q, (θ) and Ω are known.

However RBS cannot be used to detect hydrogen atoms, since helium atoms are heavier than hydrogen atoms and therefore no backscattering event occurs. A similar method as RBS can be used to detect hydrogen, known as ERD. In ERD, the high energetic He^{+} ions are directed to the target sample at very small incident angle (Figure 24), causing elastic recoil collisions and thereby kicking out the lighter target atoms. The ejected particles are measured instead of the scattered He^{+} ions, by a detector positioned at small incident angle with respect to the sample's surface [47]. The kinetic energy of the ejected particle together with the scattering angle can be used to determine lighter particles [45].

In this work, RBS/ERD measurements were performed to determine the chemical composition, O/Ti ratio and the atomic areal density (atoms/cm²) of the deposited TiO_2 films. Moreover, the deposition rate (atoms/nm².cycle), atomic density (atoms/cm³) and elemental mass density (g/cm³) was calculated from the atomic areal density. The RBS/ERD measurements in this work have been performed with by Detect99.

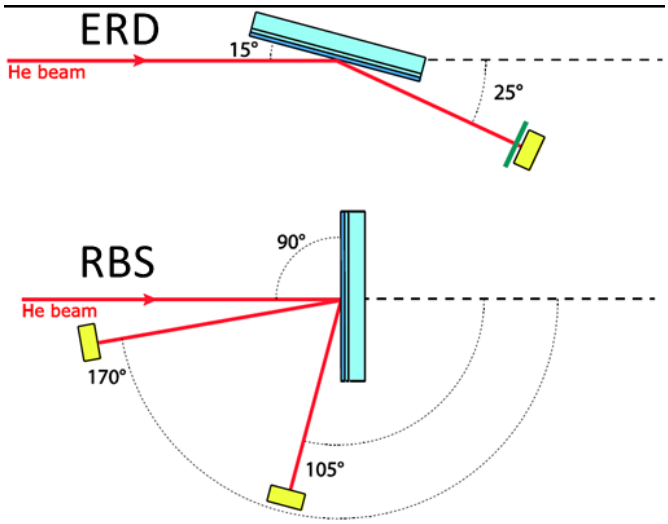

Figure 24: Schematic representations of Elastic recoil detection (ERD) and Rutherford backscattering spectrometry (RBS). In RBS, high energetic He^+ ions are directed perpendicular to a sample's surface, causing elastic collisions with heavier target atoms and are consequently backscattered. The energy of the backscattered He^+ ions are measured by a rotational detector and can be used, together with the scattering angle, to determine the mass of the target atoms. In ERD, the target sample is positioned at very small incident angle with the He^+ ion-beam, causing elastic recoil collisions with the lighter hydrogen atoms. The energy of the ejected hydrogen atoms is consequently measured by a detector, which is placed at very small incident angle with the sample's surface.

4. Results and Discussion

In this chapter the results are presented. In the first section the TiO_2 films deposited by guiding the vaporized TTIP precursor into the discharge volume (PE-CVD mode) are characterized. The possibility to achieve an improvement in material quality, by the spatial separation of precursor and reactant gas (Plasma-assisted ALD mode) is investigated in the second section. The TiO_2 films deposited by the two processes are compared in terms of growth behavior, chemical composition, surface morphology and printing resolution. During analyses of the TiO_2 films on glass substrate, crystallized particles were observed which are discussed in the last section of this chapter.

4.1 PE-CVD of TiO_2 thin films

The depositions were performed on glass (dielectric) and Si (conductive) substrates. The growth rate of the TiO_2 layers are reported in the first section, followed by the chemical analysis by XPS in the second section. The high resolution Ti2p, O1s, N1s and C1s peaks are studied in more detail. The morphology and surface roughness of the films are discussed in the third section. The patterning resolution of the µPP in PE-CVD mode is investigated by means of XPS line-scan in the last section.

4.1.1 Growth rate

The film thickness as a function of plasma PR (i.e. plasma exposure time), is presented in Figure 25. The results are shown for films deposited on glass substrates, with and without adding 10 sccm oxygen to the gas mixture and on Si substrate without oxygen to the gas mixture. Due to the limitation in system design, no oxygen could be added to the gas mixture when Si was used as the substrate. The applied voltage was 5.8 kV_{PP} and remained the same during all experiments. It can be seen that in all three conditions the growth rate changes linearly with increasing the number of plasma PR. The growth rate was calculated from the slope of the linear fit and is reported in Table 3. The growth rate on the glass substrate decreased from 2.3 to 2.0 nm/PR after adding oxygen to the gas mixture.

Table 3: Growth rates for PE-CVD deposited TiO_2 films on glass substrate with and without 10 sccm O_2 to the gas mixture and on Si substrate.

Substrate	Gas mixture	Growth rate (*nm/PR*)	Growth rate (*nm/ms*)
Glass	25 sccm TTIP; 0 sccm O_2	2.3 ± 0.2	5.7 ± 0.5
Glass	25 sccm TTIP; 10 sccm O_2	2.0 ± 0.2	5.0 ± 0.5
Si	53 sccm TTIP	1.3 ± 0.2	3.25 ± 0.5

The growth rate on Si substrate was lower than the growth rate on glass substrate. An extra dielectric layer is required when plasma printing is performed on a conductive substrate, hence the distance

between the high voltage substrate table and the needle electrodes increased, compared to the setup for dielectric substrates (Figure 9). Moreover, the gas flow and pump speed were different in the two configurations. Therefore the difference in growth rate is most likely explained by the difference in configurations which were used for PE-CVD. Significantly smaller growth rates in the range of 0.3 – 0.34 nm/s were reported in other DBD-CVD processes of TiO_2 with TTIP as precursor[57,58]. However the used setups were planar DBD configurations and therefore difficult to compare with the µPP setup.

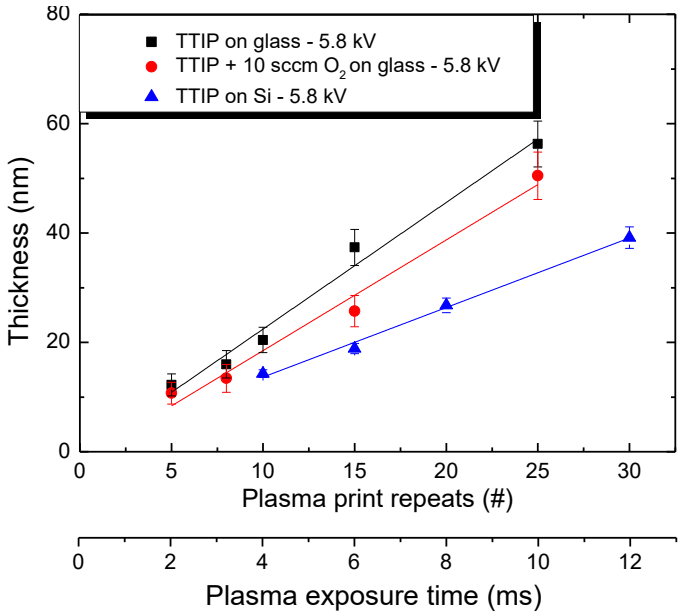

Figure 25: Thickness (nm) of TiO_2 films as function of plasma print repeats (PR) and plasma exposure time (ms). Depositions were performed on glass substrates with only TTIP to the gas mixture (black), with TTIP and 10 sccm O_2 (red), and on Si substrate (blue) with only TTIP to the gas mixture. The applied voltage was 5.8 kV_{PP} for all the experiments.

4.1.2 Chemical and optical properties

XPS measurements were carried out to determine the chemical composition of the TiO_2 films. XPS measurements were performed on as-deposited films and after sputtering with Ar^+ ions. The sputtering step was performed to obtain information about the chemical composition in the bulk of the deposited TiO_2 film (i.e. without influence of hydrocarbon surface contamination). The result of XPS measurements on TiO_2 samples deposited on glass substrate with and without adding O_2 to the deposition gas mixture and on Si substrate are presented in Table 4. TiO_2 films contained carbon and nitrogen as impurities.

The O/Ti ratio varied between 2.60 and 2.15 without sputtering, by changing the deposition conditions (Table 4), suggesting a layer over-stoichiometry. It is expected that the presence of OH-groups are the reason for the over-stoichiometry. The O/Ti ratio varied between 2.07 and 1.89 after sputtering, by changing the deposition conditions. However this ratio might be affected by the sputtering step (section 3.3.2). All elemental concentrations reported in the following are bulk values, determined after sputtering. As it has already been discussed, the O-related plasma species, e.g. O- and OH radicals, react with the isopropyl ligands of TTIP molecule leading to formation of volatile byproducts (e.g. CO_2, H_2O, etc.) and a less carbon- containing TiO_2 film (Table 4). The amount of nitrogen in the films deposited on glass substrate decreased from 3.4 to 1.7 % by increasing the O_2 flow from 0 to 10 sccm. Nitrogen was used as the carrier gas and for the gas curtain system. OES measurements were performed to identify the active species in the plasma, the spectra can be found in appendix E.

However, atomic nitrogen could not be detected with the used OES system, since the system was limited to a minimum detection wavelength of 200 nm (a vacuum UV system is required to detect wavelengths lower than 200 nm) and the dominant atomic nitrogen peaks are located at 149 and 174 nm [59]. Moreover, NH^* and N_2^* are located at 336 and 337 nm, respectively[60]. However, it was not possible to distinguish the two peaks due to the resolution of the used OES system. Nonetheless N_2^+ species (391 nm[61]) were detected which require an energy of 15.5 eV [28], significantly larger than the amount of energy required to dissociate a N_2-molecule (9.7 eV)[28]. Therefore the presence of atomic nitrogen in the plasma is expected. The amount of nitrogen decreases by increasing O_2 flow, which is explained by the positive electron affinity of oxygen. Atoms and molecules with positive electron affinities have the tendency to acquire an electron and form negative ions, which results in a corresponding decrease in electron density in the plasma [28]. Therefore, presence of oxygen in the gas mixture can reduce the production of atomic nitrogen.

The carbon and nitrogen content in the TiO_2 films on Si substrate was measured between 7.5 and 0.5% respectively, which were lower than the amount of carbon and nitrogen in TiO_2 films deposited on the glass substrate. The following hypothesis is put forward to explain the lower amount of nitrogen in TiO_2 films on Si substrate. The average electric field strength of the plasma on conductive substrates is lower than on dielectric substrates with the same applied voltage, due to the larger distance between the high voltage substrate table and the needle electrodes (Figure 9). The decreased electric field strength results in a decreased plasma energy density on conductive substrates and presumably to a reduced production rate of atomic nitrogen. This hypothesis could also explain the lower growth rate on Si substrates in comparison with glass substrates (section 4.1.1). Significantly lower amounts of carbon were reported in [62,63,64]. In a recent study by Battiston et al[62], TiO_2 films were deposited with a low pressure PE-CVD setup with N_2/O_2/TTIP gas mixture at substrate temperatures between 100 and 250°C and Si as substrate. They reported a carbon content lower than 3%. While in a recent study by Gazal et al[64], TiO_2 films were deposited on Si substrate with a PE-CVD µ-wave torch at atmospheric pressure, argon as carrier gas and substrate temperature between 50 and 200°C. They reported a carbon content less than 4%. An overview of other reported CVD systems and the corresponding properties can be found in Table 10 (Appendix F).

Table 4: Chemical composition of the TiO_2 films deposited on glass and Si substrates, determined by XPS. Measurements were performed on as-deposited and after 60 seconds of sputtering with 500 eV Ar^+ ion beam. All samples were deposited with an applied voltage of 5.8 kV_{PP} and 25 plasma PR.

Condition	Substrate	As-deposited (%) ± 1.0				± 0.1	After sputtering (%) ± 1.0				± 0.1
		Ti	O	C	N	O/Ti	Ti	O	C	N	O/Ti
25 sccm TTIP; 0 sccm O_2	Glass	18.6	48.3	29.0	4.1	2.60	28.0	57.8	10.8	3.4	2.07
25 sccm TTIP; 5 sccm O_2	Glass	19.2	48.2	31.4	1.2	2.50	30.3	61.2	6.8	1.7	2.02
25 sccm TTIP; 10 sccm O_2	Glass	20.3	52.2	24.2	3.1	2.57	31	62.4	4.9	1.7	2.01
53 sccm TTIP; 0 sccm O_2	Si	25.0	53.6	20.0	1.3	2.15	31.8	60.2	7.5	0.5	1.89

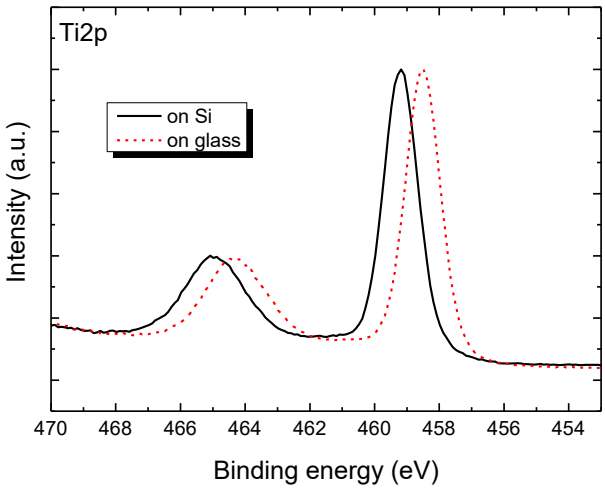

Figure 26: High resolution XPS spectra of the titanium Ti2p peak in as-deposited films on glass (red) and Si (black) substrates.

High resolution XPS spectra of titanium Ti2p, oxygen O1s, nitrogen N1s and carbon C1s peaks were recorded and used to determine the elemental concentration (Table 4) and the chemical environment of the atoms. The high resolution titanium Ti2p peak is presented in Figure 26. Two peaks are observed, at a binding energy values of 459 and 465 eV. The peak at 459 eV represents the spin orbit $Ti2p_{3/2}$ [65,66,67,63,68], while the peak at 465 eV represents the $Ti2p_{1/2}$ spin orbit [65,69,70,71]. Both spin orbits correspond to the Ti^{4+} oxidation state in TiO_2 [72] and no other peaks are observed, indicating that Ti^{4+} is the dominant oxidation state of titanium in the film. The Ti2p peak is reported for as-deposited samples because sputtering with Ar^+ ions leads to a change in the oxidation state of Ti from Ti^{4+} to Ti^{3+} or even lower [37,73,74,75]. The Ti2p peak of the film deposited on glass substrate is shifted by 0.6 eV to lower binding energies, which can be explained by the influence of titanium bound to nitrogen in TiN bonds[76].

The high resolution O1s spectra and the corresponding deconvolution is shown in Figure 27a. The peak with the highest intensity at 530.7 eV corresponds to Ti-O bond [67,72,77] and the peak at 532 eV can be assigned to C-O, C=O [71,72] and N-TiO_2 [70,78] bonds. However the Ti2p peak shift suggests the presence of N-TiO_2 bonds in TiO_2 film deposited on glass substrate and not on Si substrate. Therefore the 532 eV peak can be predominantly attributed to C-O and C=O bonds.

The nitrogen N1s spectra of the as-deposited films and the corresponding deconvolution is presented in Figure 27b. The N1s peak of the film on glass substrate can be deconvoluted to two peaks at 400 and 401.9 eV. The peak at 400 eV can be attributed to anionic N^- species in O-Ti-N bonds [70,78], chemisorbed N_2 molecules and NO_x species [71,72]. Since the N-TiO_2 bond was also observed in the O1s spectra at 532 eV, the peak at 400 eV can be predominantly attributed to anionic N^- species in O-Ti-N bonds [78]. The second peak at 401.9 eV is significantly lower and can be assigned to N species in Ti-O-N bonds [70,78]. As it can be seen in Figure 27b, the intensity of the N1s peak for the film deposited on Si substrate was considerably lower and the peak position was at 401 eV, which can be attributed to absorbed N, NO and NO_2 species[70].

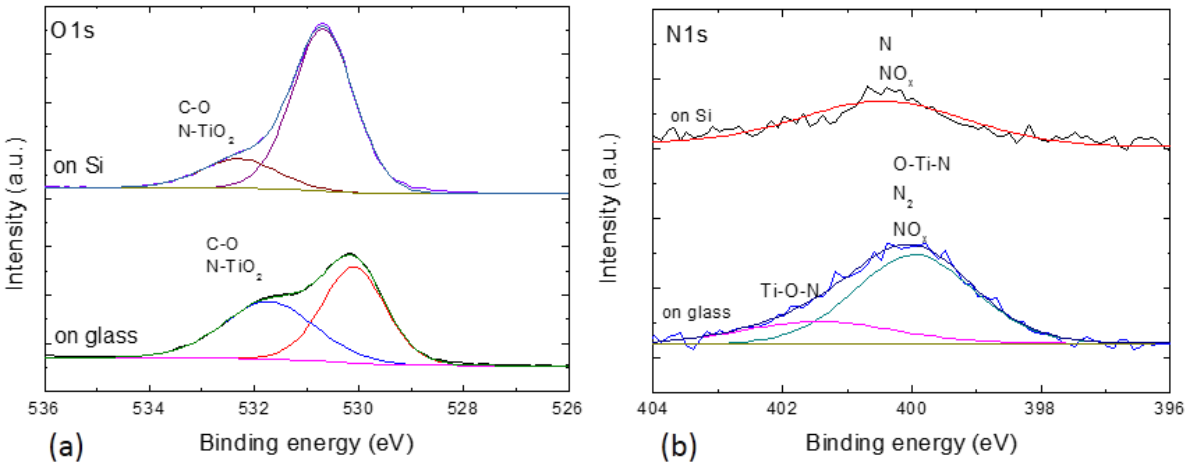

Figure 27: High resolution XPS spectra of (a) oxygen O1s and (b) nitrogen N1s peaks. The spectra were recorded on as-deposited PE-CVD films on glass and Si substrates.

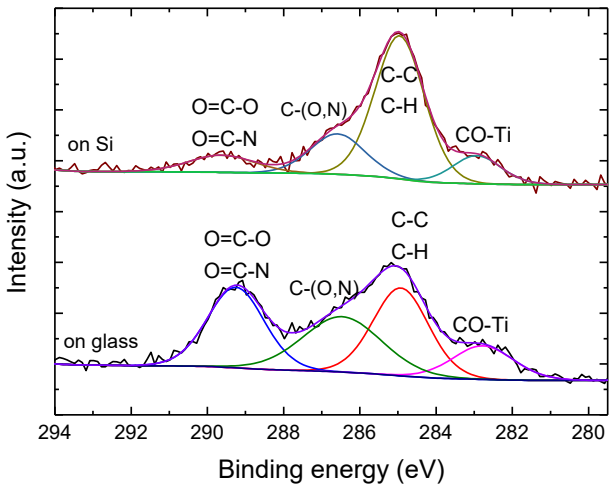

Figure 28: High resolution C1s XPS spectra of the PE-CVD films recorded after sputtering on glass and Si substrates.

The carbon C1s spectra of the films deposited on glass and Si substrates are shown in Figure 28. The peak at 289.6 eV can be assigned to C-species in O=C-O and O=C-N groups [69,76]. The large intensity difference between the peak in films deposited on Si and glass substrate is explained by the lower amount of nitrogen in TiO_2 films deposited on Si substrate, as was shown in Table 4. The peak at 286.6 eV attributes to C-O and C-N bonds [37,76,79], while the peak at 285 eV can be assigned to C-C and C-H bonds [67,77,76,80]. The peak at 282.9 eV is most likely formed due to sputtering during XPS measurement [81] and can be assigned to C-species bonded in CO-Ti groups[80,82]. Other works also reported Ti-C bonds at 282 eV after sputtering, however no peak at 282 is observed in our measurements [37,83].

The RI (at 632.8 nm) of the TiO_2 layer was measured by SE adopting the Cauchy function. The value of RI was 1.81 for a 50 nm thick TiO_2 film. A similar value of RI (1.8 – 2.1) was reported in [62], where TiO_2 films were deposited in a low pressure PE-CVD setup with TTIP as precursor and substrate temperature between 120 and 250°C. However, high density amorphous TiO_2 films are characterized by a RI between 2.1 – 2.3 [34,63], which suggests that the mass density of the deposited TiO_2 films in this work is rather low.

In conclusion, XPS measurements showed carbon and nitrogen as impurities in the deposited TiO_2 films. The lowest amount of carbon measured was 4.9%, when glass was used as substrate. In case of Si substrate, the carbon content was measured to be 7.5%, which is significantly higher than reported in other PE-CVD processes with Si as substrate and TTIP as precursor [62,63,64]. Moreover, the RI is in general relatively low compared with other PE-CVD processes (Table 10).

4.1.3 Morphology and surface roughness

The morphology and surface roughness of the TiO_2 films deposited by PE-CVD on glass and Si substrates are presented in this section. Figure 29 presents SEM images of PE-CVD TiO_2 films deposited on glass substrate with only TTIP (Figure 29a) and TTIP and 10 sccm O_2 (Figure 29b) to the gas mixture. As it can be seen from the images, the films were amorphous (as confirmed by Raman spectroscopy) and the surface is composed of agglomerated particles and the size of the particles decreased upon adding oxygen to the gas mixture. The average feature size and number of them are reported in Table 5, averaged over three images. AFM images of PE-CVD TiO_2 films deposited on glass substrate, with and without 10 sccm O_2 to the gas mixture and on Si substrate are shown in Figure 30. The root mean square (R_{MS}) roughness was 11 nm when only TTIP was used (Figure 30a) and decreased to 4 nm upon adding oxygen to the gas mixture (Figure 30b). The surface of TiO_2 film on Si substrate (c) was smooth with R_{MS} value of 0.25 nm. The same R_{MS} value was measured for a pristine Si substrate with native oxide. Figure 31 shows SEM images of TiO_2 film on Si substrate (Figure 31a) and a cross-sectional SEM image (Figure 31b). The images showed a smooth and uniform surface. Similar values of R_{MS} roughness were reported in [57,68]. In [57] TiO_2 films were deposited on a glass substrate in an atmospheric pressure DBD-CVD setup with TTIP as precursor, they reported a R_{MS} roughness between 10 and 21 nm (scan size 10 x 10 µm). While in [68] TiO_2 films were deposited on Si substrate by a hydrolytic CVD setup at atmospheric pressure and room temperature with TTIP as precursor, a R_{MS} value of 0.28 nm (scan size 0.5 x 0.5 and 10 x 10 µm²) was reported.

Table 5: Average particle size, number and R_{MS} roughness for TiO_2 films deposited on glass substrate with and without O_2 to the gas mixture and on Si substrate.

Substrate – gas mixture	Average particle size (nm²)	Average particle number / µm²	R_{MS} surface roughness
Glass – 25 sccm TTIP	1004 ± 386	243 ± 103	11 ± 1 nm
Glass – 25 sccm TTIP; 10 sccm O_2	377 ± 179	223 ± 116	4 ± 0.5 nm
Si – 53 sccm TTIP	/	/	0.25 nm

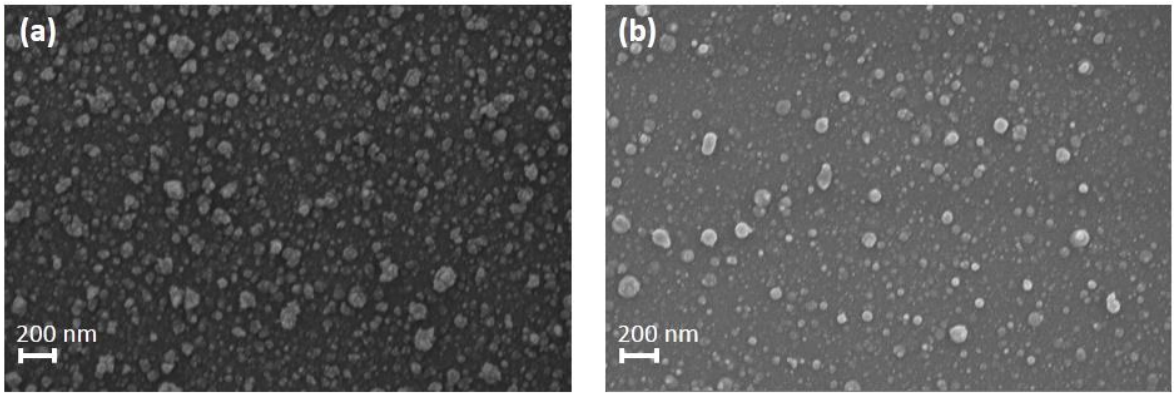

Figure 29: SEM images of PE-CVD TiO_2 films deposited on glass substrate with (a) only TTIP and (b) TTIP and 10 sccm O_2 to the gas mixture with V_{PP} = 5.8 kV and 30 plasma PR. Due to dielectric nature of TiO_2 films, 5 nm Au/Pd was sputtered on the sample before SEM imaging.

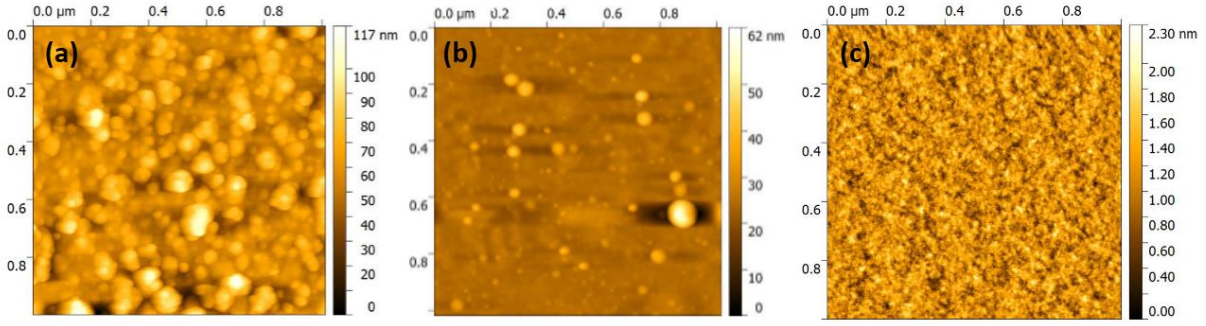

Figure 30: AFM images of PE-CVD TiO_2 films deposited on glass substrate with (a) only TTIP (b) TTIP and 10 sccm O_2 to the gas mixture and on (c) Si substrate. AFM scan area was 1 x 1 µm². Samples were made with V_{PP} = 5.8 kV and 30 plasma PR.

The large difference in the surface roughness of the TiO_2 films deposited on glass and Si substrates can be explained by the difference in the charge distributions on the surface in DBDs. Figure 32 shows the distribution of induced and deposited charges on metal electrode and dielectric surfaces in a planar DBD system [17]. Charges are deposited on the dielectric surface upon discharge ignition. It was shown that the charge distribution on the surface of dielectric is non-uniform, due to the filamentary discharges in DBDs [17,84]. The deposited charges on the dielectric surface lead to the induction of charges in the opposing electrode. The induced charges are uniformly distributed along the surface [17]. We hypothesize that the TiO_2 layers deposited on glass, where the glass serves as the dielectric of the DBD configuration (Figure 13) are influenced by the non-uniform surface charges and therefore rough surfaces with R_{MS} value between 4 and 11 nm were observed. On the other side, a smooth surface with R_{MS} value of 0.25 nm was observed when TiO_2 films were deposited on Si substrate. As it was described in section 3.1, a dielectric layer was placed between the electrode and Si substrate. Since the Si substrate is conductive, the induced charge is distributed uniformly along the surface of Si and therefore the TiO_2 layer on Si substrate is not affected by the non-uniform charge distribution on the dielectric surface.

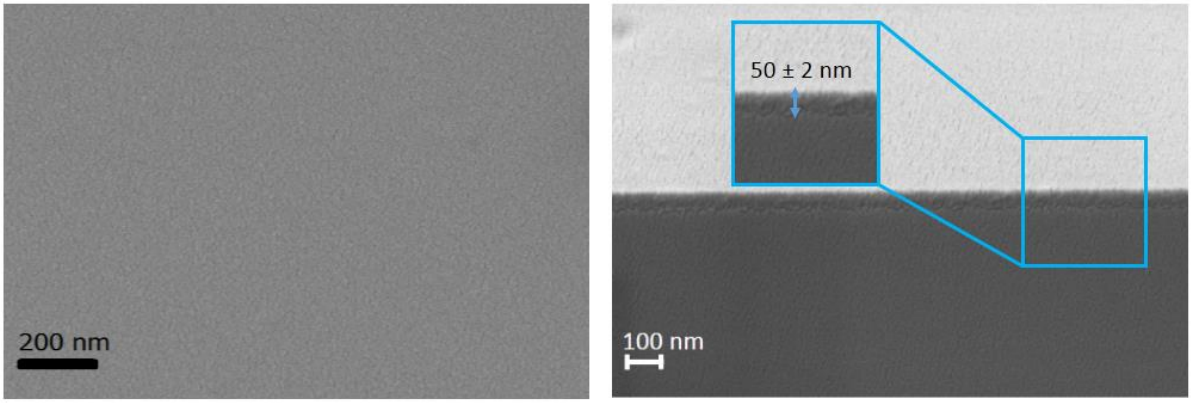

Figure 31: (a) SEM image of PE-CVD TiO_2 film deposited on Si substrate and (b) corresponding cross-sectional SEM image. Samples were made with V_{PP} = 5.8 kV, 30 plasma PR. Due to dielectric nature of TiO_2 films, 5 nm Au/Pd was sputtered on the sample before SEM imaging.

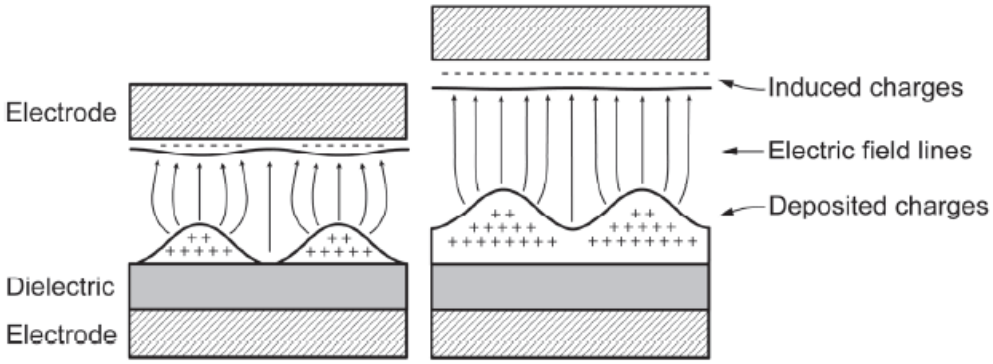

Figure 32: Schematic view of the distribution of deposited surface charges on dielectric substrate and the corresponding induced charges in opposing electrode in a planar DBD system. The induced charges are distributed more uniformly along the surface, leading to a more uniform electric field near the opposing electrode than near the dielectric layer. Taken from [17].

4.1.4 Printing resolution of the µPP in PE-CVD mode

The printing resolution of the µPP in PE-CVD mode was studied by XPS line-scan and is presented in this section. In order to determine the resolution in PE-CVD mode, TiO_2 was deposited on Si substrate in form of a line by surface activation with just one needle electrode. A distance of 270 µm between consecutive plasma dots was used (section 3.1). The line is expected to be the smallest TiO_2 feature that can be deposited. Atomic % of Ti, O, C and Si elements were measured by performing XPS line-scan perpendicular to the deposited TiO_2 line. Details of XPS line-scan can be found in section 3.3.2. Figure 33 shows the atomic % of the elements as a function of distance perpendicular to the deposition line. The TiO_2 line is characterized by the positions with highest concentration of Ti and O and decreased concentration of Si. In an ideal situation, Ti is not expected to be present out of the deposition area, but 9% of Ti was still detected in the vicinity areas. Probable explanations are: diffusion of active TTIP molecules which are generated in the plasma [38], contribution of moisture from the environment, condensation of TTIP molecules on the surface, etc. The resolution is described as

the distance between the points at full width half max (FWHM) of the corresponding Ti, O and Si signals in Figure 33, resulting in a resolution of approximately 1600 µm for a 20 plasma PR TiO_2 line.

It is expected that the printing resolution depends on the stability of the plasma. The TTIP precursor concentration is determined by the N_2 carrier flow through the TTIP bubbler and is expected to change by changing the N_2 flow. It is worth mentioning that the N_2 flow through TTIP bubbler for depositing the TiO_2 line (1 needle electrode) remained the same as the flow for depositing previous larger area samples (with multiple needle electrodes), due to limitations in the current setup. Therefore it is expected that the concentration of TTIP molecules in the discharge volume was too large for one single needle electrode. A too large precursor concentration manifests in an occasionally very bright and/or weak plasma and thereby influencing the line width of the deposition. It is also expected that the printing resolution depends on the number of plasma PRs and more experiments should be performed.

The information from XPS analysis is limited to the top 10 nm of the layer due to the limited escape depth of photoelectrons. The expected thickness of the TiO_2 line was 27 nm (20 * 1.33 nm/PR), however Si from substrate was detected in the deposited area, indicating that the layer thickness is less than 10 nm. Hence the growth rate is affected by the number of activated needle electrodes during discharge and the PE-CVD mode delivers no accurate thickness control for small area features.

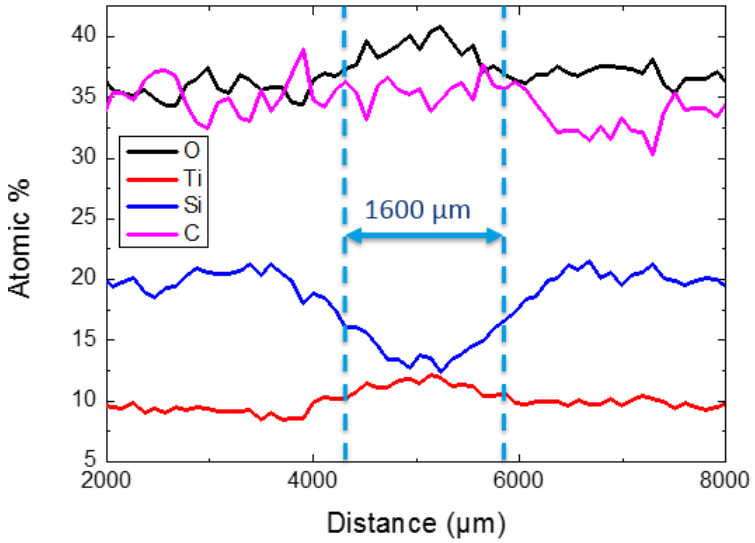

Figure 33: Atomic % of Ti, O, Si and C as function of distance, determined by XPS line-scan. The resolution is described as the distance between the points at FWHM of the corresponding Ti, O and Si signal, resulting in a resolution of approximately 1600 µm for a 20 plasma PR TiO_2 line.

4.1.5 Conclusions: TiO_2 deposited by PE-CVD mode

In this chapter it was shown that the µPP can be used as plasma source to deposit TiO_2 films at atmospheric pressure, by guiding vaporized TTIP precursor molecules to the discharge volume. The µPP was never used before to deposit metal oxides thin films and numerous hardware modifications were required, which are all described in Appendix B.

The films were deposited on dielectric (glass) and conductive (Si) substrates. The growth rate of TiO_2 films on glass substrate decreased from 2.3 to 2.0 nm/PR by the addition of O_2 to the gas mixture. A

lower growth rate (1.33 nm/PR) was observed on Si substrate, which can be explained by the difference in configuration (i.e. reduced average electric field strength).

A large difference in R_{MS} roughness was observed between the TiO_2 films deposited on glass and Si substrates. The surface of TiO_2 film on Si substrate was smooth with R_{MS} value of 0.25 nm and corresponding SEM images showed a smooth and uniform surface. The surface of TiO_2 films on glass substrate was rough and was composed of agglomerated particles and the size of the particles decreased by adding O_2 to the gas mixture. The same effect was visible in the corresponding AFM images, the R_{MS} roughness decreased from 11 to 4 nm by the addition of O_2. The large difference in roughness of films deposited on Si and glass substrates is explained by charge buildup on the dielectric substrate upon discharge. The RI index was only measured for TiO_2 film on Si substrate and was measured 1.81 on a 50 nm thick film. The chemical composition was determined by XPS. The carbon and nitrogen content in TiO_2 film on glass substrate decreased from 10.7 to 4.9% and 3.4 to 1.7%, respectively, by adding 10 sccm O_2 to the gas mixture. The amount of carbon and nitrogen in films deposited on Si substrate was measured 7.5 and 0.5%, respectively. Some recent works reported significantly lower amounts of carbon in TiO_2 films. Therefore the material quality of the TiO_2 films deposited in PE-CVD mode is not satisfying yet. Hence the question arises if the temporal/spatial separation of precursor and oxidant exposures (i.e. ALD-mode) could lead to the improvement of the material quality.

The patterning resolution of the µPP in PE-CVD mode was approximately 1600 µm for a 20 plasma PR TiO_2 line. It is worth mentioning that the growth rate was affected by the number of activated needle electrodes, hence the PE-CVD mode provides no accurate thickness control for small area features.

4.2 Plasma-assisted ALD of TiO_2 thin films.

Since the deposition of TiO_2 films in PE-CVD mode showed relatively large amount of carbon in the film (7.5% in case of Si substrate) and a relatively low RI (Table 10), in this section we explore the spatial/temporal separation of the substrate exposure to the precursor and oxidant. The µPP was upgraded to a so-defined µ-plasma assisted ALD setup by integration of a precursor dosing compartment at the print-stage. The design and modifications of the print-stage are described extensively in section 3.2.2.

The saturation experiments in order to determine the ALD process development are described in section 4.2.1. The chemical composition and impurity content of TiO_2 ALD films were studied by XPS and RBS/ERD and can be found in section 4.2.2. Section 4.2.3 describes the morphology and surface roughness. The patterning resolution of the µPP, when operated in ALD mode, is investigated in section 4.2.4. The chapter is completed with a conclusion and comparison between both depositions modes (i.e. PE-CVD and plasma-assisted ALD).

4.2.1 ALD process development

The basic principles and properties of ALD can be found in Appendix A. ALD is characterized by self-limiting surface reactions, ideally resulting in a constant growth per cycle (GPC) within a specific process window. The required precursor and plasma exposure times and purge times to achieve self-limiting surface reactions depend on the substrate, precursor and oxidant. In order to establish the ALD process of TiO_2 on µPP tool, a set of saturation experiments were therefore performed.

In µPP ALD setup, the precursor exposure time can be changed between 315 and 1900 ms by varying the motion speed of the printing head (Table 2). The deposition area was purged during the head translation and the purging time for every TTIP exposure (i.e. motion speed) is reported in Table 2. However extra purge time can be added, as already discussed in section 3.2.2. Thickness of the deposited films were measured by ex-situ SE after 100 ALD cycles and the GPC was calculated. Saturation curves were obtained by changing the precursor exposure and purge times (Figure 34a). The GPC is not saturating by increasing the TTIP exposure time from 0 to 1900 ms, when no extra purge time was used in between the TTIP and O_2 plasma exposures. Insufficient purge in ALD process can lead to incomplete removal of the unreacted species from the chamber (in the case of µPP, deposition area). CVD reactions can therefore occur between unreacted precursor molecules and the gas molecules from the next ALD half cycle, i.e. O-radicals, leading to higher GPC than a pure ALD process [85]. This effect was more visible when longer precursor exposure times (TTIP exposure time of 1900 ms) were used, because the required purge time for longer precursor exposure times may be much higher. The GPC decreased with increasing purge time and saturated at 0.145 nm/cycle with a TTIP exposure time between 475 and 950 ms, when 30s of extra purge time was used (Figure 34a). However, the GPC increased slightly (0.17 nm/cycle) when the TTIP exposure time was doubled (950-1900 ms), as a consequence of insufficient purge for that long TTIP exposure times.

The influence of purge time on the GPC was further investigated, by depositing a set samples with fixed precursor exposure time (475 ms) and increasing extra purge time from 0 to 30s. Figure 34b shows that the GPC remains constant at 0.145 nm/cycle after 10s of extra purge time, when 475 ms of TTIP exposure time per cycle was used. Most low temperature thermal ALD processes require longer purge

times to achieve self-limiting surface reactions, however the required purge time in the µPP ALD-setup is significantly reduced by using O_2-plasma as oxidant and thereby highlighting the advantage of plasma [37].

Hence the GPC at saturation is 0.145 nm/cycle, however a large variety of GPCs are reported in other ALD processes of TiO_2 with TTIP as precursor, varying between 0.05 and 0.19 nm/cycle [37,40,41,35,33]. An overview of other reported ALD processes of TiO_2 and the corresponding properties can be found in Appendix F. In a recent study by Theirich et al [40], TiO_2 ALD films were deposited at atmospheric pressure and room temperature with TTIP as precursor and O_2 DBD-plasma as oxidant. It was shown that the GPC increased with increasing TTIP exposure, however the purge time was 15s in all experiments and probably not sufficient enough. A GPC of 0.16 nm/cycle was reported, consisting of 0.11 nm/cycle ALD component and an additional parasitic CVD component of 0.05 nm/cycle due to reactions with residual water in the system. While in [35], low pressure radical enhanced ALD of TiO_2 with TTIP as precursor was performed, a GPC of 0.19 nm/cycle was reported. Therefore the GPC achieved with the µPP ALD-setup corresponds with values reported in the literature.

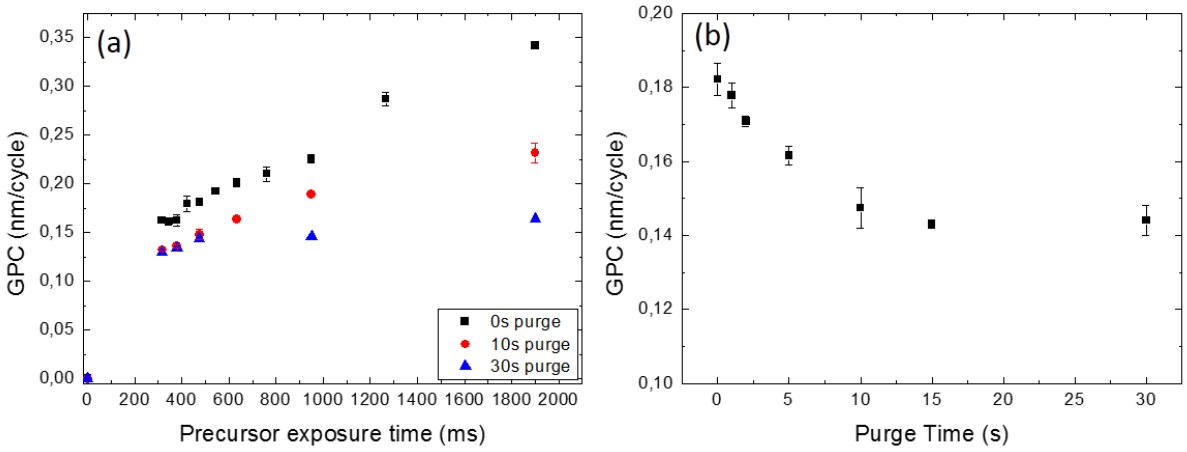

Figure 34: (a) GPC (nm/cycle) as function of precursor exposure time (ms) for three different extra purge times: black: 0s, red: 10s and blue: 30s. Plasma exposure time per ALD-cycle was 400 µs and V_{PP} = 5.8 kV. (b) GPC (nm/cycle) as function of purge time (s). Precursor exposure time per ALD-cycle was 475 ms, plasma exposure time 400 µs and V_{PP} = 5.8 kV was used during all the experiments. Note: Y-scale starts at 0.10 nm/cycle. The GPC was calculated after 100 ALD-cycles.

The required plasma exposure time to achieve self-limiting ALD reactions was determined, by investigating the influence of the plasma exposure time on the GPC. As it was described in section 3.2.2, the plasma exposure time can be increased by discrete steps of 400 µs, by increasing the number of plasma PR per ALD-cycle. A series samples was deposited with increasing number of plasma PR per cycle from 1 to 10, all with 100 ALD-cycles, 475 ms precursor exposure and 0s extra purge time per ALD-cycle. The GPC as function of plasma PR and plasma exposure time per ALD-cycle is presented in Figure 35a. The GPC decreased from 0.18 nm/cycle when only one plasma PR/cycle was applied to 0.15 nm/cycle when more than three plasma PR were applied in each ALD-cycle. The decrease in GPC is explained by the more efficient abstraction of the absorbed TTIP molecule hydrocarbon groups (ligands) with increasing O_2 plasma exposure time. However chemical analyses is required, which is addressed in section 4.2.2.

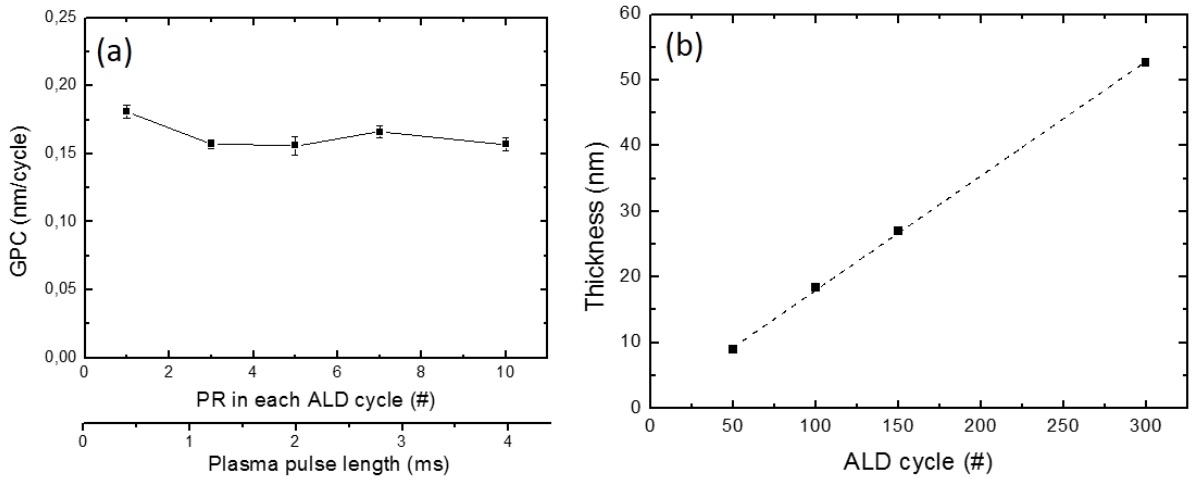

Figure 35: (a) GPC (nm/cycle) as function of plasma PR, i.e. plasma exposure time (ms) per ALD-cycle. The GPC was calculated after 100 ALD-cycles. Precursor exposure time per ALD-cycle was 475 ms, no extra purge time and V_{PP} = 5.8 kV. (b) Thickness (nm) as function of number of ALD cycles. Precursor exposure time per ALD-cycle was 475 ms, plasma exposure time 400 µs, no extra purge time and V_{PP} = 5.8 kV was used during all the experiments.

The thickness of TiO_2 films as a function of number of ALD cycles is shown in Figure 35b. The TiO_2 layers were deposited by 475 ms of TTIP exposure, one plasma PR (400 µs) and 0s of extra purge time in every cycle. It shows that the growth was linear between 50 and 300 ALD cycles. It is worth mentioning that the TiO_2 layers in Figure 35b were not deposited under saturation conditions and therefore an additional CVD component is present.

The ALD process development was determined in this section. It was shown that saturation of the growth was achieved at 0.145 nm/cycle when 10s of extra purge time, 475 ms TTIP exposure time and one plasma PR per ALD cycle were applied. The influence of plasma exposure time on the GPC was not found to be a relevant parameter, while the precursor exposure and purge times are essential to be controlled to achieve saturated processes at the surface.

4.2.2 Chemical and optical properties

The chemical composition, O/Ti ratio, mass density and deposition rate of the TiO_2 ALD films was investigated by means of XPS and RBS/ERD measurements. XPS measurements were performed after sputtering with Ar^+ ions. The influence of plasma exposure time, i.e. plasma PR per ALD-cycle on the impurity content was determined by XPS measurements. The samples were deposited all with 100 ALD-cycles with 475 ms of precursor exposure, 0s extra purge time and increasing number of plasma RP per ALD-cycle from one to ten. Table 6 shows that the amount of carbon and nitrogen in the films decreases with increasing plasma exposure time. The amount of carbon in TiO_2 film when only one plasma PR was applied was 5.1% and decreased to less than 1% when more than 7 plasma PR/ALD-cycle were applied. An increase in O_2 plasma exposure leads to a more quantitative removal of the hydrocarbon ligands of the absorbed TTIP molecules. The amount of nitrogen in the TiO_2 films decreased from 3.0 to 1.8% by increasing the plasma exposure time. The decrease in amount of carbon in TiO_2 films with increasing O_2 plasma exposure time was also reported in a recent study by Aghaee et al [37], where TiO_2 films were deposited with a low pressure plasma-assisted ALD setup with TTIP as precursor and O_2 plasma as oxidant. They observed that the amount of carbon in the film decreased from 5.0 to 0.5% by increasing O_2 plasma exposure time from 500 ms to 5s. Similar carbon and nitrogen

concentrations were reported in [86], where TiO_2 films were deposited by a ALD process with a heteroleptic alkylamido titanium precursor and O_2 plasma as oxidant. However the precursor was different and therefore difficult to compare with this work (Table 11, Appendix F).

Table 6: Elemental carbon and nitrogen content of TiO_2 ALD films deposited with increasing number of plasma PR per cycle from one to ten, according to XPS. Measurements were performed after sputtering with Ar^+ ions. All samples deposited by 100 ALD-cycles. The precursor exposure time per cycle was 475 ms, extra purge time was 0s and V_{PP} = 5.8 kV was used during all the experiments. .

PR in each ALD cycle	Plasma pulse length (ms)	Bulk analysis (%) ± 1.0	
		C	N
1	0.4	5.1	3.0
3	1.2	2.7	2.5
5	2	2.0	2.4
7	2.8	0.9	1.8
10	4	1.1	1.9

Table 7: Chemical composition, mass density and deposition rate of TiO_2 ALD films determined by XPS and RBS/ERD measurements. All samples deposited by at least 500 ALD-cycles with 475 ms of precursor exposure time per cycle. The amount of purge time and plasma PR per ALD-cycle is shown in the table. XPS measurements were performed after sputtering with Ar^+ ions. Note: samples were deposited after refilling TTIP bubbler (50g), which was double the amount as for the previous samples.

PR in each ALD cycle	Purge time (s)	Total plasma pulse length (ms)	Atomic % by XPS (± 1%)		Atomic % by RBS/ERD(*)			Mass density (g/cm^3)	[O]/[Ti]	Ti at./nm^2.cycle
			C	N	C	N	H			
1	10	0.4	4.2	5.4	<4.5	3.5	12.3	1.70	2.05	2.2
5	0	2	5.1	4.2	<4.5	3.0	13.0	1.85	2.08	2.3
5	10	2	4.2	5.9	<4.5	7.8	11.2	1.8	2.12	2.2
10	10	4	<1	4.9	<4.5	2.9	6.3	2.04	2.20	2.4

(*) Accuracy RBS measurement: H: 7%; Ti: 2%; O: 4%; N: 2%; Detection limit of RBS: N: 2%; C: 4%.

Table 7 presents the chemical composition, mass density (g/cm^3), O/Ti ratio and deposition rate (at/nm^2.cycle) according to RBS/ERD measurements for various samples. XPS measurements were also performed on the same samples and the C and N value from XPS after Ar^+ sputtering is reported in the same table. All samples were deposited with at least 500 ALD-cycles. The O/Ti ratio increased from 2.05 to 2.20 by increasing plasma exposure time and no significant influence of purge time on the O/Ti ratio was observed. The amount of carbon was below the detection limit of RBS (<4.5%) while it was between less than 1 and 5.1% according to XPS measurements. The amount of nitrogen decreased with increasing plasma exposure time from 3.5 to 2.9%, according to RBS measurements. The same effect was also observed in the XPS measurements for previous deposited samples (Table 6). The

amount of nitrogen in the TiO_2 film deposited with 10s of extra purge time and 5 plasma PR per ALD-cycle was measured 7.8%, however the accuracy of that measurement is questionable. It is worth mentioning that the values between the two tables (Table 6 and 7) are different, which can be explained by several reasons. First of all, the gap distance between the Si substrate and the plasma print head could have been slightly larger, resulting in a lower plasma energy density. Secondly, small variations in gas flow/speed (O_2 and TTIP) and pump speed were possible. Another possibility is that the needle electrodes were affected by the prolonged O_2-plasma ignition.

The hydrogen content was determined by means of ERD (section 3.3.6) and decreased from 12.3 to 6.3% by increasing plasma exposure time from 1 to 10 PR, respectively. This is explained by the removal of the hydrocarbon ligands of the TTIP molecule by active O-species. The mass density and deposition rate was calculated from the areal density. The number of deposited Ti atoms per cycle (i.e. deposition rate) increased from 2.2 to 2.4 at/nm².cycle with increasing plasma exposure time. The number of Ti atoms per nm² can also be calculated theoretically[c], using the mass density obtained from the RBS measurements and varied between 2.6 and 2.9 at/nm². Figure 36 shows the change in mass density and RI as a function of plasma PR in each ALD-cycle. The mass density increased from 1.70 to 2.04 g/cm³ and the RI from 1.86 to 1.97 by increasing the plasma exposure time from 1 to 10 PR per ALD cycle. The RI of the TiO_2 films with one plasma PR per ALD-cycle was measured 1.86, and no significant influence of precursor exposure or purge time was observed. The RI is rather low in comparison with other values reported in the literature, varying between 2.1 and 2.4 [42,37,35]. However the reported systems are low-pressure ALD systems with significant higher substrate temperatures. There were no report on the RI of TiO_2 ALD films deposited at atmospheric pressure.

In [87] TiO_2 ALD films were deposited by a low pressure ALD setup at 200°C with TTIP as titanium precursor and O_2 plasma as oxidant, they reported an O/Ti ratio of 2.3. In a recent study by Ratzsch et al [88], TiO_2 ALD films were deposited with a low pressure plasma-assisted ALD setup at substrate temperatures between 70 and 200°C with TTIP as precursor and O_2 plasma as oxidant. They reported an O/Ti ratio of 2.0 and a mass density of 2.61 g/cm³. In another study by Potts et al [33], TiO_2 ALD films were deposited at low pressure and room temperature with TTIP as titanium precursor and O_2 plasma as oxidant. They reported a GPC of approximately 0.06 nm/cycle, an O/Ti ratio of 2.2, mass density of 2.7 g/cm³, carbon content of 4.2%, hydrogen content of 16.9% and a deposition rate of 0.9 at/nm².cycle. Therefore the O/Ti ratio of the deposited TiO_2 thin films with the µPP ALD setup correspond with values reported in the literature. The observed mass density in this work is lower than the values reported by Potts and Ratzsch et al, which was already expected from the relatively low RI. More critical is the significant higher number of atoms deposited per ALD-cycle, 2.2-2.4 at/nm².cycle with the µPP ALD setup and only 0.9 at/nm².cycle was reported by Potts et al. Which could possibly suggest that the µPP ALD process is not completely pure ALD but more an ALD-like process.

[c] the atomic areal density of one TiO_2 monolayer can be calculated according to Eq.[89]: $atomic\ areal\ density = \left(\frac{1}{3}\frac{\rho * N}{\mu}\right)^{2/3}$ where ρ is the TiO_2 mass density (Table 7), N Avogadro's number and μ the molecular mass of TiO_2 (79.9 g/mol).

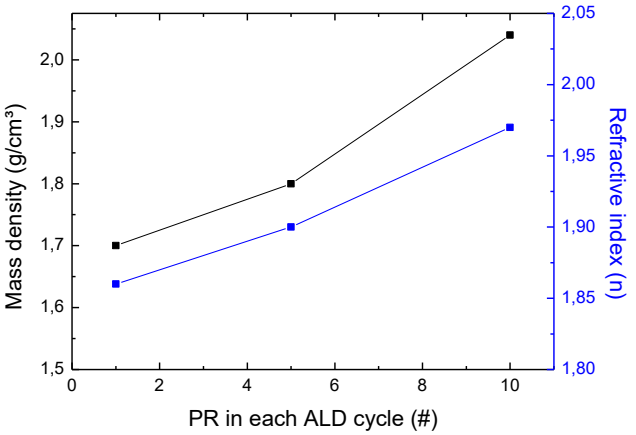

Figure 36: Mass density (g/cm³) and RI (at λ = 632.8 nm) of TiO_2 films measured by RBS and SE, respectively, as a function of PR in each ALD-cycle. Precursor exposure time per ALD-cycle was 475 ms and 10s of extra purge time was used.

4.2.3 Morphology and surface roughness

The morphology and surface roughness of the TiO_2 ALD films were determined with SEM and AFM. Figure 37 shows an AFM image (a) and a cross-sectional SEM image (b) of an ALD TiO_2 film. The AFM scan area is 1x1 µm² and the scale in the SEM image is 100 nm. The TiO_2 sample was deposited at saturation conditions. The film was amorphous (as confirmed by Raman spectroscopy) and the R_{MS} roughness was measured 0.25 nm. The cross-sectional SEM image showed a uniform and smooth layer. Amorphous TiO_2 films were also observed in other low temperature (i.e. lower than 250 °C) ALD processes with TTIP as precursor and O_2 plasma as oxidant (Table 11) [37,35,34]. A similar surface roughness value was reported by Theirich et al [40], where TiO_2 ALD films were deposited at atmospheric pressure with TTIP as precursor and O_2 plasma as oxidant.

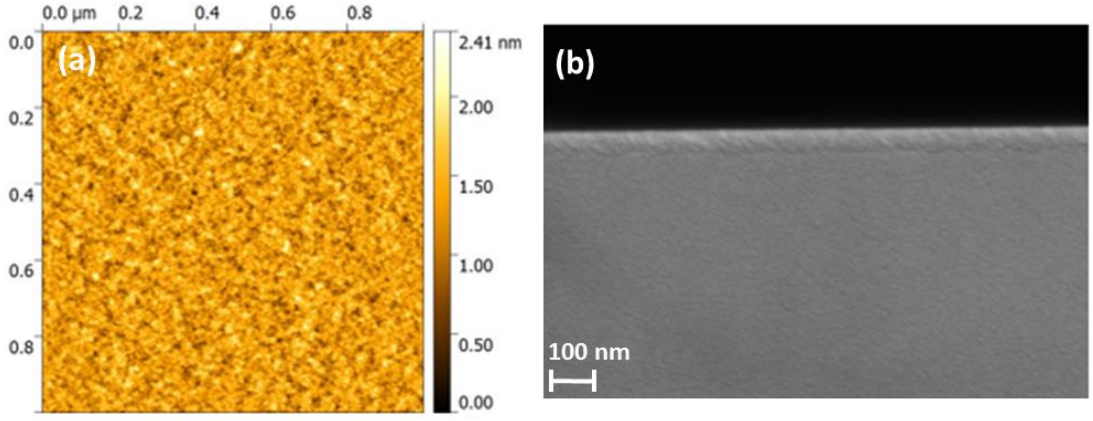

Figure 37: (a) AFM and (b) cross-sectional SEM image of TiO_2 thin film deposited in plasma-assisted ALD mode. AFM scan area is 1x1 µm² and the scale in the SEM image is 100 nm. The film was deposited at saturation conditions and the film thickness is approximately 50 nm.

4.2.4 Resolution of the µPP in plasma-assisted ALD mode

The resolution of the µPP in plasma-assisted ALD mode is described in this section. The resolution is determined by the same method as it already has been described in section 4.1.4 for PE-CVD samples. A TiO_2 line was deposited by activation of two consecutive needle electrodes. The line was deposited by 50 ALD-cycles at saturation conditions (i.e. 475 ms of precursor exposure, 30s extra purge time and 400 µs plasma exposure time per ALD-cycle). As for the PE-CVD line sample, a distance of 270 µm between consecutive plasma dots was used. The result of XPS line-scan is presented in Figure 38, showing that the patterning resolution after 50 ALD-cycles is approximately 1400 µm. It is worth mentioning that the resolution in PE-CVD mode was determined by activation of only one needle electrode, while two consecutive needle electrodes were activated for the ALD line sample. Due to limitations in system's design, TiO_2 line could not be deposited in plasma-assisted ALD mode with only one needle electrode.

The profile (Figure 38) shows titanium in the surrounding area, most likely due to accumulated TTIP precursor molecules on the surface or due to diffusion of active O_2 plasma species. A large difference is observed in the carbon signal between the deposited line and surrounding area, while no difference in the signal was observed in PE-CVD mode (Figure 33).

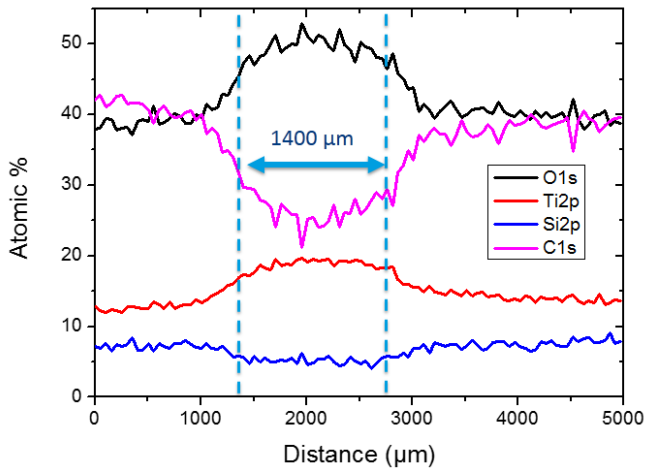

Figure 38: Atomic % of Ti, O, Si and C as function of distance, determined by XPS line-scan. The resolution is described as the distance between the points at FWHM of the corresponding Ti, O, Si and C signal, resulting in a resolution of approximately 1400 µm for a 50 ALD-cycle TiO_2 line. Note that the TiO_2 ALD line is two pixels wide, i.e. two consecutive needle electrodes were activated for the deposition.

4.2.5 Conclusion and comparison between plasma-assisted ALD and PE-CVD mode

In this chapter it was shown that the µPP can be upgraded to a µ-Plasma assisted ALD setup, which makes possible to deposit patterned TiO_2 films with sub-nanometer thickness control. In order to enable ALD with the µPP, a precursor dosing head was integrated in the system. The required hardware modifications are extensively described in section 3.2.2. Saturation experiments were performed to

determine the required precursor exposure, plasma exposure and purge time to achieve self-limiting surface reactions (ALD process development). The GPC remained constant at 0.145 nm/cycle after 10s of extra purge time, when 475 ms of precursor exposure time and one plasma PR per ALD-cycle were used. The effect of plasma exposure time on the growth was not as important as the TTIP exposure and purge time.

The SEM and AFM images showed a uniform and smooth surface with a R_{MS} roughness of 0.25 nm. The RI was measured 1.97 on a TiO_2 film deposited at saturation conditions and 10 plasma PR per ALD-cycle. RBS measurements showed a mass density of 1.70-2.04 g/cm³ and the O/Ti ratio was variable between 2.05 and 2.20. The TiO_2 films contained carbon, nitrogen and hydrogen as impurities, according to XPS and RBS/ERD measurements. An overview of the material properties can be found in Table 8 and Appendix F.

The amount of carbon, nitrogen and hydrogen in the TiO_2 films decreased to less than 1.0, 1.8 and 6.3%, respectively, by increasing the number of O_2 plasma PR per ALD-cycle, due to a more effective combustion of the hydrocarbon ligands of the absorbed TTIP molecule. Hence the amount of impurities in the TiO_2 film decreased with increasing plasma exposure time, resulting in the formation of a more pure and denser TiO_2 film. As confirmed by the increasing mass density (1.70 to 2.04 g/cm³), number of deposited Ti atoms per cycle (2.2 - 2.4 at/nm².cycle) and RI (1.86 – 1.97) with increasing plasma exposure time. The obtained properties correspond well with other reported ALD processes, a comparison can be found in Table 11 (Appendix F). The pattering resolution of the µPP in ALD mode was found to be approximately 1400 µm for a TiO_2 line deposited by activation of two consecutive needle electrodes.

Table 8: Overview of the properties of TiO_2 films deposited in PE-CVD and plasma-assisted ALD mode. The reported PE-CVD film properties are for TiO_2 films deposited on Si substrates.

	PE-CVD mode	Plasma-assisted ALD mode
Growth rate	**1.33 nm/PR**	**0.145 nm/cycle**
R_{MS} roughness	**0.25 nm**	**0.25 nm**
Refractive index (@ 632.8 nm)	**1.81**	**1.97**
O/Ti Ratio (*)	**2.15**	**2.05-2.20**
Carbon content	**7.5 ± 0.5 %**	**<1%**
Nitrogen content	**<1%**	**1.8 ± 0.5%**
Accurate thickness control (**)	**No accurate thickness control for small features**	**Yes, accurate thickness control for small features**
Resolution	**1600 µm (20 PR); 1 needle electrode**	**1400 µm (50 cycles); 2 needle electrodes**

(*) O/Ti ratio in PE-CVD mode was determined by XPS measurements without sputtering. The ratio in ALD mode was determined by RBS/ERD measurements.
(**) Influence of number of activated needle electrodes on the growth rate.

Table 8 presents an overview of the properties of TiO_2 films deposited in PE-CVD and ALD mode. First of all, the growth rate of TiO_2 on Si substrate was 1.33 nm/PR in PE-CVD mode, while 0.145 nm/cycle at saturation conditions in ALD mode. The surface of TiO_2 films deposited in PE-CVD and ALD modes were smooth, a R_{MS} roughness of 0.25 nm was measured in both situations. The RI increased from 1.81 in PE-CVD to 1.97 in ALD mode (with 10 plasma PR/ALD-cycle). The higher RI indicates an increased material mass density of the TiO_2 films deposited in ALD mode. The O/Ti ratio was 2.15 in PE-CVD mode, determined by XPS without sputtering. The O/Ti ratio in ALD mode was determined by RBS/ERD and was measured 2.05-2.20. However the ratios are determined by two different methods and

therefore difficult to compare. The amount of carbon in the films decreased from 7.5% in PE-CVD mode to less than 1% in ALD mode (with 10 plasma PR/ALD-cycle). Plasma-assisted ALD mode enables the possibility to increase the plasma exposure time independently to the precursor exposure time, which was obviously not possible in PE-CVD mode, which explains the lower amount of carbon in the ALD TiO_2 film. In contrary, the amount of nitrogen increased from 0.5% in PE-CVD mode to 1.8% in ALD mode. It is expected that the production rate of NO_x related plasma species is higher in an O_2/N_2 gas mixture than in an O_2/N_2/TTIP gas mixture, which explains the larger amount of nitrogen in films deposited in ALD mode.

One of the research questions in this Master Thesis, is whether the modification of the µPP from a PE-CVD system in a plasma-assisted ALD system results in an enhancement of the patterning resolution. The resolution of the µPP in PE-CVD mode was approximately 1600 µm for a 20 plasma PR TiO_2 line, deposited by activation of only one needle electrode. While the resolution in ALD mode was approximately 1400 µm for a TiO_2 line deposited with 50 ALD-cycles at saturation conditions and activation of two consecutive needle electrodes. Due to limitations in system's design, no TiO_2 line could be deposited in ALD mode by activation of only one needle electrode. The growth rate in PE-CVD mode was influenced by the number of activated needle electrodes. A significantly smaller growth rate was observed when depositing TiO_2 films in form of a line by activation of only one needle electrode than when depositing larger area features by activation of multiple needles. It is worth mentioning that the growth rate in plasma-assisted ALD mode was constant and not affected by the number of activated needle electrodes. Hence one of the advantages of the plasma-assisted ALD mode is an accurate thickness control for small area features.

It can be concluded that the modification of the µPP from a PE-CVD in a plasma-assisted ALD setup results in improved material properties, an enhancement of the patterning resolution and a more accurate thickness control for small area features. The modification makes it possible to deposit almost carbon-free TiO_2 thin films with sub-nanometer thickness control. Besides all the advantages, the ALD process is significantly slower than the PE-CVD process. First of all due to the lower growth rate and secondly because of the required purge times to obtain self-limiting surface reactions. However the integration of a special purge module/zone could decrease the required purge time significantly, which is discussed in the outlook.

4.3 Nitratine crystal formation

In the analyses of TiO_2 films deposited in PE-CVD mode on glass substrate, some remarkable micro-size crystallized particles were observed as shown in Figure 39, in which a large scale (a) SEM image is presented with two close-ups of crystallized particles (b, c). Energy-dispersive X-Ray spectroscopy (EDX) and Raman spectroscopy have been performed in order to determine the composition of the crystals. The EDX results are presented in Figure 40, measured on a crystallized particle (a) and (b) on the surrounding area.

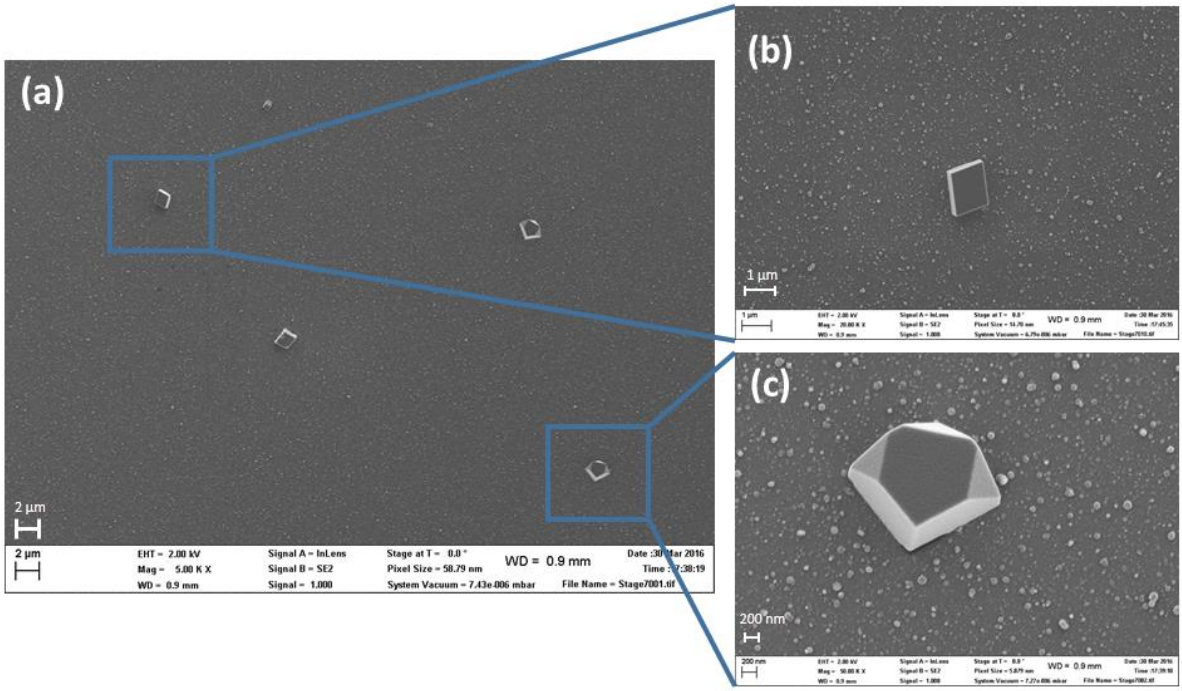

Figure 39: SEM image of PE-CVD TiO_2 thin film on glass substrate (30 plasma PR, 25 sccm TTIP, 10 sccm O_2, V_{PP} = 5.8 kV). Micro-crystallized particles were detected. (b, c) are two close-ups of crystallized particles.

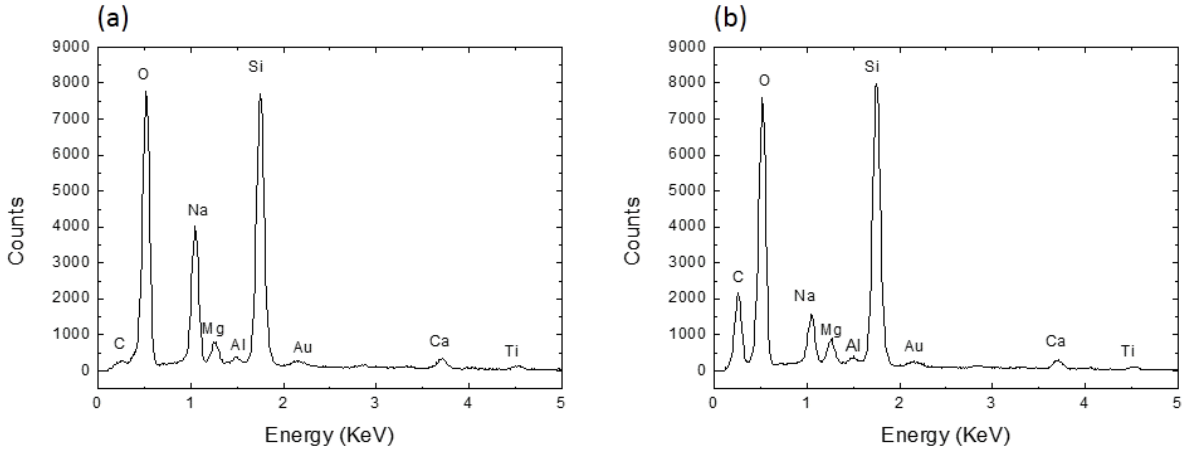

Figure 40: EDX spectra measured on (a) crystalized particle and (b) surrounding area. A large intensity difference is observed in the sodium (Na) and carbon (C) peaks.

The detected elements are all present in soda-lime-silicate glass substrates (Table 9) [90]. EDX is characterized by a large penetration depth, in the order of micro-meters, depending on the material density and the acceleration voltage of the e-beam [91]. A large intensity difference is observed in the carbon and sodium peaks. The carbon intensity decreased and the sodium intensity increased on a crystallized particle. The other components have a comparable intensity.

The Raman spectrum, determined on a crystallized particle is presented in Figure 41. The observed peaks at 186, 724, 1067, 1386 and 1670 cm^{-1} correspond all with Nitratine ($NaNO_3$) [92,93,94]. The structural formula of Nitratine is presented in Figure 42. The particles were also detected on the surface of O_2-plasma treated substrates, hence without TTIP in the gas mixture. However, the particles were not detected on an untreated substrate. Therefore it is most likely that the Nitratine crystals are formed due to a combinatorial reaction of the sodium containing silicate glass substrate with NO_X related plasma species. However the formation of Nitratine crystals in a plasma environment has never been reported so far.

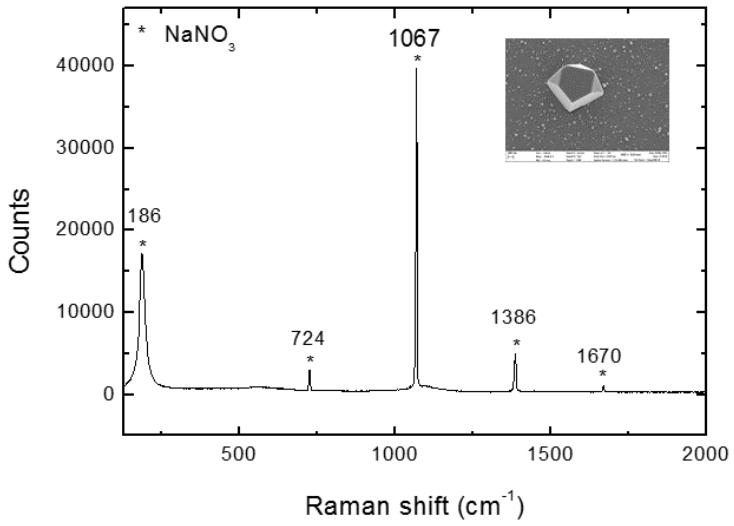

Figure 41: Raman shift measured on a crystallized particle. The detected peaks all correspond with Nitratine ($NaNO_3$) [92,93,94].

Table 9: Composition of soda-lime-silicate glass substrates.[95,96]

	%
SiO_2	70-74
Na_2O	13-18
CaO	8-10
MgO	3-4
Al_2O_3	0.15
Fe_2O_3	0.1
K_2O	0.03
TiO_2	0.02

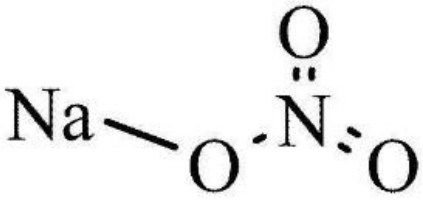

Figure 42: Chemical structural formula of Nitratine ($NaNO_3$)

The effect of sodium in the substrate was excluded by depositing a 100 nm thick Al_2O_3 film by ALD on the silicate glass substrate [97]. No crystallized particles were observed after O_2-µPlasma treating the Al_2O_3 coated substrate. Therefore the silicate glass substrate can be attributed as the sodium source.

In order to gain more insight in the growth mechanism, substrates were O_2-µPlasma treated (10 sccm O_2, V_{PP} = 5.8 kV) with increasing number of plasma PR (1-30). The statistical analyses of the corresponding SEM images is presented in Figure 43, with (a) the average number of particles detected in an area of 3200 µm², (b) the average size of the particles and (c) the surface coverage of the particles as function of plasma PR. Initially, when only one plasma PR was used, a small amount of particles was detected but the average particle size was rather large (0.36 ± 0.17 µm²). The amount of detected particles increased and the average particle size decreased by increasing the number of plasma PR. The surface coverage increased linearly with number of plasma PR. Therefore it is expected that rather large crystals were formed which are fragmented into smaller crystals in the following plasma PRs.

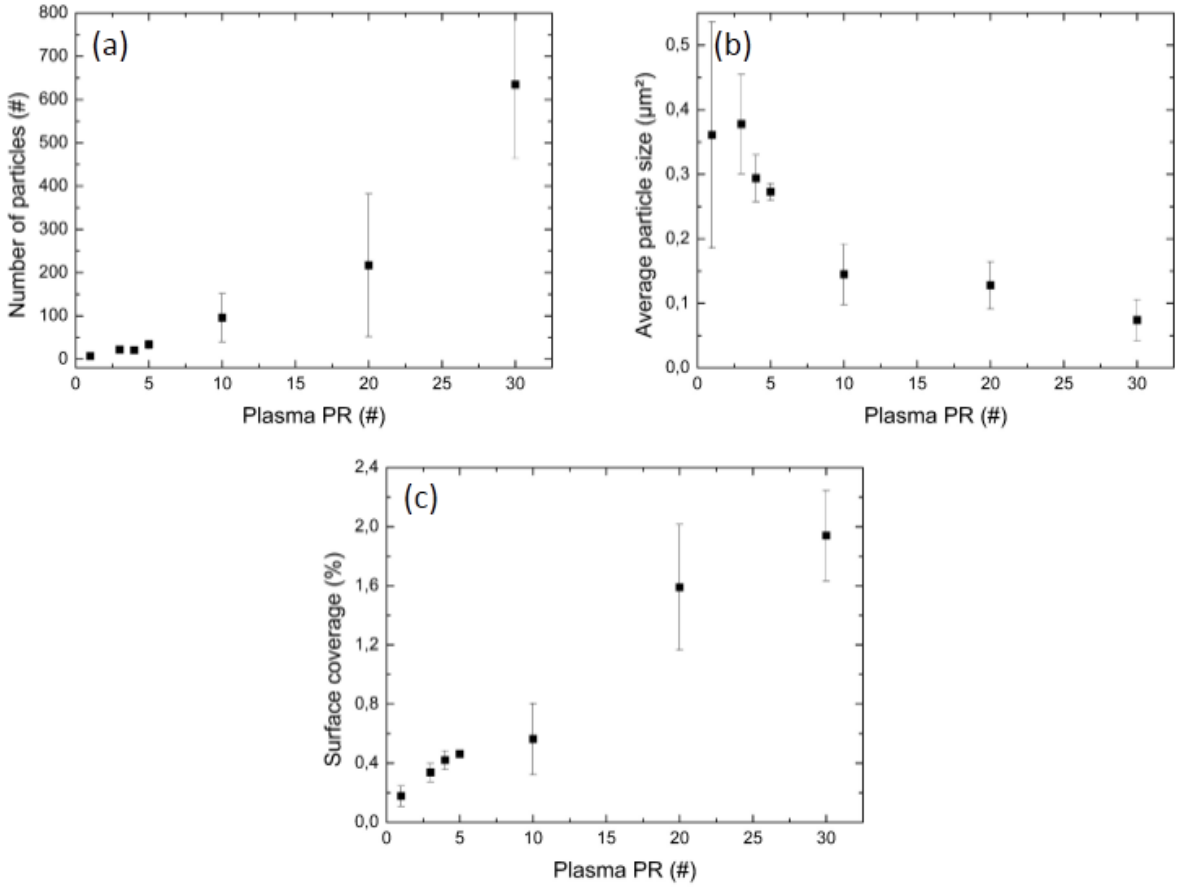

Figure 43: (a) Average number of detected particles, (b) average size of the particles and (c) surface coverage of the crystallized particles as a function of O_2 plasma PR (10 sccm O_2, V_{PP} = 5.8 kV). The analyzed area is 3200 µm². The measurements were averaged over 4 different SEM images and the corresponding standard deviation was used for the error bars.

As already mentioned, nothing has been reported about Nitratine crystal formation in plasma environment so far, hence no growth mechanism is reported. Therefore in the following paragraph a hypothesis is presented to explain the crystal formation.

Growth mechanism (hypothesis):

We hypothesize that the crystals are formed due to a combinatorial reaction of the sodium containing silicate glass substrate with NO_x related plasma species. The substrate is exposed to a large electric field, in the order of 10^7 V/m, upon discharge ignition. The appliance of a strong electric field near a glass substrate could possibly initiate a diffusion of sodium ions to the surface, as has been reported in [90]. They reported the diffusion of sodium and potassium ions in Borosilicate glass tubes with an applied electric field between 10^4 and 10^5 V/m.

The µPP is operated with an AC supply voltage, hence the sign of the electric field changes every half-cycle. However the electric field strength near the substrate's surface can be significantly larger than the average electric field strength, due to the filamentary discharges [98], which could explain the diffusion of sodium ions to the surface. However some effort should be made to determine the electric field strength in the µPP during discharge. Hence it is assumed that sodium ions diffuse towards the surface upon discharge ignition. The silicate glass substrates also contain calcium (± 9%), however calcium ions (Ca^{2+}) are less mobile than sodium ions (Na^+). In order to prove the participation of sodium compounds of the substrate in the reaction mechanism, depth profiling measurements have been performed with XPS on an O_2-µPlasma treated substrate (30 plasma PR, 10 sccm O_2). The result is presented in Figure 44a, in which the sodium concentration is shown as a function of etch time. The etch rate is 0.2 nm/s, therefore the figure shows an atomic concentration as function of depth. The amount of sodium increased from 1 to 5%, with increasing depth, until saturation at 5% after 250s (50 nm depth). Indicating that the sodium species in the top 50 nm layer were used in the Nitratine crystal formation. A schematic view of the sodium concentration in the substrate, after plasma treatment is presented in Figure 44b. However one of the remaining questions is in what form sodium exists in the silicate glass substrates, which can either be Na cations or Na_2O. Na cations can diffuse to the surface by appliance of a sufficient strong electric field. However, a large amount of energy is required to dissociate a Na_2O molecule. Knowledge of the electric field strength in the µPP during discharge is required to determine the probability to dissociate a Na_2O molecule with the electric field in the µPP.

Apart from sodium ions, also nitrogen oxide related species (NO_x) are required for the crystal formation. Nonetheless, the production of NO_x related species in discharges with an air-like gas mixture have been reported several times [99,100]. In [99] the detection of NO_x related species (i.e. NO, NO_2, N_2O, HNO_2) was reported, detected by gas-phase FTIR studies in an roll-to-roll DBD setup with an air-like gas mixture. It was shown that the production rate of NO_x related species increased with increasing O_2-flow. However NO_3 was not detected. While in [100] FTIR measurements are reported, performed on the gas mixture produced by an atmospheric pressure argon plasma jet with N_2/O_2 mixture as shielding gas, they reported long living nitrogen species, such as NO_2, NO, N_2O, N_2O_5 and HNO_3. The time evolution of the density of NO_x species in a streamer of an air DBD has also been modelled [101]. They report the production of NO, N_2O_5, N_2O, NO_2 and NO_3.

Therefore the Nitratine crystals are most likely formed due to a combinatorial reaction between NO_x related species, produced in the plasma and with to the surface diffused sodium compounds by the applied electric field. A schematic view of this hypothesis is presented in Figure 45. However more research should be done in order to prove the hypothesis. First of all, gas-phase FTIR measurements on the exhaust gas produced in the plasma, are going to be performed in the near future. In order to identify and quantify the produced species (NO_x-related). Secondly, some effort should be given to determine the electric field strength near the glass substrate in the µPP during discharge, which could explain the dissociation of Na^+ ions from Na_2O in the substrate.

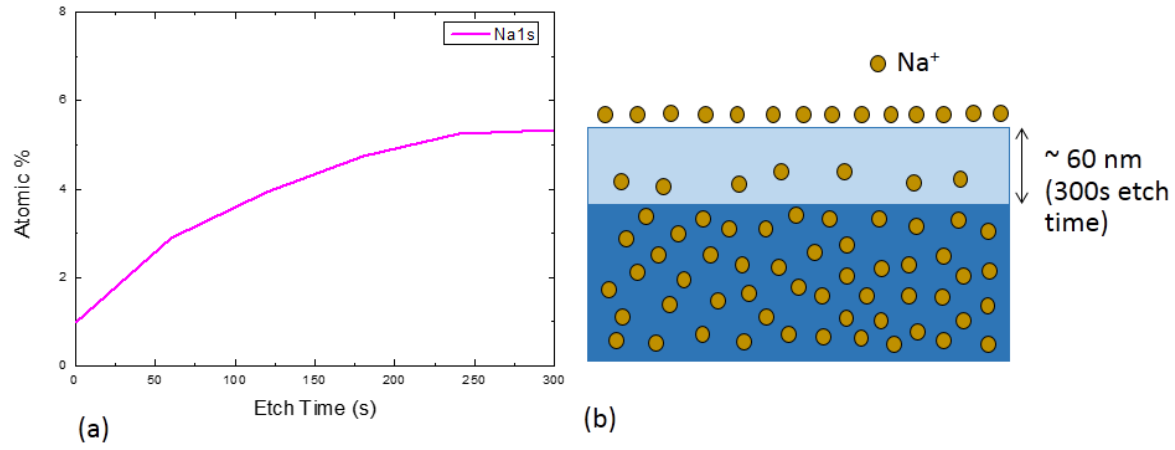

Figure 44: (a) Sodium concentration as function of etch time (s) in an O_2-µPlasma treated silicate glass substrate (10 sccm O_2, 30 PR), determined by XPS. The etch rate is 0.2 nm/s, therefore the figure can be presented as an atomic concentration as function of depth (0-60 nm). The amount of sodium increased from 1 to 5% with increasing depth (etch time) in the first 50 nm. Indicating that the sodium species in the top 50 nm layer were used for the crystal formation. (b) Schematic view of the sodium concentration in the substrate after plasma treatment.

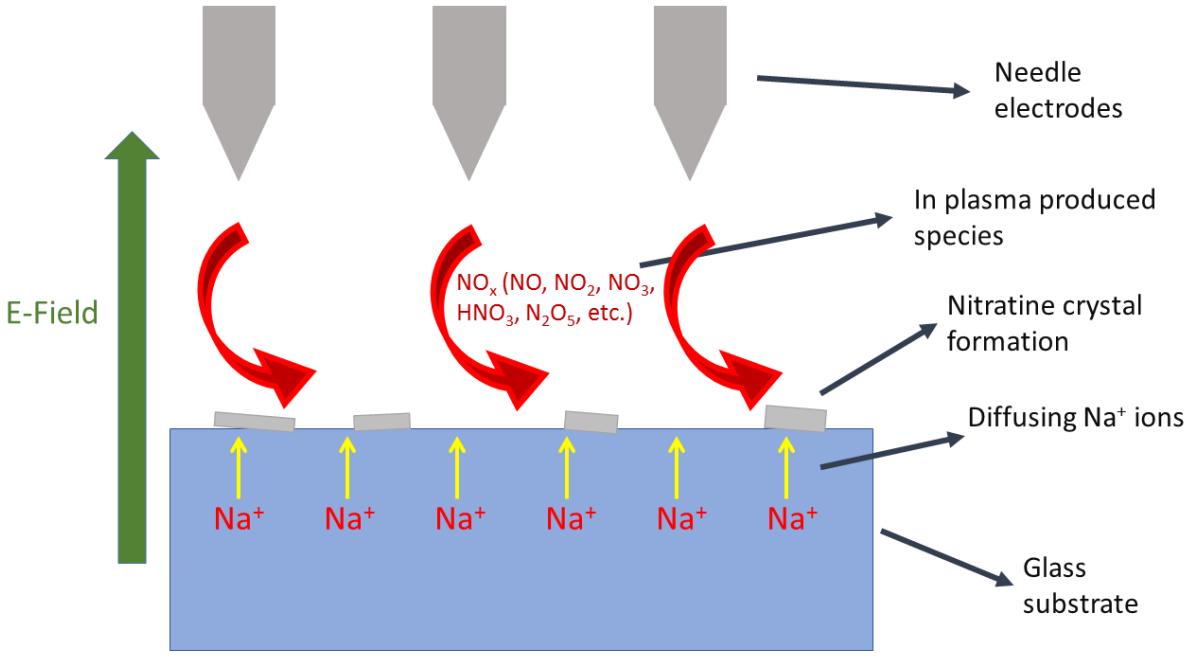

Figure 45: Schematic view of the Nitratine crystal formation (hypothesis). Sodium ions (Na^+) diffuse to the substrate's surface by the appliance of a strong electric field, due to the filamentary discharges and NO_x related species are produced in the plasma. The NO_x species react chemically with the diffused sodium ions in order to form Nitratine crystals.

5. Conclusions and outlook

In this Master Thesis the possibility to deposit patterned metal oxides thin films, i.e. TiO_2, with the µPP as a plasma source has been proven. The depositions were performed in two different operation modes, PE-CVD and plasma-assisted ALD mode. In PE-CVD, a vaporized titanium precursor (TTIP) was fed into the discharge volume by means of a nitrogen carrier gas. For the second part of this Master Thesis, the µPP was upgraded to a plasma-assisted ALD system, through the integration of a precursor dosing head.

The conclusions and answers to the research questions are given in section 5.1, followed by an outlook for future experiments and system modifications in section 5.2.

5.1 Conclusions

Answers to the research questions are provided in this section. The questions were divided in two large questions with multiple sub-questions. The first question was stated as follow:

1. ***Can the µPP, which is initially used for plasma activation of surfaces, be used for deposition of metal oxides thin films (e.g. titanium dioxide) in a patterned manner (PE-CVD mode)?***

The µPP was used to deposit metal oxides thin films (i.e. TiO_2) in a patterned manner by guiding a vaporized titanium precursor (TTIP) to the discharge volume. The films were deposited both on glass and Si substrates. The required hardware modifications and material properties are addressed in the answers to the sub-questions.

a. ***What are the required hardware modifications to enable metal oxides thin film deposition with the µPP?***

The µPP had never been used to deposit metal oxides thin films and numerous hardware modifications were required. First of all, the polymer precursor lines were replaced by stainless steel flexible lines. The polymer lines absorb water, which is reactive with the TTIP precursor. TTIP has a melting point of 17-18°C, therefore a precursor heating system was added to prevent solidification of the precursor inside the bubbler. In order to prevent condensation of the 'warmer' precursor inside the lines, gas chamber and on the substrate, heating systems for the lines, gas chamber and substrate were designed and added to the setup. Finally, a gas curtain system was designed to enclose the gas mixture and print head from the environment. The required hardware modifications are well described in Appendix B.

b. ***What is the growth rate of the deposited film? Is there a difference when depositing on dielectric or conductive substrates (i.e. difference between both plasma configurations)?***

The growth rate on glass substrate was 2.3 nm/PR and decreased to 2.0 nm/PR by adding 10 sccm O_2 to the gas mixture. The O-related plasma species (e.g. O-radicals) react with the isopropyl ligands of the TTIP molecule and form volatile byproducts and a more dense TiO_2 film. The growth rate was lower on Si substrate, 1.33 nm/PR. However µPlasmaPrinting on a conductive substrate requires a change in configuration and the precursor flow and pump speed were different.

c. What are the properties? What is the stoichiometry, impurity content, etc.? And how do the properties (stoichiometry, roughness, etc.) compare with those achieved with other CVD systems?

The TiO_2 films contained carbon and nitrogen as impurities, according to XPS measurements. The amount of carbon in films deposited on glass substrate decreased from 10.7 to 4.9%, while nitrogen decreased from 3.4 to 1.7% by adding 10 sccm O_2 to the gas mixture, which also explains the decreased growth rate. The carbon and nitrogen content in films on Si substrate was measured 7.5 and 0.5%, respectively. The lower amount of carbon and nitrogen in films on Si substrate in comparison with glass substrate is most likely explained by the difference in configuration. The stoichiometry of the TiO_2 films in PE-CVD mode was found to be 2.15– 2.60, depending on the gas mixture and type of substrate.

The SEM images of TiO_2 films on Si substrate showed a smooth and uniform surface. While the surface of TiO_2 films on glass substrate was rough and composed of agglomerated particles. The R_{MS} roughness was determined by AFM and was significantly different between the two substrate types. The TiO_2 film was smooth on Si substrate, a R_{MS} roughness of 0.25 nm was measured. The film on glass substrate was rough, with a R_{MS} roughness of 11 nm and decreased to 4 nm by adding O_2 to the gas mixture. The large difference in surface roughness between films on Si and glass substrates is explained by charge buildup on the dielectric substrate (i.e. glass) upon discharge. The RI index was only determined for TiO_2 film on Si substrate and was measured 1.81 on a 50 nm thick film.

The stoichiometry and R_{MS} roughness correspond with TiO_2 films deposited in other reported CVD systems with TTIP as precursor. The RI is rather low in comparison with other reported processes, indicating a relatively low mass density. The growth rate obtained with the PE-CVD µPP setup was significantly larger than other reported values in the literature, however those were not local and patterned depositions and therefore difficult to compare with. The amount of carbon in TiO_2 films is rather large, compared with other CVD processes. Therefore the material quality achieved with the µPP in PE-CVD mode was relatively poor and the possibility to achieve an improvement in material quality was investigated. An overview of other in the literature reported CVD processes and corresponding material properties can be found in Appendix F.

d. What is the patterning resolution of the µPP, when depositing TiO_2 thin films in PE-CVD mode?

The resolution was determined by means of XPS line-scan and was found to be approximately 1600 µm for a 20 plasma PR TiO_2 line. However it is expected that the resolution is dependent to the stability of the plasma and is influenced by the concentration of TTIP molecules in the discharge volume. It is worth mentioning that the carrier gas flow remained the same as for larger area depositions (with multiple needles), due to limitations in the current setup. Therefore it is expected that the concentration of TTIP molecules in the discharge volume was too large for one single needle electrode. A too large precursor concentration manifests in an occasionally very bright and/or weak plasma and thereby influencing the line width of the deposition. It was also observed that the growth rate was affected by the number of activated needle electrodes, therefore the PE-CVD mode provides no accurate thickness control for small area features.

Due to the relatively low RI (1.81) and large amount of carbon in the TiO_2 films (7.5% in case of Si substrate) deposited by guiding the vaporized TTIP precursor directly into the discharge volume (PE-CVD mode). The possibility to achieve an improvement in material properties by the spatial separation of precursor and oxidant exposures was investigated (Plasma-assisted ALD mode). The second research question was stated as follow:

2. *Can the µPP be modified in order to achieve successful plasma-assisted atomic layer deposition of metal oxides (e.g. TiO_2) in a patterned manner?*

The µPP was upgraded from a PE-CVD to a µ-Plasma assisted ALD setup. The possibility to deposit TiO_2 ALD films with the µPP as plasma source was proven. The required hardware modifications, process development and material properties are given in the answers to the sub-questions.

a. What are the required hardware modifications?

In order to enable ALD with the µPP setup, a precursor dosing head was designed and integrated at the print-stage. The dosing head served as one half-cycle, while the O_2 plasma exposure by the plasma print head served as the other half-cycle in the ALD-process. The substrate was alternatively exposed to TTIP precursor and O_2-plasma by the alternate shifting of both heads over the substrate. In order to separate both heads (plasma en precursor) from each other and from the environment, a different gas curtain system was designed and integrated in the setup.

b. What is the ALD process development?

A set of saturation experiments were performed to determine the required precursor exposure, plasma exposure and purge times to achieve self-limiting surface reactions. The GPC remained constant at 0.145 nm/cycle with 10s of extra purge time, when 475 ms precursor exposure time and one plasma PR per ALD-cycle were applied. The influence of plasma exposure time on the GPC was not as important as the precursor exposure and purge time.

c. What are the properties of the material? What is the effect of the number of plasma PR per ALD – cycle, i.e. plasma exposure time?

The surface of TiO_2 ALD film was smooth and uniform, according to SEM and AFM images. The R_{MS} roughness was measured 0.25 nm, similar to the roughness of a pristine Si substrate with native oxide. The RI increased with increasing plasma exposure time and was measured 1.97 on a TiO_2 film deposited at saturation conditions with 10 plasma PR per ALD-cycle. The relatively low RI indicates a low material mass density, as confirmed by RBS measurements, which showed a material density of 1.70-2.04 g/cm^3. The TiO_2 films contained carbon and nitrogen as impurities according to XPS measurements. An overview of the material properties can be found in Table 8 and Appendix F.

The influence of increasing plasma exposure time, i.e. number of plasma PR per ALD-cycle was investigated by means of XPS and RBS/ERD measurements. The amount of carbon and nitrogen in the TiO_2 films decreased from 5 to 0.9% and from 3.0 to 1.8% respectively, by increasing the number of plasma PR per ALD-cycle from one to ten, according to XPS measurements. The same effect was observed in the hydrogen content, according to RBS/ERD measurements. The increase in O_2-plasma exposure time per cycle leads to an increased amount of produced O-related plasma species, which chemically react with the hydrocarbon ligands of the absorbed TTIP molecule and form volatile products. Therefore an almost carbon-free TiO_2 layer can be deposited provided sufficient plasma exposure time. The O/Ti ratio increased from 2.05 to 2.20 with increasing plasma exposure time,

according to RBS measurements. The material density increased from 1.7 to 2.04 g/cm³, while the number of deposited Ti atoms per ALD-cycle increased from 2.2 to 2.4 at/nm².cycle by increasing the plasma exposure time. Therefore increasing the O_2 plasma exposure time per cycle, leads to the formation of a denser and more pure TiO_2 film.

d. What is the patterning resolution of the µPP in plasma-assisted ALD mode? How does the resolution change in comparison with the PE-CVD mode?

The patterning resolution of the µPP in plasma-assisted ALD mode was found to be approximately 1400 µm for a TiO_2 line deposited with 50 ALD-cycles at saturation conditions and activation of two consecutive needle electrodes. Due to limitations in system's design, no TiO_2 line could be deposited in ALD mode by activation of only one needle electrode. The resolution in PE-CVD mode was 1600 µm for a 20 plasma PR TiO_2 line and activation of only one single needle electrode, hence the ALD mode leads to an enhanced patterning resolution. Moreover, the growth rate in PE-CVD mode was affected by the number of activated needle electrodes, while in ALD mode, the growth was independent from the number of activated needles. Therefore ALD mode provides a more accurate thickness control for small area features.

e. How do the properties (stoichiometry, impurity content, roughness, etc.) change in comparison with the PE-CVD mode? And how do these properties compare with other ALD processes?

The growth rate on Si substrate in PE-CVD mode was 1.33 nm/PR, while 0.145 nm/cycle at saturation conditions in plasma-assisted ALD mode. Hence the ALD mode makes it possible to deposit TiO_2 films with sub-nanometer growth control by controlling the number of ALD-cycles. The surface of TiO_2 films deposited by PE-CVD and plasma-assisted ALD were smooth, with a R_{MS} roughness of 0.25 nm. The RI increased from 1.81 in PE-CVD mode to 1.97 in ALD mode, indicating an increased material mass density. Carbon and nitrogen were present in the TiO_2 films as impurities, in both situations, according to XPS measurements. The amount of carbon decreased from 7.5% in PE-CVD mode to less than one percent in plasma-assisted ALD mode, provided sufficient O_2-plasma exposure time. The amount of nitrogen increased from 0.5% in PE-CVD mode to 1.8% in ALD mode, most likely due to an increased production rate of NO_x related plasma species in a N_2/O_2 gas mixture than in an N_2/O_2/TTIP gas mixture. The O/Ti ratio was 2.15 in PE-CVD mode and 2.05-2.20 in ALD mode. However the ratio in PE-CVD mode was determined by XPS (without sputtering) and by RBS/ERD measurements in ALD mode.

The growth rate, surface roughness, O/Ti ratio and amount of impurities (i.e. carbon, nitrogen and hydrogen) correspond with other in the literature reported ALD processes (Table 11). The RI and mass density were relatively low in comparison with other reported ALD processes, however it is expected that an increase in mass density and RI can be achieved by increasing the substrate temperature during the ALD process. The number of deposited Ti atoms per ALD-cycle in the µPP ALD setup (2.2-2.4 at/nm².cycle) was significant higher than values reported in the literature (0.9 at/nm².cycle), which could possibly suggest that the µPP ALD process is not completely pure ALD but more an ALD-like process. However calculations showed that the atomic areal density of one TiO_2 monolayer is approximately 4.8 titanium at/nm² (depending on the bulk mass density) and therefore half a monolayer is deposited in each ALD-cycle. An overview and comparison of other in the literature reported TiO_2 ALD processes and properties can be found in Table 11, Appendix F.

5.2 Outlook

In this thesis the possibility to deposit metal oxides thin films with the µPP as a plasma source in two different operation modes (PE-CVD and plasma-assisted ALD mode) has been proven. The possibility to perform patterned plasma-assisted ALD at atmospheric pressure is something unique and could be applicable in numerous applications or the µPP-head could possibly be implemented in other spatial ALD systems. However the µPP ALD system is a prototype and more research should be done in order to further improve and modify the system in a µ-Plasma assisted ALD Printer. In this section suggestions are given in order to further investigate and improve the prototype system and the corresponding TiO_2 thin films.

First of all, no TiO_2 ALD line could be deposited with activation of only one needle electrode in the present setup, due to a too large concentration of O_2 for one single needle electrode in the discharge volume. Therefore, single needle TiO_2 line samples should be deposited by using a MFC, allowing a lower gas flow (0-5 sccm O_2). The patterning resolution of the µPP in ALD mode can then be determined for one single needle electrode and a more accurate comparison of the resolution in PE-CVD and ALD mode can be made. Secondly, the influence of substrate temperature on the growth rate, chemical composition, mass density and optical properties should be investigated. Most other reported (plasma-assisted) ALD processes are operated with higher substrate temperatures and an increase in material density and RI is expected by increasing the substrate temperature. Finally, the prototype system has been used to deposit TiO_2 films with TTIP as titanium precursor. However the system should also be tested with other precursors and/or different types of metal-oxides.

As already mentioned, the µPP ALD-system is a prototype and further improvements are necessary to upgrade the system in a commercially available µ-Plasma assisted ALD Printer. First of all, the precursor exposure time is dependent to the motion speed of the print-stage as well as to the size (i.e. length) of the dosing head, limiting the current setup to a minimum precursor exposure time of 315 ms. However, it was shown that self-limiting surface reactions are already achieved after 475 ms of precursor exposure. Thereby, decreasing the size of the dosing head makes it possible to decrease the minimum precursor exposure time and the growth in the region before saturation could be investigated. Secondly, the purge steps are performed during transition between both heads by a combination of N_2-flow from the gas curtain system, O_2-flow to the inlet of plasma head and exhaust flow through the outlet by a vacuum pump. However extra purge times were required, limiting the process speed significantly. Therefore the addition of an extra purge module/zone between both heads (plasma and precursor) should reduce the purge time and increase the process speed significantly.

Finally some suggestions are given for further investigation of the growth mechanism of the Nitratine crystals (section 4.3). First, gas-phase FTIR measurements on the produced exhaust gas are going to be performed in the near future. The measurements should identify and quantify the produced plasma species (e.g. NO_x). Secondly, some effort should be given to determine the electric field in the µPP during discharge.

6. References

1. Mackus, A.J.M., Bol, A.A., Kessels, W. M. . The use of atomic layer deposition in advanced nanopatterning. *Nanoscale* **6,** 10941–10960 (2014).
2. Levy, D. H., Nelson, S. F. & Freeman, D. Oxide Electronics by Spatial Atomic Layer Deposition. *J. Disp. Technol.* **5,** 484–494 (2009).
3. Levy, D. H., Ellinger, C. R. & Nelson, S. F. Metal-oxide thin-film transistors patterned by printing. *Appl. Phys. Lett.* **103,** (2013).
4. Kreitz, S., Penache, C., Thomas, M. & Klages, C. P. Patterned DBD treatment for area-selective metallization of polymers-plasma printing. *Surf. Coatings Technol.* **200,** 676–679 (2005).
5. F. Roozeboom, W. M. M. K. Lecture Notes Plasma & Materials Processing. (2014).
6. https://www.bloomberg.com/news/articles/2016-06-09/how-intel-makes-a-chip. (2016).
7. Breen, T. L., Fryer, P. M., Nunes, R. W. & Rothwell, M. E. Patterning Indium Tin Oxide and Indium Zinc Oxide Using Microcontact Printing and Wet Etching. *Society* **18,** 194–197 (2002).
8. Choi, H. W., Farson, D. F., Bovatsek, J., Arai, a & Ashkenasi, D. Direct-write patterning of indium-tin-oxide film by high pulse repetition frequency femtosecond laser ablation. *Appl. Opt.* **46,** 5792–5799 (2007).
9. Iu, Y. A. N. G. L., Ee, J. U. H. W. A. N. L. & Eo, D. A. E. H. I. K. S. Ion beam fabrication of aluminum-doped zinc oxide layer for high-performance liquid crystals alignment. **24,** 17424–17432 (2016).
10. Farahani, R. D., Dubé, M. & Therriault, D. Three-Dimensional Printing of Multifunctional Nanocomposites: Manufacturing Techniques and Applications. *Adv. Mater.* 5794–5821 (2016). doi:10.1002/adma.201506215
11. Huiskamp, T. & Stevens, A. PUSHING THE FRONTIERS OF PLASMA PRINTING BY PULSED POWER TECHNOLOGY.
12. Schalken, J.-P. M . Sc . Thesis Jean-Paul Schalken µ PlasmaPrinting of amine-containing polymer lms using APTMS (3-aminopropyl trimethoxysilane). (2014).
13. Dongen, M. van. µPlasma patterning and inkjet printing to enhance localized wetting and mixing behavior. (2014).
14. Pierson, H. O., Publishing, W. A. & York, N. *Handbook of chemical vapor deposition: principles, technology and applications*. (1999).
15. George, S. M. Atomic layer deposition: An overview. *Chem. Rev.* 111–131 (2010). doi:10.1021/cr900056b
16. Profijt, H. B., Potts, S. E., van de Sanden, M. C. M. & Kessels, W. M. M. Plasma-Assisted Atomic Layer Deposition: Basics, Opportunities, and Challenges. *J. Vac. Sci. Technol. A Vacuum, Surfaces, Film.* **29,** 50801 (2011).
17. Peeters, F. The Electrical Dynamics of Dielectric Barrier Discharges. (Technical University Eindhoven, 2015).
18. Borcia, G., Borcia, C. & Dumitrascu, N. Temporal evolution of pulsed atmospheric pressure

DBD in asymmetric configuration. *Rom. Reports Phys.* **54,** 689–697 (2009).

19. Bittencourt, J. A. Fundamentals of Plasma Physics. (2010).

20. Kostov, K. & Honda, R. Characteristics of dielectric barrier discharge reactor for material treatment. *Brazilian J. …* **1,** 322–325 (2009).

21. Peeters, F. J. J. & van de Sanden, M. C. M. The influence of partial surface discharging on the electrical characterization of DBDs. *Plasma Sources Sci. Technol.* **24,** 15016 (2015).

22. Kogelschatz, U., Eliasson, B., Egli, W., France, P. I. V & Abb, E. Dielectric-Barrier Discharges. Principle and Applications. *J. Phys. IV Fr. 7 Colloq. C4, supplément au J. Phys. III* **7,** C4-47-66 (1997).

23. Tyata, R. B., Subedi, D. P., Wong, C. S. & Lumpur, K. Comparison of Dielectric Barrier Discharge in Air ,. **6,** 6–10 (2010).

24. Merbahi, N., Sewraj, N., Marchal, F., Salamero, Y. & Millet, P. Luminescence of argon in a spatially stabilized mono-filamentary dielectric barrier micro-discharge: spectroscopic and kinetic analysis. *J. Phys. D. Appl. Phys.* **37,** 1664–1678 (2004).

25. Kogelschatz, U. & Kogelschatz, U. Discharge Physics, and Industrial Applications". **23,** 1–46 (2003).

26. K. H. Becker, U. Kogelschatz, K. H. S. and R. J. B. Non-Equilibrium Air Plasmas At Atmospheric Pressure. 682 (2005).

27. Sublet, a *et al.* Atmospheric and sub-atmospheric dielectric barrier discharges in helium and nitrogen. *Plasma Sources Sci. Technol.* **15,** 627–634 (2006).

28. A. Sobota. Lecture Notes - Gas Discharges course TU/e. (2015).

29. Alexandre, V. Stability of atmospheric pressure glow discharges. *Thesis* (2005).

30. Chirokov, a., Gutsol, a. & Fridman, a. Atmospheric pressure plasma of dielectric barrier discharges. *Pure Appl. Chem.* **77,** 487–495 (2005).

31. Papageorghiou, L., Panousis, E., Loiseau, J. F., Spyrou, N. & Held, B. Two-dimensional modelling of a nitrogen dielectric barrier discharge (DBD) at atmospheric pressure: filament dynamics with the dielectric barrier on the cathode. *J. Phys. D. Appl. Phys.* **42,** 105201 (2009).

32. Joerie, V. (PMP T. Atmospheric pressure micro-discharge current characterization. (2015).

33. Potts, S. E., Profijt, H. B., Roelofs, R. & Kessels, W. M. M. Room-temperature ALD of metal oxide thin films by energy-enhanced ALD. *Chem. Vap. Depos.* **19,** 125–133 (2013).

34. Chaukulkar, R. P. & Agarwal, S. Atomic layer deposition of titanium dioxide using titanium tetrachloride and titanium tetraisopropoxide as precursors. *J. Vac. Sci. Technol. A Vacuum, Surfaces, Film.* **31,** 31509 (2013).

35. Niskanen, a, Arstila, K., Leskela, M. & Ritala, M. Radical enhanced atomic layer deposition of titanium dioxide. *Chem. Vap. Depos.* **13,** 152–157 (2007).

36. Poodt, P. *et al.* High-speed spatial atomic-layer deposition of aluminum oxide layers for solar cell passivation. *Adv. Mater.* **22,** 3564–3567 (2010).

37. Aghaee, M. *et al.* Low temperature temporal and spatial atomic layer deposition of TiO2 films. *J. Vac. Sci. Technol. A Vacuum, Surfaces, Film.* **33,** 41512 (2015).

38. Poodt, P., Kniknie, B., Branca, A., Winands, H. & Roozeboom, F. Patterned deposition by plasma enhanced spatial atomic layer deposition. *Phys. Status Solidi - Rapid Res. Lett.* **5,** 165–167 (2011).

39. van den Bruele, F. J. *et al.* Atmospheric pressure plasma enhanced spatial ALD of silver. *J. Vac. Sci. Technol. A Vacuum, Surfaces, Film.* **33,** 01A131 (2015).

40. Theirich, D. *et al.* Atmospheric pressure plasma ALD of titanium oxide. *Chem. Vap. Depos.* **19,** 167–173 (2013).

41. Tallarida, M., Friedrich, D., Städter, M., Michling, M. & Schmeisser, D. Growth of TiO2 with thermal and plasma enhanced atomic layer deposition. *J. Nanosci. Nanotechnol.* **11,** 8049–53 (2011).

42. Sinha, A., Hess, D. W. & Henderson, C. L. Area selective atomic layer deposition of titanium dioxide: Effect of precursor chemistry. *J. Vac. Sci. Technol. B Microelectron. Nanom. Struct.* **24,** 2523 (2006).

43. Barkhouse, D. A. R., Gunawan, O., Gokmen, T., Todorov, T. K. & Mitzi, D. B. Device characteristics of a 10.1% hydrazine-processed Cu2ZnSn(Se,S)4 solar cell. *Prog. Photovoltaics Res. Appl.* **20,** 6–11 (2012).

44. Xie, Q. *et al.* Atomic layer deposition of TiO[sub 2] from tetrakis-dimethyl-amido titanium or Ti isopropoxide precursors and H[sub 2]O. *J. Appl. Phys.* **102,** 83521 (2007).

45. Processing, M. Atomic Layer Deposition of In 2 O 3 : growth , morphology and hydrogen doping Dries Vanhemel. (2015).

46. Wang, X., Wu, G., Zhou, B. & Shen, J. Optical constants of crystallized TiO2 coatings prepared by sol-gel process. *Materials (Basel).* **6,** 2819–2830 (2013).

47. van Drunen, M. Atomic Layer Deposition of Silicon Nitride from novel precursor DSBAS and nitrogen plasma. (2015).

48. Rajiv Hemani. Depth selective laser crystallization of evaporated Boron-doped a-Si using femtosecond laser. (2014).

49. Benjamin, G. ALD of Ruthenium thin films fro EBECHRu: Surface chemistry, film properties and applications. *Thesis PMP* (2014). doi:10.1016/B978-0-444-59561-4.00018-8

50. Butt, H. J., Cappella, B. & Kappl, M. Force measurements with the atomic force microscope: Technique, interpretation and applications. *Surf. Sci. Rep.* **59,** 1–152 (2005).

51. Processing, M. & Damen, M. A. Measuring precursor residence times using Electron-Beam-Induced Deposition pillar growth. (2014).

52. Poulus, R. J. An Optimization of Graphene Growth by Chemical Vapor Deposition. (2014).

53. Faraz, T., Roozeboom, F., Knoops, H. C. M. & Kessels, W. M. M. Atomic Layer Etching: What Can We Learn from Atomic Layer Deposition? *ECS J. Solid State Sci. Technol.* **4,** N5023–N5032 (2015).

54. Arts, K. On the influence of ICP-PECVD deposition paramaters and annealing on the properties of a-Si:H passivation layers. (2014).

55. Mohammed, M. A. Atomic layer deposition of passivation layers for hybrid organo - lead halide perovskite solar cells. (2015).

56. R. d'Agostino, F. Cramarossa, F. F. Plasma polymerization of Fluorocarbons. *Plasma Depos. Treat. Etch. Polym.* 95 (1990).

57. Klenko, Y. & Píchal, J. DEPOSITION OF TiO 2 THIN FILMS USING ATMOSPHERIC DIELECTRIC BARRIER DISCHARGE. 177–179 (2008).

58. Xiwen, Z., Yu, G. & Gaorong, H. Fabrication of Titanium Dioxide Thin Films by DBD-CVD Under Atmosphere. *Plasma Sci. Technol.* **9,** 674–677 (2007).

59. Rahman, a. *et al.* Absolute UV and VUV emission in the 100-400 nm region from 13.56 MHz driven hollow slot microplasmas operating in open air. *31st IEEE Int. Conf. Plasma Sci. 2004. ICOPS 2004. IEEE Conf. Rec. - Abstr.* **13,** 537–547 (2004).

60. Cicala, G., Creatore, M., Favia, P., Lamendola, R. & D'Agostino, R. Modulated rf discharges as an effective tool for selecting excited species. *Appl. Phys. Lett.* **75,** 37–39 (1999).

61. Nassar, H. *et al.* N 2 + /N 2 ratio and temperature measurements based on the first negative N 2 + and second positive N 2 overlapped molecular emission spectra. *J. Phys. D. Appl. Phys.* **37,** 1904 (2004).

62. Battiston, G. a *et al.* PECVD of amorphous TiO 2 thin films : effect of growth temperature and plasma gas composition. *Thin Solid Films* **371,** 126–131 (2000).

63. Jiménez, C. *et al.* Deposition of TiO 2 thin films by atmospheric plasma post-discharge assisted injection MOCVD. *Surf. Coatings Technol.* **201,** 8971–8975 (2007).

64. Gazal, Y. *et al.* Multi-structural TiO2 film synthesised by an atmospheric pressure plasma-enhanced chemical vapour deposition microwave torch. *Thin Solid Films* **600,** 43–52 (2016).

65. Monoy, A. *et al.* Surface preparation influence on the initial stages of MOCVD growth of TiO2 thin films. *Thin Solid Films* **515,** 687–690 (2006).

66. Heo, C. H., Lee, S.-B. & Boo, J.-H. Deposition of TiO2 thin films using RF magnetron sputtering method and study of their surface characteristics. *Thin Solid Films* **475,** 183–188 (2005).

67. Klenko, Y. & Pichal, J. TiOx films deposited by plasma enhanced chemical vapour deposition method in atmospheric dielectric barrier discharge plasma. *Plasma Chem. Plasma Process.* **32,** 1215–1225 (2012).

68. Masuda, Y., Jinbo, Y. & Koumoto, K. Room Temperature CVD of TiO₂ Thin Films and Their Electronic Properties. *Sci. Adv. Mater.* **1,** 138–143 (2009).

69. Chen, Q. *et al.* Synthesis of TiO 2 porous films by atmospheric dielectric barrier discharge plasma at room temperature. 6–8 (2015).

70. Lee, S. H., Yamasue, E., Ishihara, K. N. & Okumura, H. Photocatalysis and surface doping states of N-doped TiOx films prepared by reactive sputtering with dry air. *Appl. Catal. B Environ.* **93,** 217–226 (2010).

71. Fakhouri, H., Salem, D. Ben, Carton, O., Pulpytel, J. & Arefi-Khonsari, F. Highly efficient photocatalytic TiO 2 coatings deposited by open air atmospheric pressure plasma jet with aerosolized TTIP precursor. *J. Phys. D. Appl. Phys.* **47,** 265301 (2014).

72. Laidani, N. *et al.* Intrinsic defects and their influence on the chemical and optical properties of TiO 2− x films. *J. Phys. D. Appl. Phys.* **43,** 485402 (2010).

73. Satoshi Hashimoto, Aki Murata, T. S. and A. T. Alternation of Ti 2p XPS Spectrum for TiO2 by Ar Ion Bombardment. *J. Surf. Anal.* (2002).

74. Hashimoto, S., Tanaka, A., Murata, A. & Sakurada, T. Formulation for XPS spectral change of oxides by ion bombardment as a function of sputtering time. *Surf. Sci.* **556,** 22–32 (2004).

75. Matsui, H., Tabata, H., Hasuike, N., Harima, H. & Mizobuchi, B. Epitaxial growth and characteristics of N-doped anatase TiO2 films grown using a free-radical nitrogen oxide source. *J. Appl. Phys.* **97,** 123511 (2005).

76. Shelemin, A., Choukourov, A., Kousal, J., Slav??nsk??, D. & Biederman, H. Nitrogen-doped TiO2 nanoparticles and their composites with plasma polymer as deposited by atmospheric pressure DBD. *Steel Res. Int.* **11,** 864–877 (2014).

77. Brevet, A., Peterlé, P. M., Imhoff, L., Marco De Lucas, M. C. & Bourgeois, S. Initial stages of TiO2 thin films MOCVD growth studied by in situ surface analyses. *J. Cryst. Growth* **275,** 4–6 (2005).

78. Cong, Y., Zhang, J., Chen, F. & Anpo, M. Synthesis and characterization of nitrogen-doped TiO2 nanophotocatalyst with high visible light activity. *J. Phys. Chem. C* **111,** 6976–6982 (2007).

79. Hodgkinson, J. L., Massey, D. & Sheel, D. W. The deposition of copper-based thin films via atmospheric pressure plasma-enhanced CVD. *Surf. Coatings Technol.* **230,** 260–265 (2013).

80. Pichal, J. & Klenko, J. Positioning of the precursor gas inlet in an atmospheric dielectric barrier reactor, and its effect on the quality of deposited TiOx thin film surface. *Acta Polytech.* **53,** 223–227 (2013).

81. Magnuson, M., Lewin, E., Hultman, L. & Jansson, U. Electronic structure and chemical bonding of nc-TiC/a-C nanocomposites. *Phys. Rev.* **80,** 1–13 (2009).

82. Lewin, E., Gorgoi, M., Schäfers, F., Svensson, S. & Jansson, U. Influence of sputter damage on the XPS analysis of metastable nanocomposite coatings. *Surf. Coatings Technol.* **204,** 455–462 (2009).

83. Shui Jinn Wanga, H. Y. T. and S. C. S. Characterization of Sputtered Titanium Carbide Film as Diffusion Barrier for Copper Metallization. *ECS* (2001).

84. Pechereau, F. Numerical simulation of the interaction of a plasma discharge at atmospheric pressure with dielectric surfaces. **1,** (2013).

85. Knoops, B. H. C. M., Potts, S. E., Bol, A. A. & Kessels, W. M. M. Atomic Layer Deposition (Pre-Print Chapter). 1–28

86. Sarkar, A., Potts, S. E., Rushworth, S. A., Roozeboom, F. & Sanden, M. C. M. Van De. Plasma-Enhanced ALD of TiO2 using a Novel Cyclopentadienyl Alkylamido Precursor [Ti(Cp^{Me})(NMe2)3] and O2 plasma. *ECS Trans.* **33,** 385–393 (2010).

87. Das, C. *et al.* Thermal and plasma enhanced atomic layer deposition of TiO2: Comparison of spectroscopic and electric properties. *J. Vac. Sci. Technol. A Vacuum, Surfaces, Film.* **144,** (2015).

88. Ratzsch, S., Kley, E.-B., Tünnermann, A. & Szeghalmi, A. Influence of the oxygen plasma parameters on the atomic layer deposition of titanium dioxide. *Nanotechnology* **26,** 24003 (2015).

89. Cornelissen, L. E. In situ infrared spectroscopy for plasma-assisted ALD of SiNx films. 2015 (2015).

90. Talimian, A. & Sglavo, V. M. Electric Field-Assisted Ion Exchange of Borosilicate Glass Tubes. *Ion Exch. - Stud. Appl.* (2015).

91. Wassilkowska, A., Czaplicka-Kotas, A., Zielina, M. & Bielski, A. an Analysis of the Elemental Composition of Micro-Samples Using Eds Technique. *Czas. Tech.* **2014,** 133–148 (2015).

92. Engelhardt, M. *et al.* Interaction of an argon plasma jet with a silicon wafer. *J. Phys. D. Appl. Phys.* **49,** 145201 (2016).

93. Benages-Vilau, R., Calvet, T., Pastero, L., Aquilano, D. & Cuevas-Diarte, M. À. Morphology Change of Nitratine (NaNO3) from Aqueous Solution, in the Presence of Li+ and K+ Ions. *Cryst. Growth Des.* **15,** 5338–5344 (2015).

94. Potgieter-Vermaak, S., Horemans, B., Anaf, W., Cardell, C. & Grieken, R. Van. Degradation potential of airborne particulate matter at the Alhambra monument: A Raman spectroscopic and electron probe X-ray microanalysis study. *J. Raman Spectrosc.* **43,** 1570–1577 (2012).

95. Shelby, J. E. & Vitko, J. The reduction of iron in soda-lime-silicate glasses by reaction with hydrogen. *J. Non. Cryst. Solids* **53,** 155–163 (1982).

96. Estournès, C., Cornu, N. & Guille, J. L. Reduction of copper in soda-lime-silicate glass by hydrogen. *J. Non. Cryst. Solids* **170,** 287–294 (1994).

97. Potts, S. E. *et al.* Low Temperature Plasma-Enhanced Atomic Layer Deposition of Metal Oxide Thin Films. *J. Electrochem. Soc.* **157,** P66 (2010).

98. Zhu, X. M. & Kong, M. G. Electron kinetic effects in atmospheric dielectric-barrier glow discharges. *J. Appl. Phys.* **97,** (2005).

99. Liu, Y. *et al.* Infrared gas phase studies on plasma-polymer interaction in high-current dielectric barrier discharges. 5–7 (2015).

100. Schmidt-Bleker, A., Winter, J., Bösel, A., Reuter, S. & Weltmann, K.-D. On the plasma chemistry of a cold atmospheric argon plasma jet with shielding gas device. *Plasma Sources Sci. Technol.* **25,** 15005 (2016).

101. Riccardi, C. & Barni, R. Chemical Kinetics in Air Plasmas at Atmospheric Pressure. *Chem. Kinet.* 185–201 (2012). doi:10.5772/1990

102. Parsons, G. N. *et al.* History of atomic layer deposition and its relationship with the American Vacuum Society. *J. Vac. Sci. Technol. A Vacuum, Surfaces, Film.* **31,** 50818 (2013).

103. Munoz-Rojas, D. & MacManus-Driscoll, J. Spatial Atmospheric Atomic Layer Deposition: A new laboratory and industrial tool for low-cost photovoltaics. *Mater. Horizons* 314–320 (2014). doi:10.1039/C3MH00136A

104. Musschoot, J. *et al.* Comparison of Thermal and Plasma-Enhanced ALD/CVD of Vanadium Pentoxide. *J. Electrochem. Soc.* **156,** P122 (2009).

105. Poodt, P. *et al.* Spatial atomic layer deposition: A route towards further industrialization of atomic layer deposition. *J. Vac. Sci. Technol. A Vacuum, Surfaces, Film.* **30,** 10802 (2012).

106. van den Bruele, F. J. *et al.* Atmospheric pressure plasma enhanced spatial ALD of silver. *J. Vac. Sci. Technol. A Vacuum, Surfaces, Film.* **33,** 01A131 (2015).

107. Coburn, J. W. & Chen, M. Optical emission spectroscopy of reactive plasmas: A method for correlating emission intensities to reactive particle density. *J. Appl. Phys.* **51,** 3134–3136 (1980).

108. Di, L.-B. *et al.* Atmospheric-pressure plasma CVD of TiO 2 photocatalytic films using surface dielectric barrier discharge. *J. Phys. D. Appl. Phys.* **42,** 32001 (2009).

109. NIU Jinhai, ZHANG Zhihui, FAN Hongyu, YANG Qi, LIU Dongping, Q. J. Plasma-Assisted Chemical Vapor Deposition of Titanium Oxide Films by Dielectric Barrier Plasma-Assisted Chemical Vapor Deposition of Titanium Oxide Films by Dielectric Barrier Discharge in TiCl 4 / O 2 / N 2 Gas Mixtures ∗. *Plasma Sci. Technol.* **16 No. 7,** (2014).

110. Das, C. *et al.* Thermal and plasma enhanced atomic layer deposition of TiO2: Comparison of spectroscopic and electric properties. *J. Vac. Sci. Technol. A Vacuum, Surfaces, Film.* **33,** 01A144 (2015).

Acknowledgement

I could not have completed this graduation project without the help and assistance of a number of people, which I would all like to thank for their contribution to this Master Thesis work.

First of all, I would like to thank Adriana Creatore for all her help and guidance during the last 16 months. I also want to thank you for commenting and correcting this Master Thesis! The same goes for Morteza Aghaee, who joined me in most of the experiments and was always available for a discussion. I enjoyed working with you!

This graduation project is performed at Innophysics B.V., a company in Eindhoven. I would like to thank Hugo de Haan for the opportunity to do this interesting graduation project at his company. I learned a lot at Innophysics, in all kind of aspects. Therefore I would like to thank Hugo, Alquin Stevens and Joop Schep for the pleasant working environment, I really enjoyed working at Innophysics. I'm very happy and grateful for the opportunity to keep working at Innophysics after this graduation project.

7. Appendices

A. Atmospheric pressure (plasma-assisted) ALD

In chemical vapor deposition (CVD) both precursor and reactant gases are simultaneously in the reaction chamber. However separating both gas exposures into two discrete steps, leads to a significantly enhanced process control. The deposition technique in which precursor and reactant exposures are applied alternatively is known as ALD [1]. Extended information of ALD can be found in [1,15,102,16].

ALD is a thin film deposition technique with sub-nanometer thickness control. One ALD cycle is divided in two (or more) half-reactions, in which the precursor and reactant are applied alternatively, separated by purge steps [1]. A schematic of one ALD cycle of Al_2O_3 is shown in Figure 46. In the first step the substrate is exposed to the vaporized precursor molecules (tri-methyl-aluminum, TMA), which absorb at the surface. The reaction is self-limiting because there are a limited amount of available surface sites. The reaction chamber is purged after precursor exposure (step 2), to remove residual precursor molecules and reaction products (CH_4), which completes the first half-cycle.

In the second half-cycle (step 3) the surface is exposed to a second precursor (H_2O), a co-reactant gas, which chemically reacts with the absorbed precursor molecules. An Al_2O_3 monolayer is formed and reactive surface sites (OH groups at the surface) are created, for the next ALD cycle. The produced byproducts (H_2O and CH_4) are purged away from the chamber by a purge step (step 4) [103]. The purge steps are performed to prevent reactions between precursor and co-reactants, which could lead to unwanted and uncontrollable CVD reactions [104]. In an ideal situation the surface is covered with one homogenous sub-monolayer after every half-cycle, since both half-reactions are self-limited. Therefore only one monolayer is deposited per ALD-cycle and the material is deposited layer-by-layer [1], enabling ultimate growth control by controlling the number of ALD-cycles. The self-limiting effect of the half-cycles results in a saturation of the growth rate, manifesting in a characteristic growth per cycle (GPC) [85]. By ALD deposited thin films are characterized by excellent conformity, uniformity, surface coverage, high film quality and excellent thickness control on atomic scale [1,53]. Besides the advantages, ALD is characterized as a slow, often low pressure process, which makes it difficult and expensive to scale up [103].

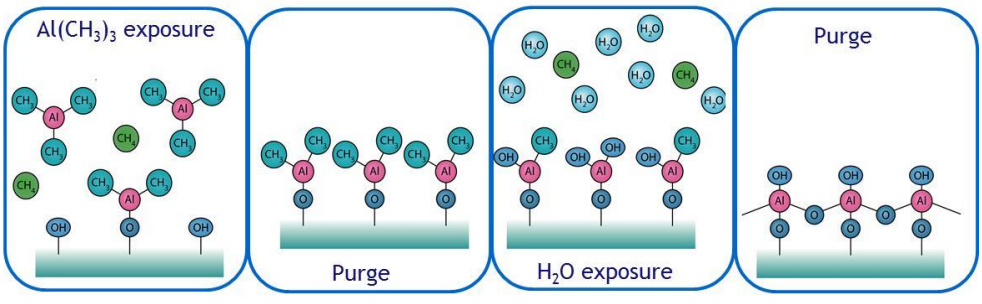

Figure 46: Schematic diagram of one ALD cycle of Al_2O_3. The different steps are depicted from left to right. One ALD cycle is divided in two half-reactions, each consisting of a gas exposure and a purge step. First the substrate is exposed to the vaporized precursor (TMA). The precursor molecules absorb at the surface, followed by a purge step (step 2). In the second half-cycle (step 3) the surface is exposed to a reactant gas (H_2O), which chemically reacts with the ligands of the precursor molecule. Reactive surface sites are created and an Al_2O_3 monolayer is formed. The ALD-cycle is completed with a purge step (step 4). Taken from [5].

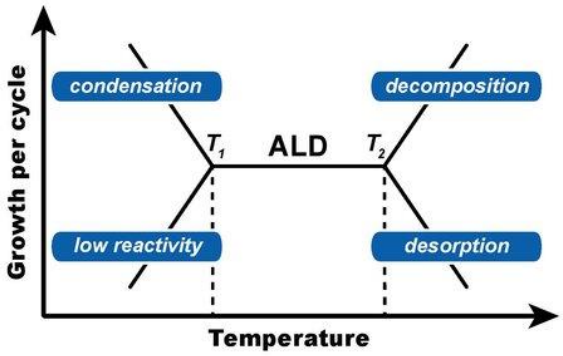

Figure 47: Temperature window for an ideal ALD process, the GPC is shown as a function of temperature. The GPC shows no or weak dependence on the substrate temperature inside the temperature window (between T_1 and T_2), while it is disrupted outside the temperature window, due to several effects. For example when the substrate temperature T is lower than a specific threshold temperature T_1, the precursor and/or reactants can condense on the surface, leading to the formation of porous and impure films and thereby increasing the GPC. However reactions require a specific threshold activation energy, therefore $T<T_1$ could also reduce the reactivity and the corresponding GPC. Moreover a substrate temperature exceeding a specific temperature T_2 could lead to decomposition of precursor/reactants and thereby increasing the GPC through additional and uncontrollable CVD reactions. $T>T_2$ can also lead to a decreased GPC by re-evaporation or etching of reactive surface groups and/or material above a specific temperature. [85]

Every ALD process is characterized by a specific temperature window in which the GPC is shown as a function of substrate temperature (Figure 47). The temperature window of an ideal ALD process is represented by the temperature range in which the GPC shows no or weak dependence on the temperature (between T_1 and T_2 in Figure 47). In the regions outside the temperature window, the ALD reactions are disrupted by several chemical and/or physical processes. For example when the substrate temperature T is lower than a specific threshold temperature T_1, the precursor and co-reactants are able to condense on the surface and form porous and impure films through undesired and uncontrollable reactions, thereby increasing the GPC. However reactions require a specific threshold activation energy, therefore $T<T_1$ can also reduce the reactivity and the GPC. A substrate temperature exceeding a specific temperature T_2 ($T>T_2$) can lead to decomposition of precursor/reactants and to corresponding additional and uncontrollable CVD reactions, thereby increasing the GPC. However $T>T_2$ can also lead to a decreased GPC, since reactive surface groups and/or material can re-evaporate or etch above a specific temperature [85].

Nonetheless, the required substrate temperature to initiate ALD reactions is reducible by replacing the reactant gas by plasma, referred to as plasma-assisted ALD. The principles, advantages and merits of plasma-assisted ALD have been well described in a review article from Profijt et al [16]. The difference between a thermal and a plasma-assisted ALD process is shown in Figure 48. In plasma-assisted ALD process, the plasma exposure takes over the role of the reactant. The produced plasma species (e.g. radicals, ions) interact with the surface, creating reactive surface sites on which the precursor bonds in the next half-cycle. As in thermal ALD, the reactions are self-limiting due to limited number of available surface sites and the reactor chamber is purged after plasma exposure to remove all reaction byproducts.

The use of plasma as reactant gas is characterized by several benefits[16]:

- The high reactivity of the plasma reduces the required substrate temperature, which is beneficial when for example fragile substrates are used which cannot withstand heat.

- The use of plasma results in improved material properties (in terms of density, impurity content, electronic properties, etc.) in comparison with thermal ALD processes, due to higher reactivity of the plasma.
- Some precursors (e.g. heteroleptic Cp-based alkoxides) are not applicable in thermal ALD processes due to a weak reactivity [97]. Hence the use of plasma as reactant leads to an increased choice of precursors and materials.
- The density, power and exposure time of the plasma provide additional parameters which can be used to tune the film composition and stoichiometry. Moreover, the plasma exposure time can be controlled accurately, due to fast on/off switching of the plasma.
- Reduced purge times, since the produced plasma species are often more volatile than the reactant gases used in thermal processes. Reduced purge times results in an increased throughput of the ALD setup.
- Etc.

Despite all the advantages, the use of plasma as reactant could lead to reduced conformality (for example for surfaces with high aspect ratio) and to plasma damage. Plasma damage can occur due to high ion bombarding energies, which are accelerated in the plasma sheath, which could lead to displacement of atoms, bond breaking, etc. [16]

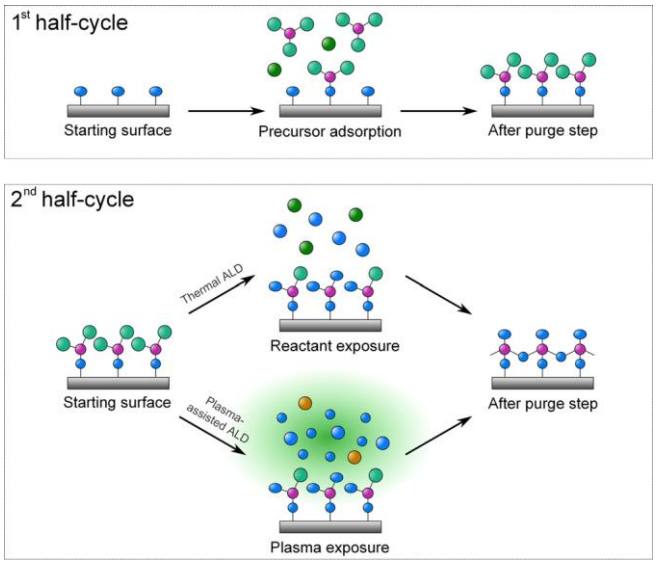

Figure 48: Schematic representation of the difference between a thermal and plasma-assisted ALD process. Taken from [16]1

In temporal ALD, the substrate is located at a fixed location and the precursor and reactant exposures are alternatively applied in the reaction chamber. The different exposures are separated by purge steps in which the reaction chamber is evacuated. The precursor and reactant exposures are separated in the time domain, as shown in Figure 49a. However the gas exposures can be separated in the spatial domain, which is known as spatial ALD [2,15,105]. In spatial ALD, each part of the substrate is alternatively exposed to the precursor and reactant in separate dosing zones. The gas exposure zones can be integrated in a deposition head, as depicted in Figure 50a [2]. The head is divided in individual gas flow zones, through which the precursor, reactant or an inert gas flows. The inert gas is used for a purge step and to separate the precursor and reactant gases from each other. The deposition head is located in proximity to the sample's surface and either the head or the sample is shifted to obtain ALD

reactions, as shown in Figure 49b. Figure 50b shows the different gas exposures experienced by one fixed point Q on the surface as function of time in a spatial ALD process [2]. Every part of the surface experiences an alternate exposure of precursor and reactant gas, separated by an inert gas, in order to achieve self-limiting ALD reactions.

In temporal ALD, the whole reaction chamber has to be evacuated after each gas exposure (i.e. precursor and reactant) and therefore the purge steps are time consuming. While in spatial ALD the purge steps are performed in separate purge zones, which is therefore faster and more efficient than in temporal ALD. Moreover, the precursor and reactant exposures are applied more efficiently in spatial ALD. Therefore higher throughputs can be obtained by spatial ALD. Besides the higher throughputs, spatial ALD is normally not limited by substrate size and is therefore more applicable in industrial applications and roll-to-roll processing [103]. As in temporal ALD, the reactant exposure can be replaced by plasma exposure, in order to increase the reactivity and to reduce the required substrate temperature. Successful deposition of Ag [106], ZnO [2], Cu_2O [103], Al_2O_3 [2,36] and TiO_2 [37,33] by spatial ALD processes are reported in the literature.

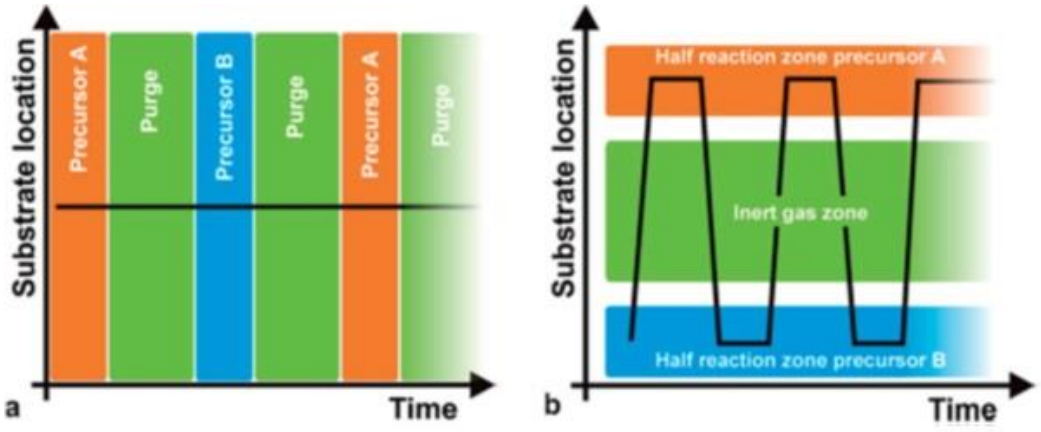

Figure 49: Temporal vs. spatial ALD. Substrate location and different gas exposures are shown as function of time. Temporal ALD (a): substrate is located at a fixed position while the precursor and reactant gases are applied alternatively in the reaction chamber, separated by purge steps in which the chamber is evacuated. Spatial ALD (b): each part of the substrate is alternatively exposed to the different gases, by shifting the substrate through the different gas exposure zones. [103,105]

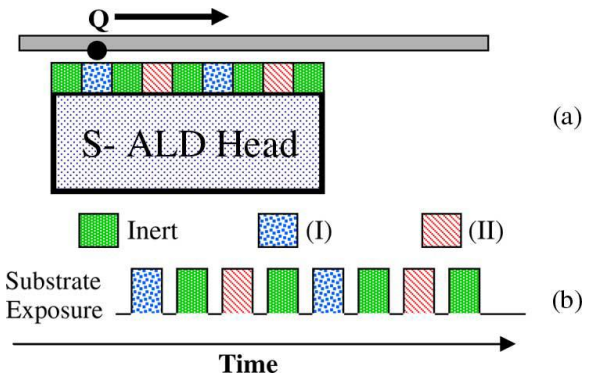

Figure 50: (a) Schematic representation of a spatial ALD – head. The head is divided in separate gas flow zones through which the precursor (blue) and reactant (red) flows, separated by purge zones (green) through which an inert gas flows. (b) The different gas exposures experienced by one fixed point on the substrate as function of time. [2]

B. Hardware modifications

In this section the required system modifications to upgrade the µPP to a versatile tool for patterned TiO_2 thin film deposition are described. The µPP was never used to deposit metal oxides thin films before and numerous problems were encountered. The different modifications are described below:

Gas curtain system

First of all, a gas curtain system was designed, in order to enclose the gas mixture and print-stage from the environment, since the organometallic titanium precursor (TTIP) chemically reacts with moisture (i.e. water) from the environment. Two different curtains were designed, one for the PE-CVD mode and one for plasma-assisted ALD mode. However two different gas chambers exist to plasma treat dielectric and conductive substrates. Therefore the gas curtain system limited the ALD experiments to conductive substrates only.

Gas delivery and heating systems

The first experiments were performed without a bubbler heating system. However TTIP has a melting point of 17°C and the precursor solidified during night. A bubbler heating system was installed to prevent solidification of the precursor inside the bubbler and kept the TTIP bubbler at 32 ± 3°C. Initially, the gas delivery setup was used with flexible polymer lines, however polymer lines absorb water from the environment. The reaction of water with the TTIP precursor resulted in powder formation and no TiO_2 film could be deposited. Therefore the polymer lines were replaced by stainless steel flexible lines, which are however very expensive. Since the TTIP bubbler was heated to 32°C, a precursor line heating tool was required to prevent condensation of the TTIP precursor on colder locations inside the lines. The stainless steel lines were enrobed with heating wire, which was fed with a supply voltage and a feedback system was used to maintain the line temperature at 50°C (Eurotherm 2408f). The print-stage (i.e. gas chamber / precursor dosing head) required a heating system, to prevent condensation in the deposition chamber. The print-stage was enrobed with heating wire and fed with a supply voltage (Kossoni Voltage Regulator, 0-250 V). The required voltage to maintain a temperature of 50 ± 5°C inside the deposition chambers was checked with a thermocouple. The precursor lines and print-stage were enrobed with aluminum foil to ensure a uniform temperature distribution.

The µPP has been initially designed without substrate heating, however substrate heating was required to prevent condensation on the substrate. Therefore, a silicon heatmat (240V, 100 W) was glued to the bottom side of the glass substrate table and a Honeywell thermostat switch was placed in the middle of the heatmat. The temperature switch opened the connection at 70°C and closed back at 55°C, in order to maintain the topside of the substrate table at a temperature of 55 ± 5°C. Different substrate temperatures are possible, since the temperature switches are available in a very broad range. The power of the heatmat (100 W) had to be limited to prevent a too fast temperature increase and correspondingly large temperature differences in the glass substrate table, which could lead (and unfortunately led) to cracking of the glass table. The power was limited by a simple dimmer, normally used for house lightning, which was integrated in the substrate heating system and slowed down the heating process.

Extra modifications plasma-assisted ALD mode

In this paragraph extra modifications specific for the ALD mode are described. First of all, a gas dosing head was designed and integrated at the print-stage. The head was made of aluminum, with two

connections, one for inlet and one for the outlet. The dosing head was integrated at the location of the camera system, normally used to visualize the discharges. Secondly, a different gas curtain system was designed. Finally, the µPP software required modifications to enable the ALD-process. The possibility to add a precursor dosing position was added, together with the possibility to add extra purge times in the ALD-cycles. Moreover, the possibility to change the motion speed of the system separately during µPlasmaPrinting and precursor dosing was integrated.

Equipment

In this paragraph, a list of the used equipment, such as MFCs, vacuum pump, heating systems, etc. is given:

- Bronckhorst MV-302 MFC for precursor dosing
- Bronckhorst MV-302 MFC for O_2-flow to plasma print head
- Bronckhorst MFC for gas curtain system (20-2000 sccm)
- Vacuubrand MZ2C vacuum pump, pump speed controlled by a needle valve and MFC
- Heat mat with Honeywell Thermostat switch
- Horst HT20N250 for bubbler heating system
- Eurotherm 2408f for line heating system
- Kossoni Voltage Regulator, 0-250 V for gas chamber heating

C. Conductive substrate configuration

Additional schematics of the conductive substrate configuration are presented in this section. As already has been discussed in section 3.1, an extra dielectric layer is required to plasma treat a conductive substrate (i.e. Si). Figure 51 presents a 3D schematic of the print-stage as it was used to plasma treat conductive substrates. It is worth mentioning that two different gas chambers exist, depending on the type of substrate. The gas chamber used in the conductive substrate configuration has a notch in which the dielectric spacer fits. A schematic view of the PE-CVD µPP setup used for deposition on conductive substrate is shown in Figure 52.

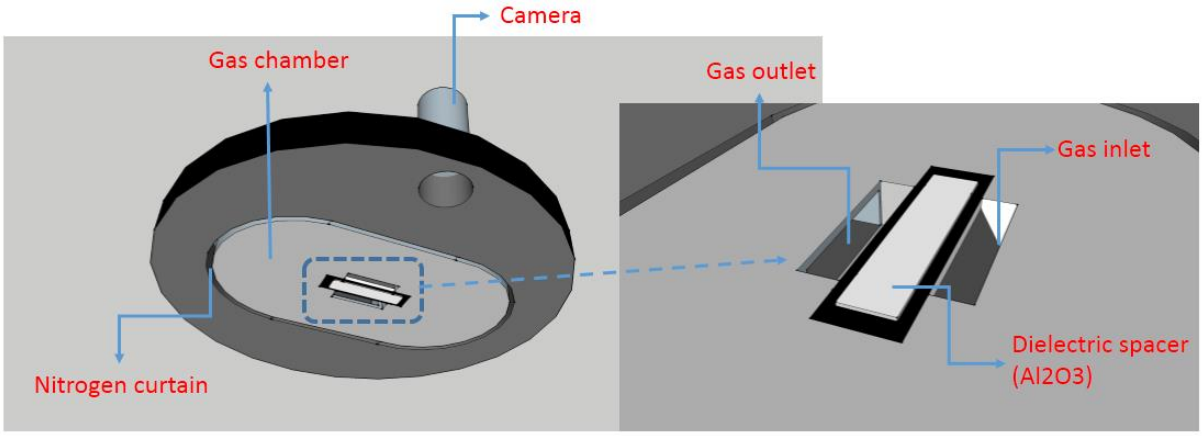

Figure 51: 3D schematic of the print-stage for plasma treating conductive substrates. A dielectric layer is positioned between the needle electrodes and the conductive substrate.

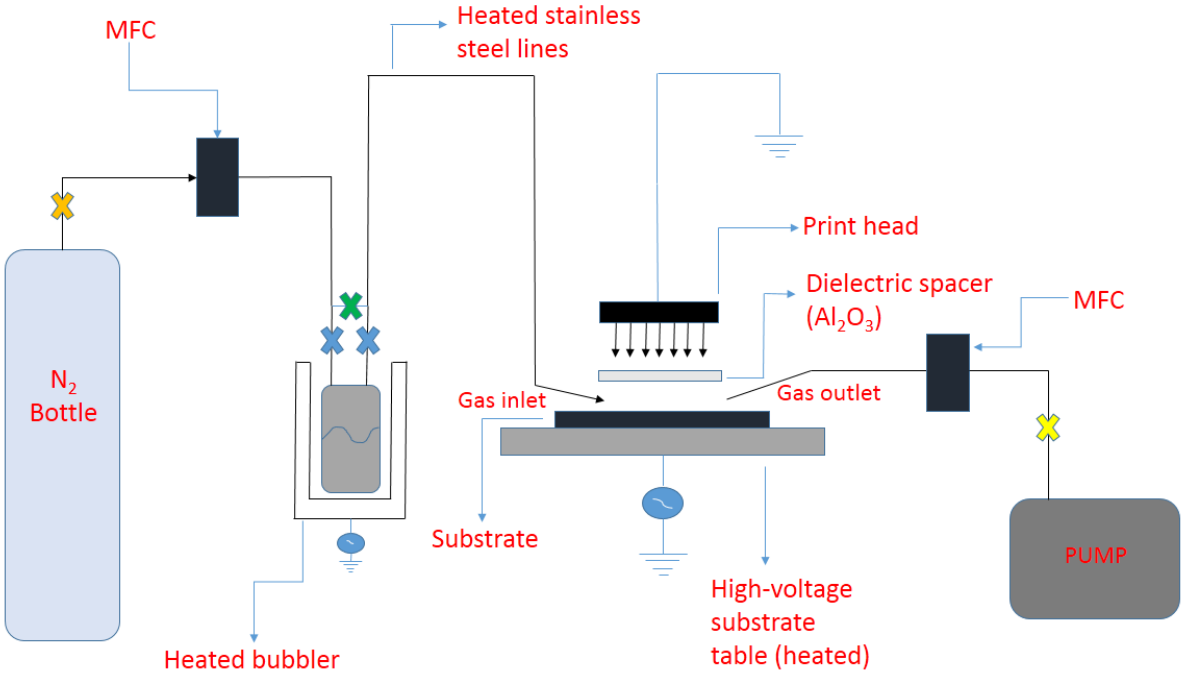

Figure 52: Schematic view of the PE-CVD µPP setup for depositing on conductive substrates (i.e. Si). The TTIP precursor and exhaust flow was 53 and 75 sccm, respectively. The gas curtain system was fed with 500 sccm N_2. The temperatures were the same as in the setup for depositing on dielectric substrates.

D. XPS line-scan: proof of concept

The patterning resolution of the µPP in the two different operation modes was determined by means of XPS line-scan, as described in sections 3.3.2 and 4.1.4. In XPS line-scan, multiple XPS measurements are performed on different positions perpendicular to the deposition line, equally spaced by 60 µm. The result is a spectrum showing the atomic % of the elements as a function of distance, from which the patterning resolution can be determined. In this section a proof of concept is given.

A reference sample with a well-defined pattern was made in order to proof the accuracy of XPS line-scan. An Al_2O_3 line with a width of 500 µm was deposited by a combination of photolithography and ALD. The line width was consequently determined by XPS line-scan, the result is presented in Figure 53. The determined line width at FWHM is approximately 500 µm, therefore it can be concluded that XPS line-scan is accurate.

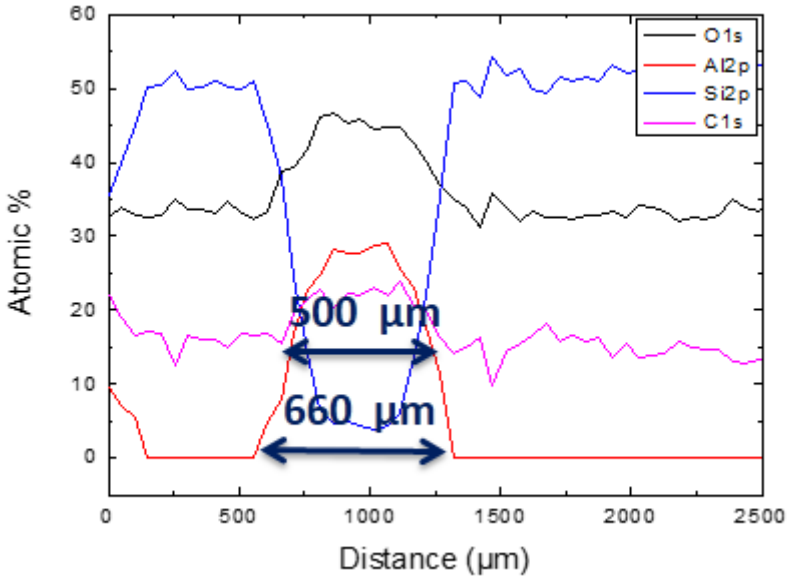

Figure 53: Atomic % of Al, O, Si and C as function of distance, determined by XPS line-scan. An Al_2O_3 line with a width of 500 µm was deposited by a combination of photolithography and ALD. The line width, determined by XPS line-scan is approximately 500 µm at FWHM.

E. OES measurements

Optical Emission Spectroscopy (OES) is an often used optical diagnostic technique and was performed to determine the active species in the plasma. Photons are emitted when atoms or molecules in electronically excited states spontaneously decay to lower energy states, the emitted photons are analyzed in OES [107]. The corresponding photons have characteristic frequencies, which are plotted in an emission spectrum. An OES spectrum is in principle a collection of spectral lines generated by the different excited species in the plasma [53]. The intensity of the emission lines depends on the concentration of the specific species. Therefore OES enables the possibility to identify the excited species in a plasma and it can provide a measure for the relative concentration [53]. An Ocean Optics USB4000 OES system with a detection range from 200 to 1100 nm was used. A collimating lens was used to guide the produced light into the glass fiber, which was connected to the OES system. The results are presented from Figure 54 to Figure 56. Figure 54 shows the full range emission spectra for 10 sccm N_2 (black) and 10 sccm O_2 (red) as gas mixtures with V_{PP} = 5.8 kV. All significant spectral lines are located in a wavelength range between 250 and 450 nm, which is shown in Figure 55. It is worth mentioning that the OES measurements were performed in open air, without using the gas curtain system. The N-related peaks are also observed when O_2 is used, due to the presence of N_2 from the environment. Atomic N could not be detected with the used OES system, since the dominant N-peaks are located at 149 and 174 nm [59]. However the presence of N_2^+ species was observed (Figure 55), which requires an energy of 15.5 eV to form [28]. Therefore the presence of atomic Nitrogen is assumed since the energy required to dissociate a N_2 molecule is only 9.7 eV. Figure 56 presents the OES spectrum obtained when 15 sccm O_2 was used as gas mixture with V_{PP} = 7.0 kV, the peak at 777 nm corresponds with O-radicals.

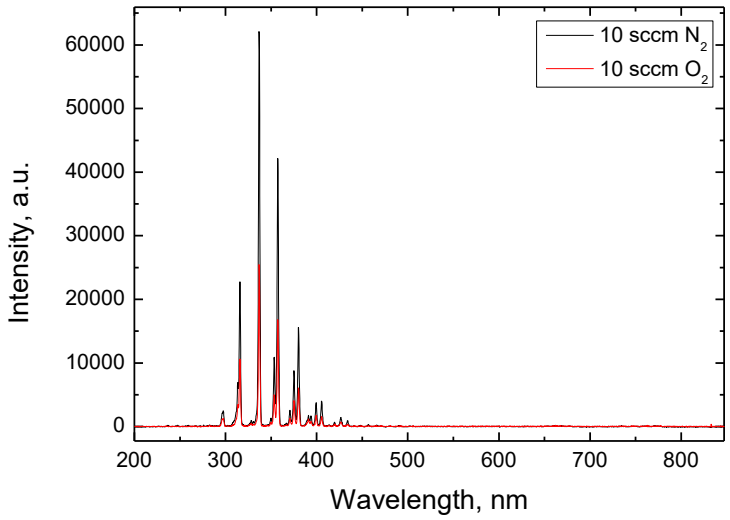

Figure 54: Optical emission spectra for 10 sccm N_2 (black) and 10 sccm O_2 (red) as gas mixtures with V_{PP} = 5.8 kV.

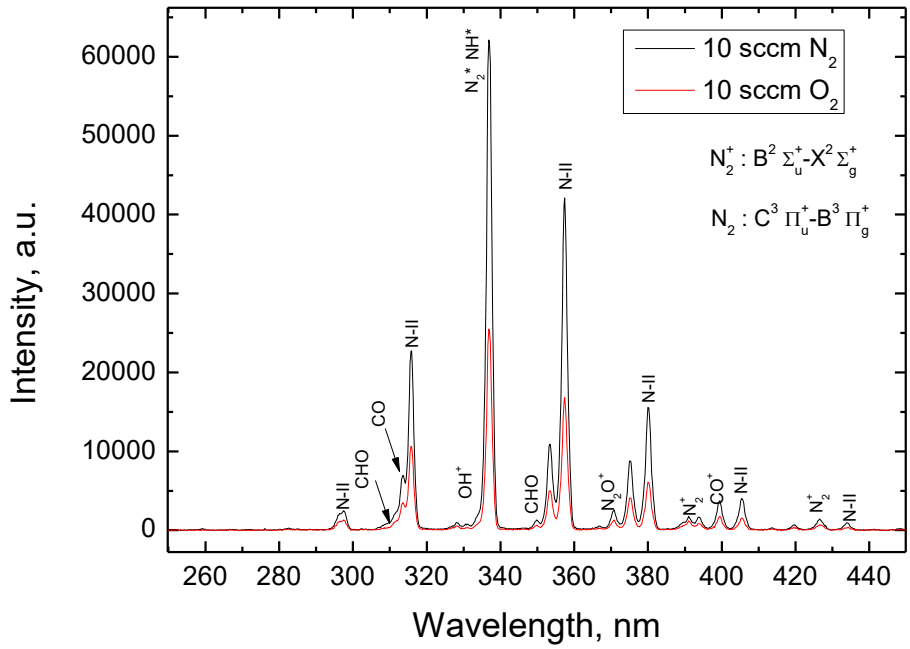

Figure 55: Optical emission spectra for 10 sccm N_2 (black) and 10 sccm O_2 (red). Zoomed region of Figure 54. The presence of N_2^+ species is observed in the spectra.

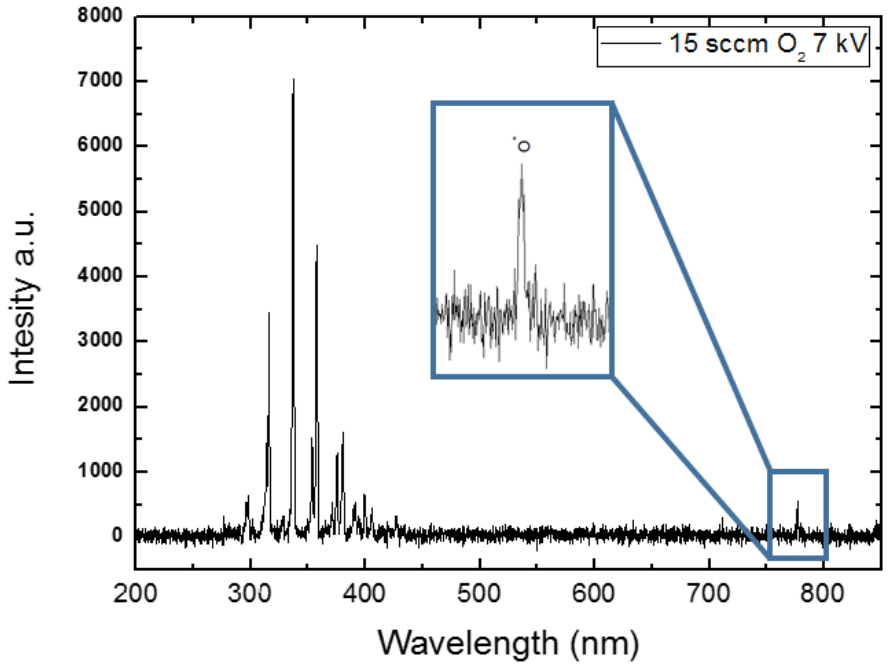

Figure 56: Optical emission spectrum for 15 sccm O_2 as gas mixture with V_{PP} = 7.0 kV. The peak at 777 nm corresponds with O-radicals.

F. Comparison with literature

An overview of other in the literature reported TiO_2 (plasma enhanced) CVD and ALD processes and their corresponding properties is given in this section. The CVD processes are presented in Table 10 and the ALD processes in Table 11. The setup and material properties of this work are added as a comparison.

Table 10: Overview of other reported CVD systems and corresponding properties.

Reference	**This work**	[58]	[108]	[64]	[62]	[63]	[57]	[109]	[71]
Type	DBD-CVD	DBD-CVD	DBD-CVD	PECVD-µ-wave Torch	PECVD	PIMOCVD	DBD-CVD	DBD-CVD	Plasma jet
Precursor	TTIP	TTIP	$TiCl_4$	TTIP	TTIP	Titanium oxide acetylacetonate	TTIP	$TiCl_4$	Aerosolized TTIP
Gas mixture	N_2–N_2/O_2	N_2	O_2	Argon	N_2/O_2	N_2/O_2	O_2	O_2/N_2	N_2 / Dry air
Substrate	Glass / Si	Si	Si	Si	Si	Si	Glass	Si	Glass / Si
Pressure	Atm	Atm	Atm	Atm	Vacuum	Atm	Atm	Vacuum	Atm
Temperature	55°C	400°C	350-450°C	50-200°C	100-250°C	200-300°C	Roomtemp	/	Roomtemp
Growth rate (nm/s)	3250-5700	0.34	0.37	1.67	0.42-0.62	0.05-0.125	0.3	0.95-1.87	20000-40000
O/Ti ratio	2.15-2.60	/	/	2.2	2.7	>2.0	3.7*	2.58-??	1.84-2.04
C content (%)	5-10 %	/	/	<4%	3%	4.5%	32.7%*	/	3.39-10.57%
N content (%)	1.7-3.4%	/	/	/	0.9-3.5%	3.7%	/	/	0.82-1.08%
RMS Surface roughness (nm)	0.25 Si; 4-11 on glass	/	/	/	0.7-1.4	~ 1	15-23	2-10	/
RI (@ 632.8 nm)	1.81	/	/	/	1.8-2.1	2.4 @ 300 °C	/	/	/

** = influence of hydrocarbon surface contamination.*

Table 11: Overview of other reported ALD systems and corresponding properties

Reference	**This work**	[37]	[40]	[42]	[43]	[86]	[41]	[110]	[34]	[35]
Pressure	Atm	Vacuum	Atm	Vacuum	Atm	Vacuum	Vacuum	Vacuum	Vacuum	Vacuum
Substrate temperature	55°C	80-120°C	Room temp.	160°C	100°C	100-300°C	250°C	200°C	150-250°C	50-250°C
Precursor	TTIP	TTIP	TTIP	TTIP and $TiCl_4$	$TiCl_4$	*	TTIP	TTIP	TTIP and $TiCl_4$	TTIP
Oxidant	O_2-plasma	H_2O, O_3 and O_2 plasma.	O_2-Plasma	H_2O	H_2O	O_2-Plasma	O_2-Plasma	H_2O and O_2-Plasma	H_2O, O_3 and O_2 plasma.	O-radicals
Growth rate (nm/cycle)	0.145	0.012-0.056	0.16	0.07	0.06	0.07-0.10	0.13	0.05	0.07	0.19
O/Ti ratio	2.05-2.20	/	/	/	/	2.0	/	1.9-2.3	/	/
Carbon impurity content	0-5%	0.5-5.9%	/	/	/	<0.6%	/	/	/	4%
Nitrogen impurity content	1.8-5%	/	/	/	/	2.3%	/	/	/	/
RMS surface roughness (nm)	0.25	/	0.25	/	/	0.3-1	/	/	/	/
Refractive index	1.97 @ 632.8 nm	2.3	/	2.1 @ 580 nm	/	2.1 @ 100°C	/	/	2.3 @ 580 nm	2.2 @ 580 nm

** = Cyclopentadienyl Alkylamido [Ti(CpMe)(NMe2)3]*